Beyond the Shockley-Queisser Limit: Intermediate Band and Tandem Solar Cells Leveraging Silicon and CdTe Technology

by

Jonathan P. Mailoa

B.Sc., Massachusetts Institute of Technology (2011)
M.Eng., Massachusetts Institute of Technology (2012)

Submitted to the Department of Electrical Engineering and Computer Science
in Partial Fulfillment of the Requirements for the Degree of

Doctor of Philosophy

at the

MASSACHUSETTS INSTITUTE OF TECHNOLOGY

June, 2016

©2016 Massachusetts Institute of Technology

All rights reserved.

Author: ______________________________

Department of Electrical Engineering and Computer Science
May 20, 2016

Certified by: ______________________________

Tonio Buonassisi
Professor of Mechanical Engineering, Massachusetts Institute of Technology
Thesis Supervisor

Accepted by: ______________________________

Leslie A. Kolodziejski
Chair, Department Committee on Graduate Students

Beyond the Shockley-Queisser Limit: Intermediate Band and Tandem Solar Cells Leveraging Silicon and CdTe Technology

by

Jonathan P. Mailoa

Submitted to the Department of Electrical Engineering and Computer Science

May 20, 2016

In Partial Fulfillment of the Requirements for the Degree of
Doctor of Philosophy in Electrical Engineering and Computer Science

ABSTRACT

The efficiencies of single-junction solar cells have been rapidly increasing and approaching their fundamental Shockley-Queisser efficiency limits. This is true for mature commercial technologies such as silicon and cadmium telluride. In order to enable solar cells with higher efficiency limits, new concepts need to be implemented which overcome the fundamental energy conversion mechanism limitations of single-junction solar cells. For this approach to be successful, it is advantageous to leverage existing manufacturing facilities and integrate these new solar cell architectures into commercially successful solar cell technologies such as silicon and cadmium telluride.

In this thesis, two novel solar cell concepts are explored, categorized into three contributions. First, the application of intermediate band concept on silicon solar cells is explored by hyperdoping silicon, demonstrating room-temperature sub-band gap optoelectronic response from the material, and evaluating the feasibility of the intermediate band approach for improving silicon solar cell efficiency. Second, perovskite solar cells are integrated onto silicon solar cells to demonstrate mechanically-stacked perovskite/silicon tandem solar cell using low-cost silicon cell and monolithic perovskite/silicon tandem solar cell enabled by a silicon tunnel junction. Third, an analytic model is built to rapidly investigate the energy yield of different tandem solar cell architectures. When applied to cadmium telluride-based tandem solar cells, this model will help thin-film companies like First Solar narrow down the scope of future research and development programs on tandem solar cells.

Thesis Supervisor: Tonio Buonassisi
Title: Professor of Mechanical Engineering

ACKNOWLEDGEMENTS

I would like to express my gratitude to all of my colleagues at MIT Photovoltaic Research Laboratory for their support throughout this work. Yun Seog Lee helped me to get settled in the group and let me work on a couple side projects before I started my first project. Austin Akey, Christie Simmons, Joe Sullivan, and Mark Winkler were especially helpful to me in the early days of my graduate school when I have just started my first project. Support from Eric Johlin, Jungwoo Lee, Jim Serdy, Robert Hoye, Marius Peters, Sarah Sofia, and Felipe Oviedo were instrumental in the completion of my subsequent projects. Danny Ren, Haohui Liu, Zhe Liu, Nasim Khanghah, and Serena Lin from our sister lab in Singapore helped deepen my knowledge on high-efficiency solar cells. I thank Lauren Wolinsky, Mariela Castillo, Allyna Nguyen, and David Rodriguera for their administrative and lab support throughout the years. Last but not least, I would like to thank my advisor Tonio Buonassisi for his guidance throughout the years, for the freedom he gave me on driving my research direction, for the bridges and opportunities he built for my research, for the eloquent examples he showed me in building professional relationships, for the patience he displayed when I decided to not execute some of his suggestions and for the occasional free meals he bought his students during business travels. I couldn't have asked for a better graduate research advisor.

I have had a wonderful time collaborating with researchers from many outside institutions throughout my graduate school career. Inna Kozinsky (Robert Bosch RTC), my first research supervisor who introduced me to solar research and patent process. Colin Bailie, William Nguyen, Kevin Bush, Eric Hoke, and Michael McGehee (Stanford), whom we partnered

with and raced together toward the world's first perovskite/silicon tandem solar cells. Wenjie Yang and Jim Williams (ANU); Dan Recht and Michael Aziz (Harvard); Dave Hutchinson and Peter Persans (RPI); Jay Mathews and Jeff Warrender (Benet Lab); whom we partnered with to track down the elusive sub-band gap photoresponse of hyperdoped silicon. Senthil Balasubramanian, Ido Salama, Samantha Holmes, and Jody Fu (Sistine Solar), whom I collaborated with to build aesthetic photovoltaic products. Dirk Weiss, Mitchell Lee, Alex Panchula, Gang Xiong, Sachit Grover, Roger Malik, Zhibo Zhao, and Raffi Garabedian (First Solar), who provided me with many resources during my research internship at First Solar. I especially thank Dirk for letting me work on the research project and evaluate technical and commercial feasibility of tandem cells as future First Solar products. In the process, it has let me voiced my technical opinion on the company's future R&D direction; a feat which I have never imagined when I first started my graduate school. I thank Kenta Nakayashiki (REC) and James Glass (First Solar) for giving me amazing tours and explanations of full silicon and CdTe manufacturing lines respectively, which truly fascinate and enlighten me to be more involved with the transition from research into product in my future careers.

One's professional work can only flourish with the generous support of one's personal foundations. I thank my family for the support they gave me throughout the years; be it moral support or physical support in the form of special instant noodle shipments from home (yes, you have read it correctly). I thank my Indonesian friends, as well as friends at MIT and Harvard for the good and the bad times they have spent with me in New England. I thank the Janet Fischer and Anne Hunter from Course VI administration office for organizing the company information sessions throughout my years at MIT; free meals and raffles from these

information sessions always lightened up my mood and were the perfect physical and mental nourishment for a poor graduate student. I thank Japanese mangakas, animators, and video game developers for the entertainment materials they provided me during my undergraduate and graduate years at MIT, which certainly kept me away from stressful mood. Last but not least, I would like to thank the special individuals who have made my life memorable.

Nine years have passed, and I am finally ready to leave MIT and start a fulltime career. After all these years and efforts to move away from MIT, I will FINALLY manage to move away… right across the street to Kendall Square (>__<). Friends and colleagues, I will still be around in Cambridge for a while. Thank you for your support all these years, and I’ll see you around.

DEDICATION

To her

TABLE OF CONTENTS

Content | Page

ABSTRACT iii
ACKNOWLEDGEMENTS v
DEDICATION ix
TABLE OF CONTENTS xi
LIST OF TABLES xv
LIST OF FIGURES xvii
1. Chapter 1: Introduction 1
1.1. Motivation 1
1.2. Multiple Carrier Generation Solar Cells 3
1.3. Intermediate Band Solar Cells 5
1.4. Multijunction Solar Cells 6
1.5. Beyond the SQ Limit Concepts for Silicon and CdTe Solar Cells 9
2. Chapter 2: Evaluation of Intermediate Band Solar Cell Utilizing Hyperdoped Silicon 15
2.1. Background 15
2.2. Materials & Methods 19
2.2.1. Gold Hyperdoping of Silicon 19
2.2.2. Si:Au Gold Concentration & Structural Characterization 21
2.2.3. Si:Au Sub-Band Gap Optical Absorption 22
2.2.4. Si:Au Photodiode Device Fabrication 24
2.2.5. Si:Au Photodiode Type Determination 25
2.2.6. EQE Calculation for Photodiode Steady-State Photoresponse 26
2.2.7. Modeling of Fully-Depleted Hyperdoped Region in Si:Au Diode 27
2.2.8. Transient-Pulse Photoresponse 28
2.2.9. Two-Photon Absorption Model for Photodiode Background Response 30
2.3. Results & Discussion 31
2.3.1. Steady-State Room-Temperature Sub-Band Gap Photoresponse 31
2.3.2. Room-Temperature Spectral Response of Si:Au Photodiodes 33

2.3.3. Origin of Sub-Band Gap Photoresponse in Si:Au Photodiode....36
2.3.4. Spectral Response Dependence to Hyperdoped Silicon Dopant Type....38
2.4. Conclusions & Perspective....41
3. Chapter 3: Demonstration of Perovskite/Silicon Tandem Solar Cell....45
3.1. Background....45
3.1.1. Rapid Prototyping of 4T Tandem using Inexpensive Silicon....49
3.1.2. Designing 2T Tandem with *n*-Type Silicon Cell....53
3.1.3. Designing 2T Tandem with *p*-Type Silicon Cell....54
3.2. IR-Optimized Silicon Cells Made from Inexpensive Silicon for 4T Tandem....55
3.2.1. Materials & Methods....55
3.2.1.1. Selection of Inexpensive Silicon for Tandem....55
3.2.1.2. p-Type Silicon Cell Fabrication....56
3.2.1.3. Semi-Transparent Perovskite Cell Fabrication....60
3.2.1.4. 4T Tandem Cell EQE & J-V Measurement....70
3.2.2. Results & Discussions....71
3.2.2.1. 1J Perovskite Device Results....72
3.3. Silicon Cells with Integrated Tunnel Junction for 2T Tandem....77
3.3.1. Materials & Methods....77
3.3.1.1. n-Type Silicon Sub-Cell with Built-In Tunnel Junction....77
3.3.1.2. Tunnel Junction Functionality Analysis....82
3.3.1.3. Perovskite Sub-Cell Fabrication....83
3.3.1.4. Tandem Cell Testing Protocols....87
3.3.2. Results & Discussions....90
3.3.2.1. Performance of 2T Perovskite/Silicon Tandem....90
3.3.2.2. 2T Tandem Optical Loss Analysis using FDTD....94
3.4. Integration with Industrial *p*-Type Silicon Cells for 2T Tandem....96
3.4.1. Materials & Methods....96
3.4.2. Results & Discussions....100
3.5. Conclusions & Perspective....101
4. Chapter 4: Energy-Yield Assessment of CdTe-Based Tandem Solar Cell....105
4.1. Background....105
4.2. Methods & Results....108

4.2.1. Model 1: Radiatively Limited STC Efficiency & Architecture Selection 109
4.2.2. Model 2: Semi-Empirical STC Efficiency Limit 114
4.2.3. Model 3: Semi-Empirical Annual Energy-Yield 117
4.2.4. Model 3 Extension: Inclusion of Cell Operating Temperature 124
4.3. Discussion 126
4.4. Conclusions & Perspectives 128
5. Chapter 5: Conclusion 133
6. Chapter 6: Future Work 137
References 141
A. Appendix 155
A.1. Validation of Semi-Empirical Tandem Energy Yield (Model 3) 155

LIST OF TABLES

Table | Page

Table 3-1. Performance metrics of semi-transparent and opaque perovskite devices.............................73
Table 3-2. Performance metrics of 1J sub-cells and 4T perovskite/silicon tandem devices 75
Table 4-1. Top and bottom cell materials and band gaps for the CdTe-based tandem architectures.....111
Table 4-2. E_g range and record efficiency of sub-cell candidates for CdTe-based tandems.....................112
Table 4-3. Summary of tandem efficiencies in Model 1, 2, and 3 117
Table 4-4. Polycrystalline device parameters used in both efficiency and energy-yield models.............119
Table 4-5. Tandem relative energy-yield advantage over a 1J CdTe cell...124

LIST OF FIGURES

Figure Page

Figure 1.1. Two primary energy loss mechanisms in 1J photovoltaic cells ... 2
Figure 1.2. Optical loss analysis for an ideal 1J silicon cell under AM1.5G (1000 W/m^2) ... 2
Figure 1.3. Optical loss analysis for an ideal 1J CdTe cell under AM1.5G (1000 W/m^2) ... 3
Figure 1.4. Multiple carrier generation utilizing impact ionization of hot carriers ... 4
Figure 1.5. Singlet excitonic fission for multiple exciton generation solar cells ... 5
Figure 1.6. Up-conversion mechanism in intermediate band solar cells ... 6
Figure 1.7. Multijunction solar cell built using spectral splitting architecture ... 8
Figure 1.8. Multijunction solar cell built using 4T and 2T tandem architecture ... 9
Figure 2.1. Si:Au fabrication by ion implantation followed by pulsed laser melting ... 20
Figure 2.2. SIMS and TEM characterization of Si:Au ... 22
Figure 2.3. Sub-band gap light absorptance in thin Si:Au layer ... 23
Figure 2.4. Si:Au photodiode device geometry ... 24
Figure 2.5. Si:Au doping type determination by rectification test ... 26
Figure 2.6. Comparison of measured and simulated Si:Au photodiode *I-V* curve ... 27
Figure 2.7. Tunable-wavelength transient photoconductivity setup ... 28
Figure 2.8. Si:Au Sub-band gap transient photoresponse signal ... 29
Figure 2.9. Spatially-mapped steady-state sub-band gap EQE measurement setup ... 31
Figure 2.10. Spatially-mapped sub-band gap photoresponse of Si:Au photodiode ... 32
Figure 2.11. Au dose dependence of Si:Au photodiode sub-band gap photoresponse ... 33
Figure 2.12. Sub-band gap spectral response of Si:Au photodiode ... 34
Figure 2.13. Linear intensity dependence of Si:Au sub-band gap photoresponse ... 35
Figure 2.14. Bias voltage dependence of Si:Au photodiode sub-band gap photoresponse ... 38
Figure 2.15. Possible sub-band gap photoresponse mechanism in Si:Au photodiode ... 38
Figure 2.16. Polynomial dependence of sub-band gap photoresponse conversion efficiency η ... 40
Figure 3.1. Rapid efficiency record increase of 1J perovskite solar cells ... 47
Figure 3.2. Perovskite crystal structure and band gap tenability ... 48
Figure 3.3. Siemens process for 9N–11N pure Si feedstock production ... 50
Figure 3.4. FBR process for 6N–9N pure Si feedstock production ... 51
Figure 3.5. UMG-Si and TI-Si feedstock production process flow ... 52
Figure 3.6. *p*-type silicon cell fabrication process flow ... 58
Figure 3.7. EQE of 1J and IR-optimized 4T silicon cell made from inexpensive silicon ... 59
Figure 3.8. Transmission spectrum through AgNW film laminated on PET substrate ... 62
Figure 3.9. Optical density over time of perovskite film in dipping solution ... 64
Figure 3.10. Semi-transparent perovskite device efficiency distribution ... 69
Figure 3.11. Device stack of 4T perovskite/silicon tandem solar cell ... 71

Figure 3.12. *J-V* and EQE of 1J perovskite devices 72
Figure 3.13. Light transmission through semi-transparent 1J perovskite cell 73
Figure 3.14. *J-V* and EQE of 4T perovskite/silicon tandem devices 74
Figure 3.15. Device stack and SEM image of 2T perovskite/Si tandem 77
Figure 3.16. 2T perovskite/Si tandem interlayer recombination mechanism 78
Figure 3.17. TEM image of Si tunnel junction 79
Figure 3.18. SIMS profile of Si tunnel junction on *n*-type silicon cell 80
Figure 3.19. *J-V* profile for identical Si cells with & without tunnel junction 82
Figure 3.20. EQE of 1J *n*-type Si cell with & without tunnel junction 83
Figure 3.21. Light transmission into Si sub-cell in 2T perovskite/Si tandem 84
Figure 3.22. Time-transient J_{sc}, V_{oc}, and MPP of perovskite/Si tandem as the cell stabilizes 88
Figure 3.23. *J-V* curve of 2T perovskite/Si tandem on *n*-Si cell 90
Figure 3.24. EQE of 2T perovskite/Si tandem on *n*-Si cell 91
Figure 3.25. Front/back illumination on 1J semi-transparent perovskite cell 92
Figure 3.26. Light transmission through 470-nm-thick doped spiro-OMeTAD 93
Figure 3.27. Optical simulation of absorption spectrum in perovskite/*n*-Si tandem layers 95
Figure 3.28. SIMS profile of Si tunnel junction on *p*-type silicon cell 98
Figure 3.29. Prototype device structure for perovskite/silicon tandem on *p*-type silicon solar cell 99
Figure 3.30. *J-V* curve of prototype 2T perovskite/silicon tandem on *p*-Si cell 100
Figure 3.31. Efficiency record progression for perovskite/silicon tandem solar cells 101
Figure 4.1. Model 1, radiative STC efficiency limit for 2J tandem solar cells 111
Figure 4.2. Semi-empirical STC efficiency for 2J tandems in Model 2 115
Figure 4.3. Simulation flowchart for tandem energy yield calculation in Model 3 120
Figure 4.4. Light Absorption for Architecture A with FTO vs ITO as TCO 121
Figure 4.5. Device structure and energy yield of Architecture A in Model 3 122
Figure 4.6. Device structure and energy yield of Architecture B in Model 3 123
Figure 4.7. Device structure and energy yield of Architecture C in Model 3 124
Figure 4.8. Model 3 extended: Temperature effect on energy yield of Architecture C 125
Figure 4.9. Dips in AM1.5G spectrum due to water vapor absorption 127
Figure A.1. Validation of Model 3 using device-physics-based baseline model 155

Chapter 1: Introduction

1.1. Motivation

Silicon (Si) and cadmium telluride (CdTe) photovoltaics currently dominate the market of terrestrial photovoltaics. Silicon photovoltaics are promising for renewable energy applications due to their abundant feedstock, near-optimal band gap energy, and excellent electrical and mechanical properties. CdTe photovoltaics on the other hand, benefits from a streamlined and low-capital-cost polycrystalline thin-film module manufacturing. However, the efficiencies of these cells are limited by fundamental material properties of silicon and CdTe as semiconductors; which are their band gap energies (E_g) of 1.12 eV and 1.48 eV respectively. These properties determine the fundamental power conversion efficiency limit, which is known as the Shockley-Queisser (SQ) limit,[1] which is around 33% and 32% for silicon and CdTe photovoltaics, respectively (29.4% in silicon when Auger recombination is considered as an additional factor[2]). While various approaches within industry and academia have focused on increasing 1J silicon and CdTe photovoltaic efficiencies closer to the SQ limit (current records held by Panasonic with 25.6% efficient interdigitated back contact – silicon heterojunction (IBC-SHJ) cell[3] and First Solar with 22.1% band gap-graded thin-film CdTe solar cell),[4] none of these approaches can overcome the fundamental SQ limit for 1J photovoltaics. This limit is largely determined by the inefficient utilization of photons within the photovoltaic absorber layer. High-energy photons ($E_{ph} > E_g$) lose a fraction of their energy due to thermalization, while low-energy photons (sub-band gap, $E_{ph} < E_g$) are not absorbed by the photovoltaic cell (non-absorption loss) and cannot contribute to the solar cell output (**Figure 1.1**).

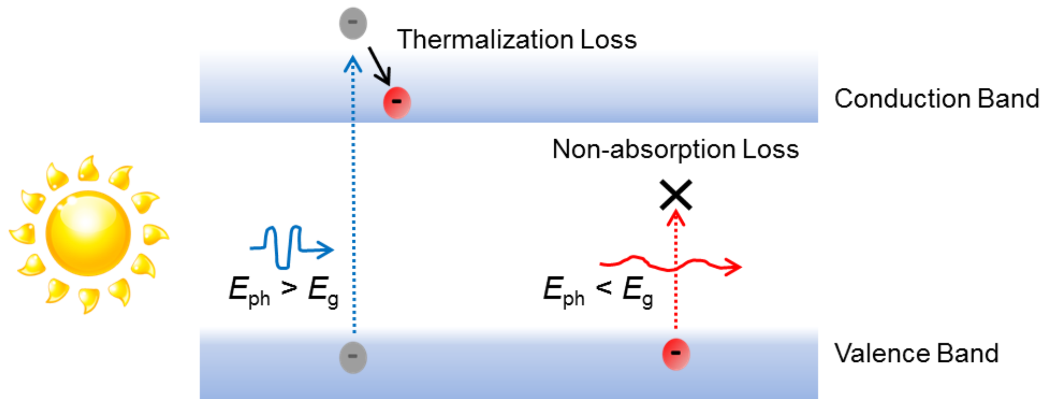

Figure 1.1. Two primary energy loss mechanisms in 1J photovoltaic cells

High-energy photons ($E_{ph} > E_g$) lose their energy because hot carriers quickly thermalize, while low-energy photons ($E_{ph} < E_g$) are lost because they are not absorbed.

For silicon, these losses alone account for as much as 50.9% of the optical energy under standard testing condition (STC) AM1.5G illumination spectrum. About 19.2% of these losses is caused by non-absorption, while 31.7% is caused by thermalization. As shown in **Figure 1.2**, only 49.1% of the optical energy in AM1.5G spectrum can be used by a 1J silicon cell.

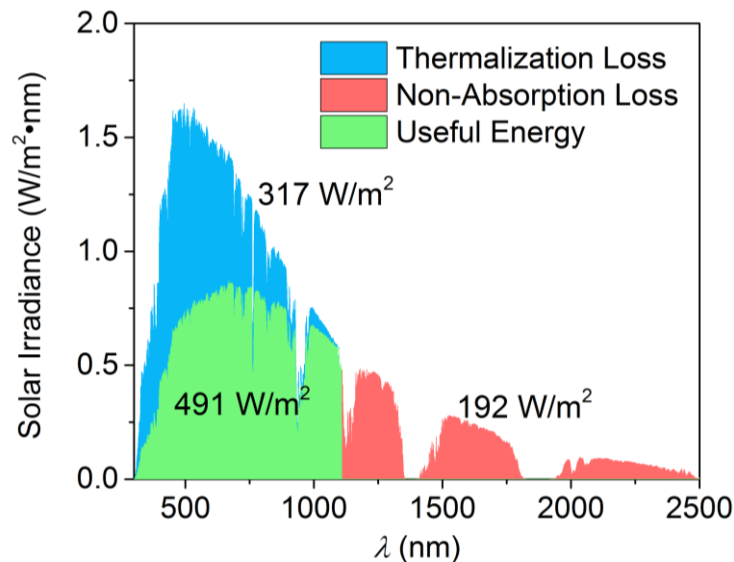

Figure 1.2. Optical loss analysis for an ideal 1J silicon cell under AM1.5G (1000 W/m²)

For CdTe, the situation is slightly different because its Eg of 1.48 eV is much wider than silicon. Under STC and AM1.5G illumination spectrum, 18.6% of these optical losses is caused by non-absorption, while 37.5% is caused by thermalization, as shown in **Figure 1.3**.

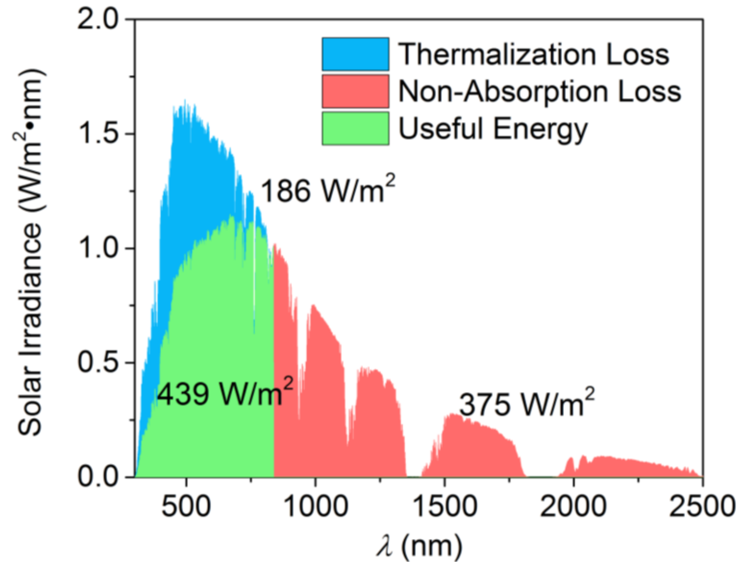

Figure 1.3. Optical loss analysis for an ideal 1J CdTe cell under AM1.5G (1000 W/m^2)

In order to mitigate these fundamental SQ loss mechanisms, solar cell architectures with additional physical mechanisms have been proposed, which can bypass the fundamental limitations detailed in the SQ limit. Some of these architectures are multiple carrier generation solar cells,[5] intermediate band solar cells,[6,7] and multijunction solar cells by using either spectral splitter or tandem architectures.

1.2. Multiple Carrier Generation Solar Cells

High-energy photons create just one electron/hole-pair in a typical *p-n* junction cell. Multiple carrier generation solar cells on the other hand, utilize down-conversion methods to channel the remaining energy from the high-energy photons to generate secondary electron/hole-pairs, effectively reducing the thermalization loss per high-energy photons.[5] This

concept can be achieved by several methods. One method is to utilize carrier multiplication caused by impact ionization, for example in $Si_{1-x}Ge_x$ alloys. In this concept, electron/hole-pairs generated by high-energy photons (hot carriers) collide with non-active carriers to form additional electron/hole-pairs; simplified schematic shown in **Figure 1.4**. Simulation work was performed for this system, which shows that impact ionization may enhance the theoretical conversion efficiency by a relatively small value of 0.5%.[8]

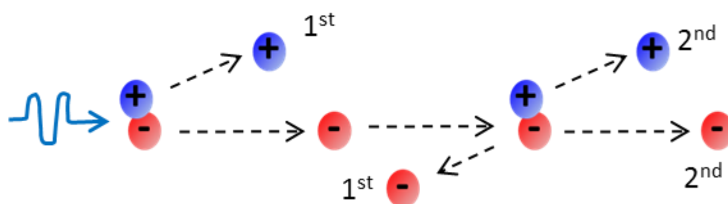

Figure 1.4. Multiple carrier generation utilizing impact ionization of hot carriers

Another possible method is to utilize multiple exciton generation (MEG) enabled by singlet excitonic state fission into two triplet excitonic states, which have previously been shown in organic materials such as pentacene or tetracene (**Figure 1.5**).[9] By utilizing the triplet excitonic states from this organic material, it is possible to make organic solar cells with quantum efficiency > 100%.[10] Further research has also shown that it is possible to couple these excitonic states into low-E_g quantum dot nanocrystals.[11] Nevertheless, coupling these excitonic states from pentacene into more mature photovoltaic materials such as silicon remains elusive. The demonstration of such phenomena, even in a small scale, is currently still an exciting research area in its own rights.

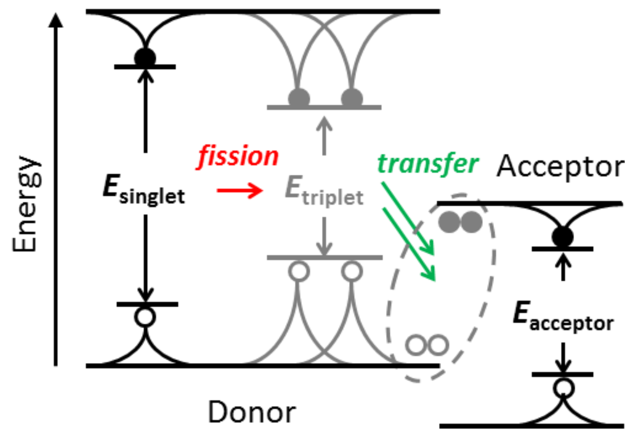

Figure 1.5. Singlet excitonic fission for multiple exciton generation solar cells

One singlet excitonic state undergoes fission into two triplet excitonic states. These excitonic states are then transferred into the acceptor in an organic solar cell, effectively producing multiple carrier pairs with one photon.

1.3. Intermediate Band Solar Cells

Intermediate band solar cells use up-conversion to enable two or more low-energy photons to excite one electron/hole-pair, effectively mitigating the non-absorption optical loss mechanism. This is usually enabled by introducing additional states into the band gap of the photovoltaic absorber layer, which acts as intermediary band for electrons from the valence band to temporarily get excited into before they eventually get excited into the conduction band (**Figure 1.6**).[6,12] The first solar cells based on this concept were developed in 2004, for which the energy levels of confined states in InAs quantum dots embedded in GaAs solar cells were used as the intermediate band.[13] The work has been able to demonstrate measurable GaAs solar cells with (albeit small, in the order of 10^{-4}–10^{-1}) quantum efficiency that extends to energies corresponding to sub-band gap photons. An alternative approach has also been successfully shown using intermediate bands arising from highly-mismatched alloys in ZnTeO system, although unfortunately the quantum efficiency of the process is still similarly low, in the order of 10^{-3}–10^{-2}.[14]

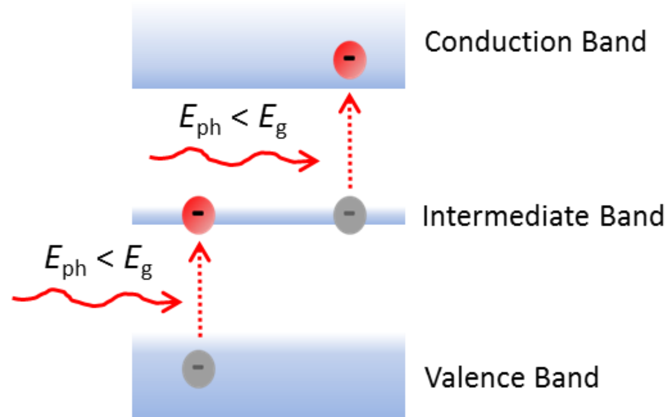

Figure 1.6. Up-conversion mechanism in intermediate band solar cells

The last approach to enable intermediate band solar cells involves the incorporation of deep-level impurities into silicon, effectively forming impurity intermediate band. This can be done by either evaporating thin film of deep-level dopant material on the silicon surface or implanting the deep-level dopants directly into the silicon, followed by pulsed laser melting (PLM) to turn the silicon surface into dopant-supersaturated single-crystal silicon layer called hyperdoped silicon.[15] While this approach is capable of producing hyperdoped silicon layer capable of more than 30% sub-band gap light absorption when chalcogen atoms like sulfur or selenium are used as the dopant,[16] no sub-band gap optoelectronic response from this single-crystal material had been observed from this material at room temperature before the work in **Chapter 2** was completed. Hence, it was not known whether the sub-band gap light absorption mechanism in hyperdoped silicon can be used in intermediate band solar cell or not, prompting an active research activity in the field.

1.4. Multijunction Solar Cells

Compared to multiple carrier generation solar cells and intermediate band solar cells, multijunction solar cells are different because they rely on neither down-conversion nor up-

conversion mechanisms. Instead of trying to introduce fundamentally new physics into solar cell devices, multijunction solar cells use multiple *p-n* junctions composed of different absorber materials with properly chosen E_g's to increase efficiency beyond its sub-cells' SQ efficiency limits. Depending on the new sub-cell being added onto the original 1J sub-cell, this architecture can mitigate either thermalization loss or non-absorption optical loss mechanisms. The sub-cell with higher E_g is used to absorb high-energy photons, while the remaining photons with lower energy are sent into the sub-cell with lower E_g. It is even possible to go well beyond 2-junction (2J) solar cells into 3 or more junctions, if desired. The obvious downside of this approach is the complexity and cost associated with the fabrication of the multiple junctions of the solar cells. However, this is also the most successful approach among attempts to surpass the SQ limit of 1J cells so far. Currently, the most efficient solar cell certified on record is at 46.0% under 508× direct sunlight (AM1.5D) concentration (4-junction solar cell developed by Fraunhofer ISE/Soitec).[17] The cell needs to be operated under high sunlight concentration because in addition to increasing its efficiency, the cell size reduction also significantly reduces the cell cost. The only commercial usage for these ultra-high-efficiency multijunction cells so far has only been for powering satellites in space, making the approach an extremely high-value application incompatible with terrestrial application as of now. Nevertheless, a more moderate multijunction solar cell composed of 2 junctions can potentially be suitable for terrestrial applications if suitable sub-cells are used.

There are many methods to make multijunction solar cells. For example, it is possible to simply fabricate two opaque solar cells with different E_g's and physically place them apart. Special optics can then be developed to split the incoming sunlight into two beams of light with

distinct wavelength spectra going separately onto the two sub-cells. The light beam with the higher average photon energy goes into the high-E_g sub-cell, while the light beam with lower average photon energy goes into the low-E_g sub-cell as shown in the basic spectral splitting architecture in **Figure 1.7**. While this spectral splitting scheme is relatively simple, it is worth noting that the physical setup is relatively costly, especially because of the optics and physical space required to make the scheme work. More research work is needed to find a better optical setup that can push down the cost of this spectral splitting architecture.

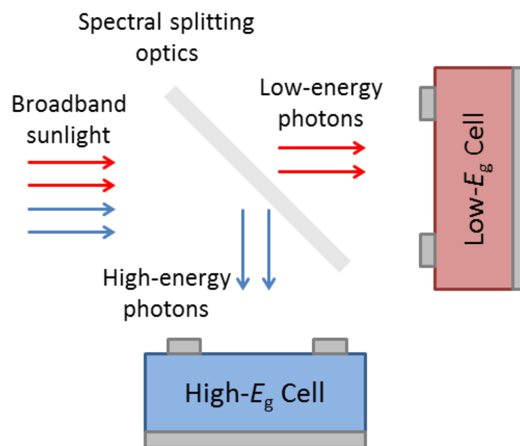

Figure 1.7. Multijunction solar cell built using spectral splitting architecture

Another attractive architecture for building a multijunction solar cell is what we call the tandem architecture, for which the low-E_g solar cell is placed directly below the high-E_g top cell. In the tandem architecture, it is necessary to design the top cell to be semi-transparent so that low-energy photons which are not absorbed in the high-E_g top cell can pass through and be absorbed by the low-E_g bottom cell. The two sub-cells can be fabricated separately, but mechanically stacked (and because there are two electrodes for each of the two sub-cells, we call this the 4-terminal (4T) tandem); or fabricated as a single monolithic device connected in

series (consequently it will have two electrodes, we call this the 2-terminal (2T) tandem). The 4T and 2T version of the tandem architecture is shown in **Figure 1.8**.

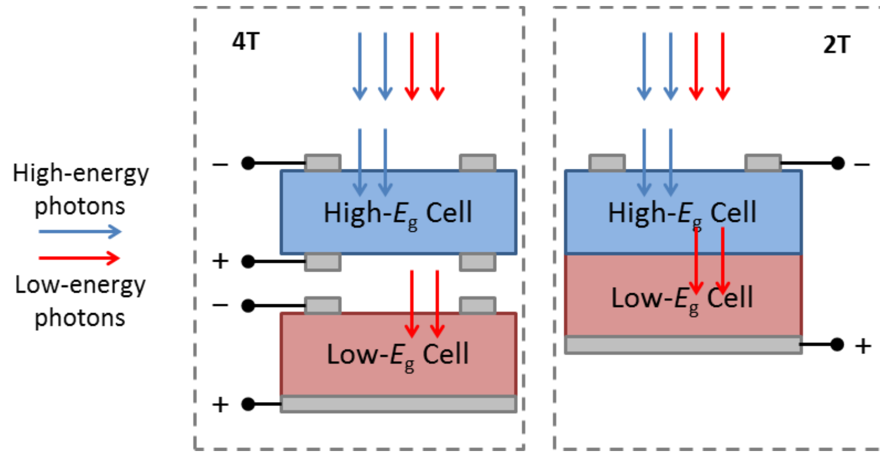

Figure 1.8. Multijunction solar cell built using 4T and 2T tandem architecture

1.5. Beyond the SQ Limit Concepts for Silicon and CdTe Solar Cells

Each of the three concepts outlined in **Section 1.2-1.4** poses significant research challenges in its own right. In this doctoral thesis, three specific contributions utilizing some of the concepts above are applied on commercially relevant solar cells such as silicon and CdTe.

In **Chapter 2**, the usage of silicon hyperdoped with gold (Si:Au) for silicon-based intermediate band solar cells to mitigate non-absorption optical loss in silicon solar cells is investigated. The primary challenge of this approach is that while large sub-band gap light absorption has been easily demonstrated using single-crystal hyperdoped silicon, no sub-band gap optoelectronic response had been demonstrated from this material at room-temperature (T = 25 ^{o}C) until this work. In this work, Si:Au was fabricated using pulsed laser melting (PLM) by our colleagues at Harvard University. Afterwards, Si:Au photodiodes were fabricated and careful characterizations were performed to show that the optoelectronic response originates

from gold impurity level within silicon and that the response increases with increasing gold doping concentration.[18] Because the resulting photoresponse has relatively small quantum efficiencies of about 10^{-4} under -5V reverse bias and 1-2 orders of magnitude smaller under forward bias, it is unlikely for this hyperdoping approach to be useful in silicon solar cells. However, the approach is simple and may be useful for the development of planar infrared photodetector array using silicon.

In **Chapter 3**, the usage of perovskite solar cells (rapidly emerging photovoltaic material) as the top sub-cell for a perovskite/silicon tandem solar cell is investigated, with the aim to mitigate thermalization optical loss in silicon solar cells. First, bottom silicon sub-cells made of low-cost silicon feedstock are fabricated. In collaboration with colleagues from Stanford University, who fabricated semi-transparent perovskite top sub-cells, a mechanically-stacked 4T perovskite/silicon tandem solar cell was demonstrated.[19] Following this prototype work, the first monolithic 2T perovskite/silicon tandem solar cell was also demonstrated, enabled by the development of a silicon tunnel junction and titanium dioxide (TiO_2) as the interlayer. The bottom silicon sub-cells and interlayer for the 2T tandem were designed and fabricated at MIT, while the top perovskite sub-cells were fabricated by colleagues at Stanford University.[20,21]

In **Chapter 4**, the modifications of CdTe 1J solar cells into tandem solar cells with II-VI top sub-cells is investigated, with the aim to mitigate non-absorption optical losses in CdTe solar cells. Collaboration was performed with First Solar, currently the largest thin-film solar company in the United States, on this endeavor. As a commercial company, First Solar is interested in performing a techno-economic analysis on the feasibility of tandem solar cells

based on its core expertise on CdTe solar cells. Before the company can justify spending money into research and development (R&D) program to commercially enable this tandem solar cell, it needs to assess the performance improvement potential as well as likely cell fabrication cost increase of the tandem solar cell. Based on the result, First Solar can then decide whether tandem solar cells based on II-VI top sub-cells are of commercial interest to the company or not. Because First Solar is a vertically-integrated solar company which performs business on the entire value chain (from solar module fabrication, project sales and development, to system production, large-scale power-plant installation and electricity generation), actual annual energy yield of the tandem module compared to a 1J module is more important and meaningful to the company than the STC efficiency number alone. Spectral modeling and semi-empirical annual energy yield models were built and utilized to evaluate different tandem architectures using II-VI top sub-cell. Based on the results, the relative annual energy yield advantage of different tandems can be quickly evaluated for different locations on Earth, guiding First Solar to focus on specific device architectures and to follow up with future cost modeling work.

Chapter 5 details the conclusions of the three topics in this thesis, which comprises of: 1. The first demonstration and evaluation of a new physical mechanism incorporation into a conventional solar cell; 2. The first demonstration of integrating a novel solar cell with a conventional solar cell using well-developed concepts; and 3. The commercially-oriented evaluation of advanced architectures based on commercial conventional solar cells.

In **Chapter 6**, I detail future work which may be of interest for further development of advanced concepts which can enable efficiencies beyond the Shockley-Queisser limits for silicon and CdTe-based solar cells.

Chapter 2: Evaluation of Intermediate Band Solar Cell Utilizing Hyperdoped Silicon

The content of this chapter is mainly taken from an article I have previously published in in Nature Communications.[18] Because Nature Communications is an open access only journal, the content of the article is being re-published in this thesis chapter under Creative Commons Attribution 4.0 International License.[22,23] My main contribution on this work has been on the experiment design, photodiode device fabrication, characterization setup construction, physical modeling, and manuscript preparation. The synthesis of gold-hyperdoped silicon using pulsed laser melting, as well as the TEM characterization of hyperdoped silicon layer, are performed by my co-authors.

2.1. Background

There are many incremental steps which are necessary to enable an intermediate band solar cell in silicon. First, it is necessary to incorporate a large number of deep-level states in the band gap of silicon, which enables absorption of sub-band gap light (photon energy E_{ph} < 1.12 eV) which is normally not absorbed by silicon. Next, it is necessary to show sub-band gap optoelectronic response from the material either under forward bias or under reverse bias. Finally, it will be necessary to show that the sub-band gap optoelectronic response is sufficiently large in forward bias operation at room-temperature to make the mechanism useful for solar cells. **The demonstration of sub-band gap photoresponse from a silicon photodiode through the intermediate band mechanism accomplishes the first two points, and consequently is an important step in the development of intermediate band solar cells based**

on silicon. Based on this photodiode demonstration, I can then evaluate the technical feasibility of using hyperdoped silicon for intermediate band solar cells based on silicon.

I demonstrate impurity-mediated room-temperature sub-band gap photoresponse in single-crystal silicon-based planar photodiodes.[18] A rapid and repeatable laser-based hyperdoping method incorporates supersaturated gold dopant concentrations on the order of 10^{20} cm^{-3} into a single-crystal surface layer ~150 nm thin (Si:Au). I demonstrate room-temperature silicon spectral response extending to wavelengths as long as 2200 nm, with response increasing monotonically with supersaturated gold dopant concentration. This hyperdoping approach offers a possible path to tunable, broadband IR imaging using silicon at room temperature. I characterize the Si:Au photodiode's sub-band gap optoelectronic response at room-temperature, show that the response originates from gold impurity level in silicon, and evaluate the technical feasibility of using hyperdoped silicon as material for intermediate band solar cells. I show that while Si:Au may not be suitable for usage as intermediate band solar cells, it may be possible for Si:Au to be useful for imaging applications.

Different levels of photoresponse lead to different applications. Devices with large quantum efficiency (QE) are useful for solar cells, while devices with small QE may be useful for photodetectors. Hyperdoped silicon devices are likely to have small sub-band gap QE's in the beginning; this makes infrared photodetectors to be the likely first applications for hyperdoped silicon. Developing a low-cost broadband infrared detector with array-based real time imaging capability at room temperature is of interest for telecommunications, security, energy, and R&D applications.[6,24–27] Silicon-based detectors satisfy the low-cost and on-chip CMOS-

compatibility criteria, but their infrared photoresponse is fundamentally limited by the 1.12 eV band gap (λ = 1110 nm). Previous attempts to extend the photoresponse of silicon-based devices into the short-wavelength infrared (SWIR) regime (λ = 1400 – 3000 nm) at room temperature focused on forming heterostructures with SiGe alloys[28–30] or microstructures of thermally absorbing material,[31,32] and modifying the intrinsic band structure via intentional introduction of defects.[33–39] Growing microstructures of foreign materials on top of silicon results in processing complexities that can compromise CMOS compatibility.[40,41] Furthermore, integration of thermally absorbing materials can be effective for SWIR response, but results in slow pixel response times intrinsically limited by the thermal time constant, which hinders applications in array-based real-time imaging systems at room temperature.[32]

The direct modification of silicon's electronic band structure is a promising approach for imaging applications, but significant advances on room-temperature sub-band gap photoresponse in silicon to date are mostly focused on fiber-coupled single-point detector applications. Published approaches predominantly involve intentionally damaging the silicon lattice,[33–39] which produces a measurable sub-band gap absorption coefficient ($\alpha = 2 – 4\ \mathrm{cm}^{-1}$)[38] compared to untreated silicon ($\alpha < 2 \times 10^{-7}\ \mathrm{cm}^{-1}$ for λ > 1400 nm).[42] To increase the optical path length and sub-band gap absorptance, these devices are integrated with micron-sized waveguide resonators.[35,39] By intentionally damaging the silicon lattice, Geis *et al*. fabricated single-point, fiber-coupled waveguide photodiodes and phototransistors with room-temperature sub-band gap (λ = 1550 nm) photoresponse of 20 and 50 $\mathrm{A \cdot W^{-1}}$, respectively.[38,39] These results correspond to impressive quantum efficiencies of 16 and 40, much larger than unity due to avalanche gain. [38,39] Unfortunately, the waveguide architecture renders this device

responsive for only a narrow band of wavelengths, and the requirement for co-planar illumination impedes incorporation into imaging arrays.

Another approach involves incorporating chalcogen dopants into silicon through picosecond or femtosecond laser irradiation. This approach has resulted in a limited number of reports of infrared photoresponse.[43,44] However, the origin of the sub-band gap photoresponse is not well understood or controlled due to the complexity of the laser-processed microstructure involving structural defects and multiple chemical phases.[45] To elucidate the origin of sub-band gap photoresponse in chalcogen-doped silicon, sulfur ions have been implanted into silicon and the resulting amorphous layer subjected to pulsed laser melting (PLM)-induced rapid solidification using a nanosecond (ns) laser, resulting in a single-crystalline silicon layer with sulfur concentrations above 10^{19} cm^{-3}.[15] This ns-laser hyperdoping process is repeatable and yields homogenous and single-crystal material, reducing the material's complexity compared to the microstructure with multiple phases found in silicon irradiated with picosecond or femtosecond lasers.[45] However, there are no reports of room-temperature sub-band gap photoresponse for this single-crystalline material. Because chalcogen-hyperdoping introduces only donor states into the silicon band gap; the resulting material has a large background free carrier concentration at room-temperature.[46,47] This large background free carrier concentration overwhelms the sub-band gap photoconductivity signal, making the observation of room-temperature sub-band gap photoconductivity in chalgogen-hyperdoped silicon difficult.[48] Similar problems have been encountered in titanium-hyperdoped silicon, for which sub-band gap photoconductivity is observed only at liquid-nitrogen temperature or below.[49] This is similar to prior work on impurity-diffused silicon photodetectors, where the

demonstration of sub-band gap photoresponse has been limited to low temperatures.[50,51] Room-temperature sub-band gap photoresponse of hyperdoped single-crystalline silicon remained elusive.

In this study, I report room-temperature sub-band gap photoresponse from single-crystalline silicon hyperdoped with an alternative dopant, gold, to concentrations as high as 5×10^{20} cm^{-3}. I present planar photodiode devices suitable for imaging-array applications fabricated from Si:Au. Steady-state and transient photoresponse measurements demonstrate that the photodiode optoelectronic response extends well into the sub-band gap regime of silicon, to at least λ = 2200 nm. Furthermore, the magnitude of the response increases monotonically with gold dopant concentration. The homogenous, single crystalline nature of Si:Au gives insight into the likely physical mechanism of enhanced sub-band gap photoresponse: a discrete set of Au-induced donor and acceptor mid-gap energy levels that generate free carriers in response to infrared light, yet reduce background free-carrier concentrations *via* self-compensation. Because PLM induces substantial heating only in the top 150 nm of the wafer, it might be added as the last step of any CMOS-compatible optoelectronic device fabrication process in user-defined device areas, limiting potential unintentional contamination effects of Au.

2.2. Materials & Methods

2.2.1. Gold Hyperdoping of Silicon

The top 150 nm of three identical <100> ***n***-type silicon wafers were implanted with $^{197}Au^{-}$ ions using an implantation energy of 50 keV and doses of $3{\times}10^{14}$, $7{\times}10^{14}$, and $1{\times}10^{15}$ cm^{-}

[2]. Pulsed laser melting (PLM) was used to melt the amorphous implanted region, which rapidly solidifies back into single crystal silicon with high, non-equilibrium dopant concentration (**Figure 2.1**).[15] Because of gold's high diffusive velocity and segregation coefficient in liquid silicon,[52] the high solidification speed outpaces the kinetics of gold segregation and results in a supersaturated, single crystalline solid solution.[52,53]

In this study, we used the third harmonic wavelength of Nd:YAG laser (λ = 355 nm), with a pulse duration FWHM of 5 ns and a fluence of 0.7 $J \cdot cm^{-2}$ for the PLM process. The Nd:YAG nanosecond pulse was used to melt and rapidly solidify the gold hyperdoped silicon (Si:Au) region, and *in situ* time-resolved reflectivity (TRR)[54] measurements showed a melt duration of 25 – 30 ns, corresponding to a solidification speed of about 7 – 10 $m \cdot s^{-1}$ based on a dopant diffusion simulation in established literature.[52]

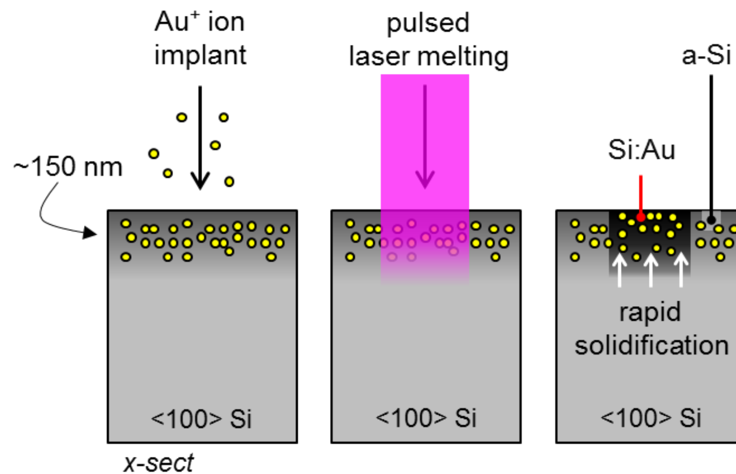

Figure 2.1. Si:Au fabrication by ion implantation followed by pulsed laser melting

Rapid solidification follows the PLM process, producing single crystalline Si:Au on the top 150 nm of the silicon wafer. The silicon area not melted by the PLM remains amorphous.

2.2.2. Si:Au Gold Concentration & Structural Characterization

After PLM, secondary ion mass spectrometry (SIMS) was performed to measure the gold atomic concentration as a function of depth (**Figure 2.2**). The solid-solubility limit of gold in silicon at room-temperature is estimated to be below 10^{15} cm^{-3}.[55–58] Supersaturated gold concentrations were achieved up to 150-nm depth for all 3 gold doses, with the largest gold concentration peak of 5×10^{20} cm^{-3} measured within the top 10 nm of the Si:Au layer. This corresponds to 1 at. % Au concentration, more than 4 orders of magnitude above the room-temperature equilibrium solid-solubility limit of gold in silicon.[55–58] The resulting material was characterized by SIMS using a Physical Electronics 6650 Dynamic SIMS instrument. Operating conditions were: 6 keV Cs ion beam at 1 nA, with SIMS craters being 50 um square; depth was measured *ex-situ* by contact profilometry. Au concentrations were calibrated against known ion-implantation doses from the as-implanted regions of each sample, normalized by the ^{28}Si signal. High-resolution transmission electron microscopy (HR-TEM) measurements confirmed that the entire Si:Au layer was single crystalline, without formation of any extended defects, secondary phases, or cellular breakdown (**Figure 2.2**).[59] TEM samples were fabricated by Focused-Ion Beam milling and liftout; TEM imaging was performed on a JEOL 2100 HRTEM operated at 200 keV in bright-field mode.

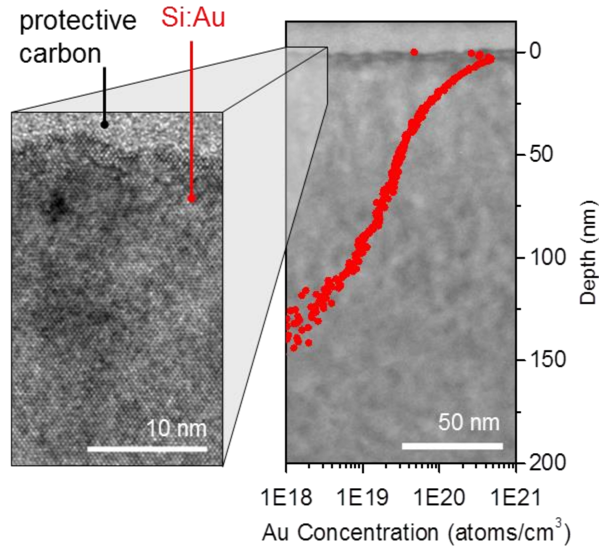

Figure 2.2. SIMS and TEM characterization of Si:Au

SIMS profile of Si:Au with 1×10^{15} cm^{-2} gold implantation dose, showing that the gold concentration in the Si:Au is more than four orders of magnitudes beyond the solid solubility limit of gold in silicon. The TEM images show that for this gold implantation dose, the entire Si:Au layer is crystalline.

2.2.3. Si:Au Sub-Band Gap Optical Absorption

Due to the large concentration of mid-gap dopant levels introduced by the gold impurities, the hyperdoped layer absorbs sub-band gap light as shown in the infrared transmission image through the sample taken using an InGaAs camera (**Figure 2.3**). Transmission (T) and reflection (R) were measured using UV-Vis-NIR spectrophotometry to quantify the sub-band gap absorptance ($A = 1 - T - R$) in the hyperdoped silicon. Similar to chalcogen-hyperdoped silicon,[60] sub-band gap light absorptance increases with increasing Au concentration (**Figure 2.3**).

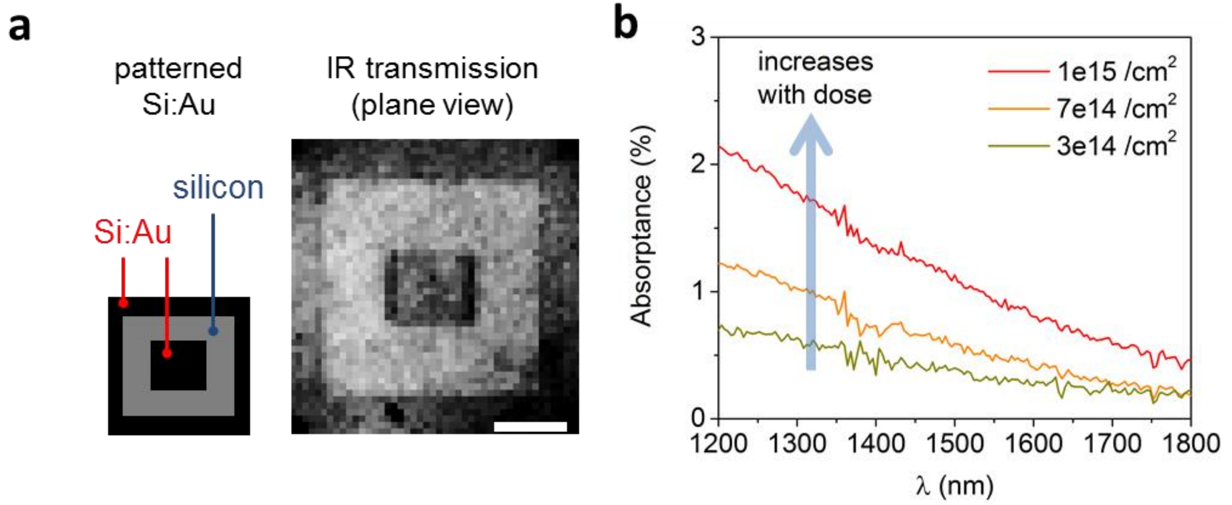

Figure 2.3. Sub-band gap light absorptance in thin Si:Au layer

(**a**) Transmission of sub-band gap light through patterned Si:Au taken using an InGaAs camera. Light transmission is reduced by absorption in Si:Au (dark areas) relative to the crystalline silicon (bright areas). (**b**) Sub-band gap light absorptance (*1 — Transmission — Reflection*) of Si:Au for various gold implantation dose relative to the sub-band gap light absorptance in the reference plain silicon sample, measured using UV-Vis-NIR spectrophotometry. Sub-band gap light absorptance increases with increasing gold dose.

I model the Si:Au as a uniform t = 150 nm thin film on top of crystalline silicon wafer. It is assumed that the real refractive index of Si:Au is not any different from that of a normal crystalline silicon. Furthermore, to simplify the model it is assumed that light interference in the thin-film Si:Au region does not play a critical role in the light propagation. Because crystalline silicon does not absorb sub-band gap light, the sub-band gap light absorption in the Si:Au layer can then be approximated as:

Equation 2.1 $$A = (1-R)\alpha t + (1-R)\alpha t(1-\alpha t)R + (1-R)\alpha t(1-\alpha t)^2 R^2 + \ldots = \frac{(1-R)\alpha t}{1-(1-\alpha t)R}$$

where A is the sub-band gap absorption measured using the spectrophotometer and R is the fraction of light reflected when light propagates through the air-silicon interface. Taking the value of R ~ 0.36 and A ~ 1%, $\alpha = A(1-R)/t(1-R-AR) = 660\,\text{cm}^{-1}$ can be approximated. This is the lower bound for the value of α in Si:Au with gold implantation dose of 10^{15} cm^{-2}. In reality,

90% of the gold atoms are buried within the top 20 nm of the Si:Au layer. Because the majority of the sub-band gap light absorption is believed to occur within this 20 nm thin layer, the actual value of α in the region with highest gold concentration may be several times larger. This is larger than that of germanium at the same wavelength (α ~ 300 cm^{-1}).[61]

2.2.4. Si:Au Photodiode Device Fabrication

We fabricate photodiodes from the Si:Au with the following dimensions (**Figure 2.4**).

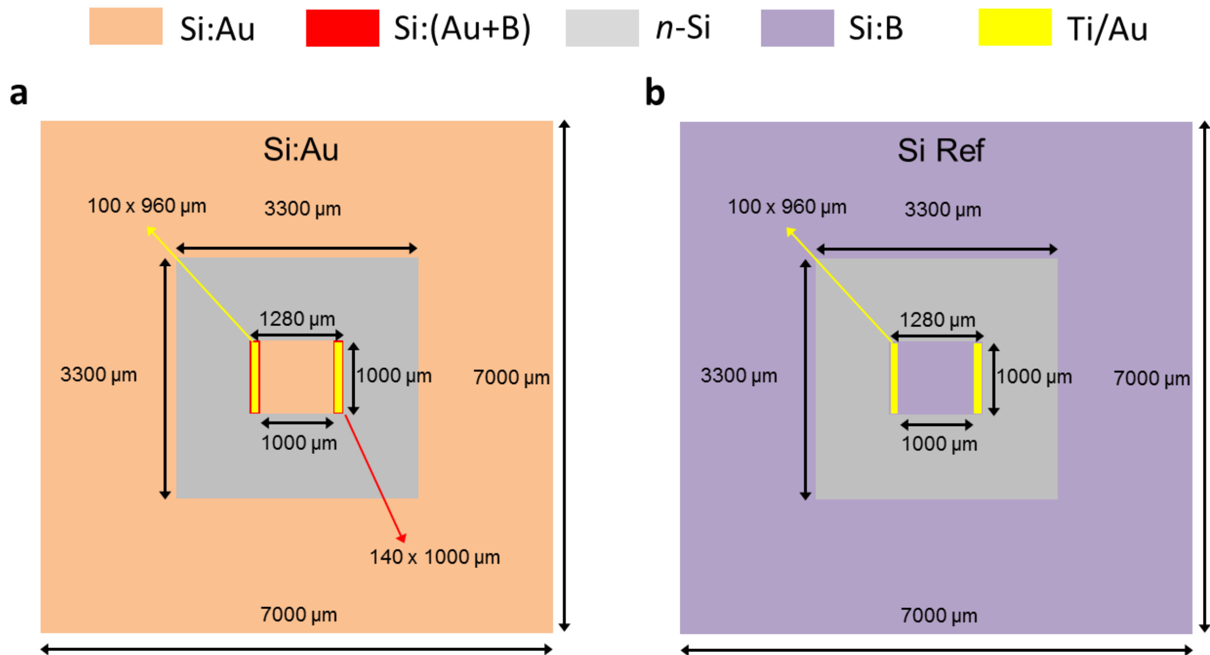

Figure 2.4. Si:Au photodiode device geometry

(**a**) Si:Au photodiode geometry. Shallow boron doping is introduced under the contact before the PLM process to reduce contact resistance to Si:Au. (**b**) Reference silicon photodiode geometry. ***p***-type Si:B layer was incorporated into the photodiode using PLM in lieu of Si:Au.

Prior to the PLM process, boron ions were selectively implanted into the gold-doped silicon area under the top contacts to improve contact resistance. The selected area for the boron implantation was patterned using photolithography, and $^{11}B^{+}$ ions (3×10^{14} cm^{-2} dose, 2 keV implantation energy) were implanted into the top 30 nm of the gold-doped area. The entire

sample then underwent the PLM process (**Section 2.2.1**), creating a homogenous single crystal Si:Au layer with a pair of rectangular Si:(Au+B) patterned areas positioned for subsequent contact deposition. The depth of the boron doping is simulated to be approximately 70 nm deep after the PLM process. Photolithography and SF_6 reactive ion etch (RIE) were then used to create a 1 μm-deep trench which isolated the 1×1 mm rectangular Si:Au and the Si:(Au+B) contact area from the rest of the Si:Au layer. Photolithography, *e*-beam evaporation and lift-off were used to deposit 30/160 nm of Ti/Au contacts on top of the Si:(Au+B) areas. On the back of the silicon wafer, a uniform 30/160 nm Ti/Au layer was deposited across the entire surface as the photodiode back contact. The back contact was attached to an external electrode by conductive silver paste, while the top contacts were connected to electrodes by Al wire bonds. For the reference silicon photodiode, the same boron doping profile is used everywhere instead of Si:Au, creating a ***p***-***n*** photodiode without any Au-hyperdoped silicon.

2.2.5. Si:Au Photodiode Type Determination

At the supersaturated concentrations obtained for Si:Au implanted with gold doses of 3×10^{14}, 7×10^{14}, and 1×10^{15} cm^{-2}, the majority-carriers in Si:Au are holes.[62] When Si:Au is fabricated on an ***n***-type silicon substrate, the resulting structure is a junction which shows the rectifying behavior of a diode in the dark (**Figure 2.5a**). In contrast, when Si:Au is fabricated on a ***p***-type silicon substrate (gold implantation dose of 10^{14} cm^{-2}), the resulting structure does not rectify in the dark (**Figure 2.5b**). This “control” test structure does not rectify since the majority-carriers in Si:Au are holes.

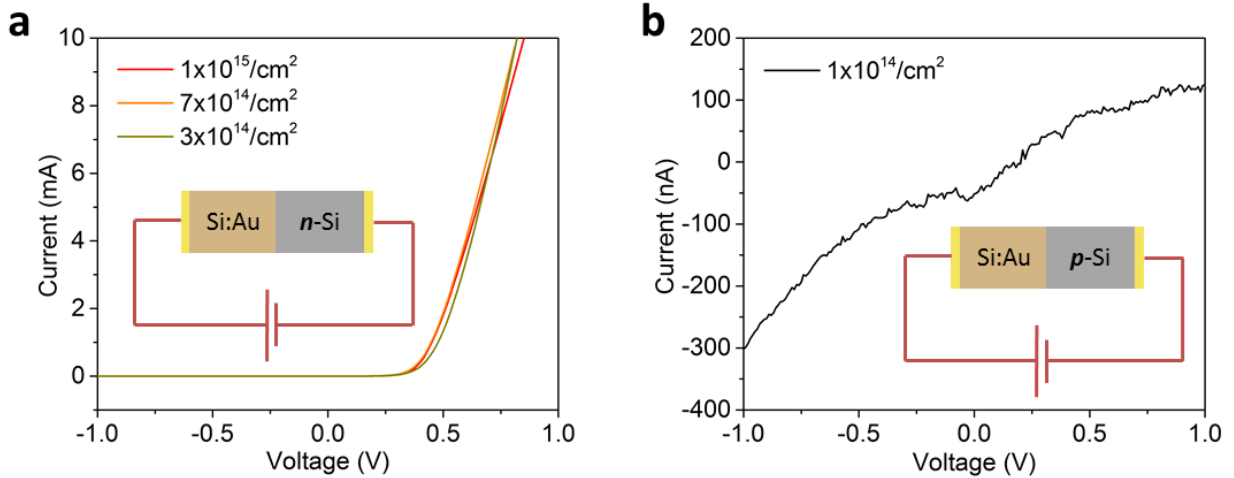

Figure 2.5. Si:Au doping type determination by rectification test

2.2.6. EQE Calculation for Photodiode Steady-State Photoresponse

Using Fourier transform, a 2 V peak-to-peak square wave $S(t)$ can be expressed as $S(t) = 1.273\sin(\omega t) + 0.4244\sin(3\omega t) + 0.2546\sin(\omega t) + \ldots$ where *ω* is the angular frequency and *t* is time. Because the optically chopped light can be approximated as a square wave and the lock-in amplifier output V_{out} is the RMS value of the first Fourier component of the signal, the mapped EQE for each coordinate on the photodiode can be calculated using the formula $EQE(x, y) = 2.22V_{out}(x, y)/Rq\phi(\lambda)$, where V_{out} is the signal output from the lock-in amplifier, *R* is the value of the comparative resistor, *q* is the electron charge and $\phi(\lambda)$ is the number of photons incident on the sample per unit time measured using a calibrated germanium photodiode. The Si:Au photodiodes were operated at –5 V reverse bias for these EQE measurements.

2.2.7. Modeling of Fully-Depleted Hyperdoped Region in Si:Au Diode

When *I*-*V* responses of Si:Au photodiodes were measured under large reverse biases, it was observed that the dark current increases almost linearly with the increase in reverse bias voltage. This is in contrast to that of a non-depleted diode which normally approach a steady dark current following the diode equation $I = I_o\left(e^{qV/kT} - 1\right)$. A simple diode model to simulate this behavior was developed in the PC1D device simulator. A ***p***-type emitter layer with a thickness of 150 nm and a low carrier lifetime of 20 ps is used to represent the Si:Au layer. The base is represented with an ***n***-type silicon with 500 μm thickness and 180 μs carrier lifetime (parameter obtained from the actual substrate). PC1D simulation shows that the hyperdoped Si:Au region is indeed fully depleted, and that the resulting dark IV curve shows the same linear behavior for large reverse bias voltages (**Figure 2.6**).

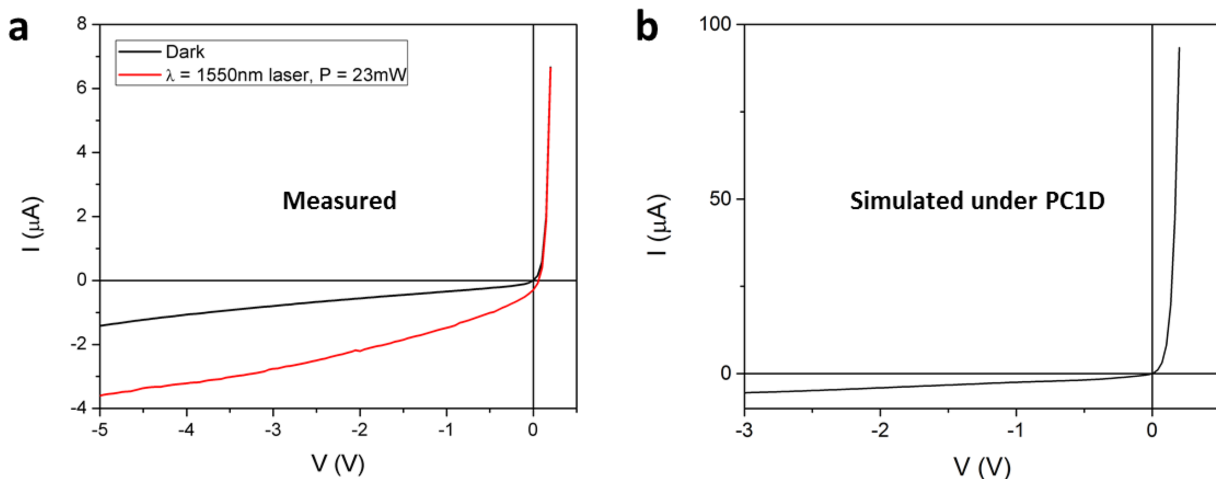

Figure 2.6. Comparison of measured and simulated Si:Au photodiode *I*-*V* curve

(**a**) IV curve of Si:Au photodiode with 10^{15}/cm^2 gold implantation dose under dark and illuminated condition with sub-band gap light, measured at the position with maximum EQE. (**b**) Simulated dark current-voltage characteristics of Si:Au diode with fully depleted hyperdoped layer, showing linear reverse bias IV characteristics which has been experimentally observed.

2.2.8. Transient-Pulse Photoresponse

The laser pulse with 10 ns FWHM exiting the optical parametric amplifier (OPA) consisted of the sub-band gap signal wavelength (λ_s), the idler wavelength (λ_i), as well as possible leakage of other above-band gap wavelengths (λ_a) due to the inner working of the OPA. λ_a was first filtered out using a razor-edge 1064 nm long pass edge filter (Edmund Optics, NT47-510). The resulting beam was further purified by dispersing it using Pellin Broca prism mounted on a rotation stage and selecting only the desired wavelength (λ_s) with a subsequent aperture. The rotation stage was calibrated such that across the entire spectral range considered only λ_s could illuminate the sample. IR ND filters mounted on a filter wheel were then used to tune the beam intensity. This experimental setup is illustrated in **Figure 2.7**.

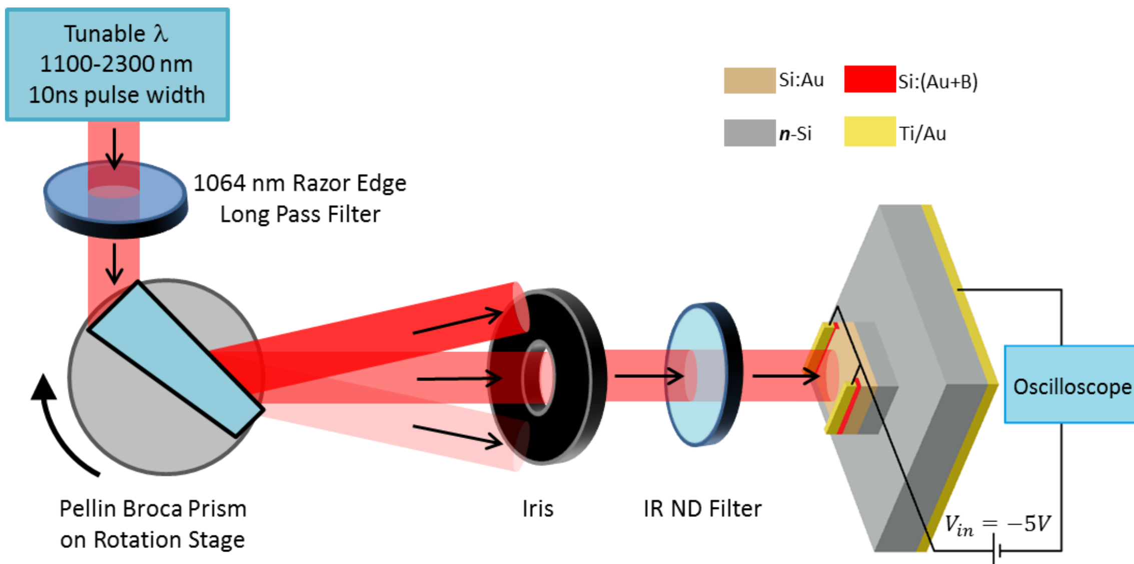

Figure 2.7. Tunable-wavelength transient photoconductivity setup

The sub-band gap pulse laser light from the optical parametric amplifier (OPA) was filtered using 1064 nm razor edge long pass filter to remove any above-band gap light shorter than 1064 nm. The light was then dispersed using Pellin Broca prism mounted on a computer-controlled rotation stage. Light with the desired wavelength passed through the iris, and the light intensity is controlled using a set of IR neutral-density filters mounted on a filter wheel.

The intensity was chosen such that the magnitude of the transient voltage was much smaller than the supply voltage V_{in} to prevent signal saturation. Furthermore, the beam intensity was also chosen such that the signal due to two-photon absorption (TPA) in the substrate was minimized (**Section 2.2.9**). The majority of the sub-band gap photoconductivity signal in the Si:Au photodiode originated from the carriers generated in the thin ***p***-type Si:Au layer and were quickly swept across the junction into the ***n***-type substrate, resulting in a signal with the similar pulse shape and FWHM as the incoming pulse laser. However, the sub-band gap signal from the reference silicon photodiode came from TPA across the entire substrate and lasted for tens of μs. An average of 200 pulses was used for the acquisition of each data point. Example of sub-band gap photoresponse signal obtained from an Si:Au photodiode and a reference silicon photodiode in this experiment is shown in **Figure 2.8** for λ_s = 1400 nm.

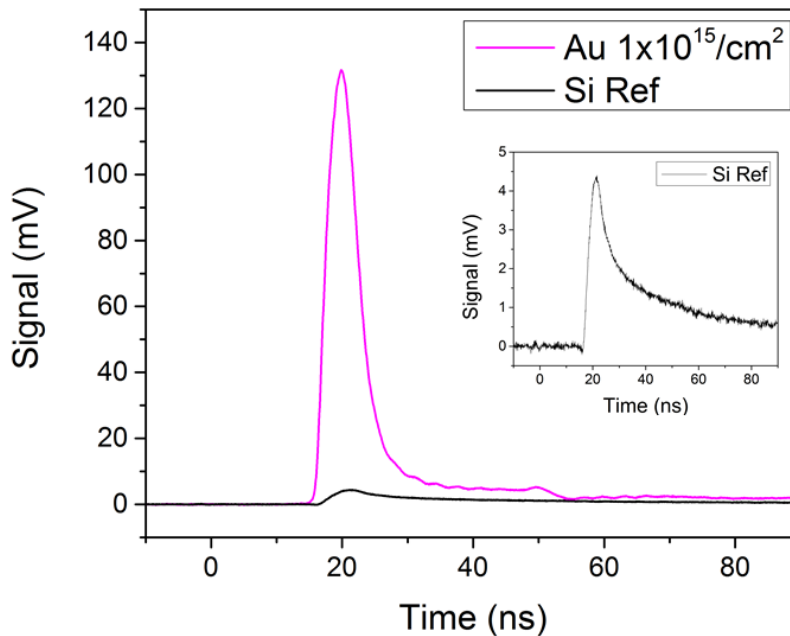

Figure 2.8. Si:Au Sub-band gap transient photoresponse signal

2.2.9. Two-Photon Absorption Model for Photodiode Background Response

As can be seen in **Figure 2.8**, we still see a small sub-band gap transient photoresponse from the reference silicon photodiode even though it is not supposed to have any sub-band gap photoresponse. This small background photoresponse is caused by two-photon absorption (TPA).[63] One of the characteristics of TPA is characterized by the sub-band gap absorption coefficient $\alpha_{TPA}(\lambda) = I(\lambda)\beta(\lambda)$ where $I(\lambda)$ is the intensity of the pulse laser used and $\beta(\lambda)$ is the published value of two-photon absorption coefficient[63] for each wavelength. The value of $\beta(\lambda)$ for λ = 1200 - 2200 nm is about 1 cm·GW^{-1}. The maximum pulse laser energy in our transient photoresponse experiment is about 100 μJ per pulse with ~0.5 cm beam diameter. Because the laser pulse full-width-half-maximum (FWHM) is about 10 ns, the maximum instantaneous intensity of the laser pulses incident on the photodiode samples are 50 kW·cm^{-2}. In this case, maximum $\alpha_{TPA}(\lambda)$ of 5×10^{-5} cm^{-1} can be approximated. This absorption coefficient is very small, and consequently for *L* = 0.5 mm thick silicon reference photodiode that we used in our experiment the total sub-band gap light intensity absorbed due to TPA can be approximated as $I_{ABS}(\lambda) \propto I(\lambda)(1 - \exp(-\alpha_{TPA}(\lambda)2L)) \propto I^2(\lambda)\beta(\lambda)2L$. The photoresponse signal observed in the oscilloscope is directly proportional to this value, hence the quadratic dependence of the signal to the photon intensity as we show later in **Section 2.3.2**. The corresponding value for the dimensionless figure of merit *η* is obtained by dividing the photoresponse signal with the sub-band gap photon illumination. Hence we have the proportionality relationship $\eta(\lambda) = AI(\lambda)\beta(\lambda)$ to model the TPA background sub-band gap photoresponse (**Section 2.3.2**), where *A* is the normalization constant.

2.3. Results & Discussion

2.3.1. Steady-State Room-Temperature Sub-Band Gap Photoresponse

To measure the room-temperature sub-band gap photoresponse in Si:Au, photodiodes were fabricated (**Section 2.2.4**). An identical photodiode was fabricated on the same substrate but with the Si:Au layer replaced by boron-doped silicon (Si:B) as a reference sample (**Figure 2.4**). The photodiodes were then connected to a comparative resistor, a lock-in amplifier, and a voltage source (V_{IN} = –5 V) that placed the devices under reverse bias (**Figure 2.9**). A diode laser (optically chopped at frequency f = 714 Hz) was focused to a 100 – 150 μm spot size on the photodiode surface. The comparative resistor value of R = 1 kΩ was chosen such that the reverse bias voltage across the photodiodes was close to 5 V ($I_{dark}R << |V_{in}|$). The laser spot was then scanned across the photodiode surface. Sub-band gap optoelectronic response was observed only in the 1×1 mm^2 area of the photodiode corresponding to the electrically connected Si:Au region.

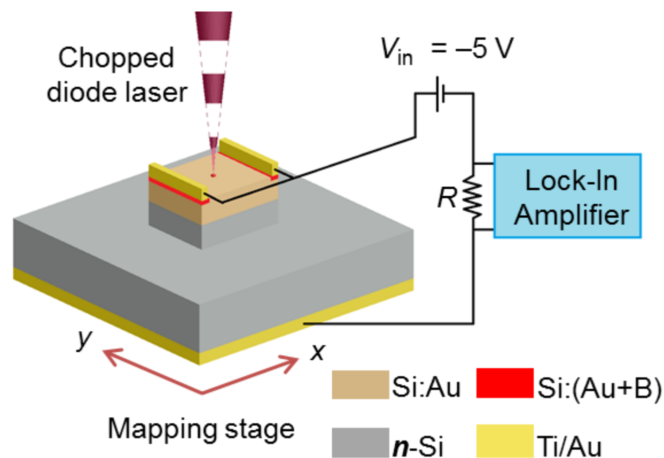

Figure 2.9. Spatially-mapped steady-state sub-band gap EQE measurement setup

Si:Au photodiode with Si:Au layer on ***n***-Si substrate operating at reverse bias. The optically chopped diode laser light is focused to 100-150 µm spot size and is scanned across the photodiode surface.

A map of sub-band gap response at λ = 1550 nm is shown in **Figure 2.10** for a sample with implantation dose of 10^{15} Au cm^{-2}. The spatial uniformity of the photoresponse within the 1×1 mm^2 area demonstrates that internal photoemission from the metal contact electrodes is not the dominant cause of the sub-band gap photoresponse.[64] The reference Si:B photodiode control samples did not show any measurable sub-band gap optoelectronic response (**Figure 2.10**), further confirming that the Si:Au layer is the origin of the room-temperature sub-band gap photoresponse.

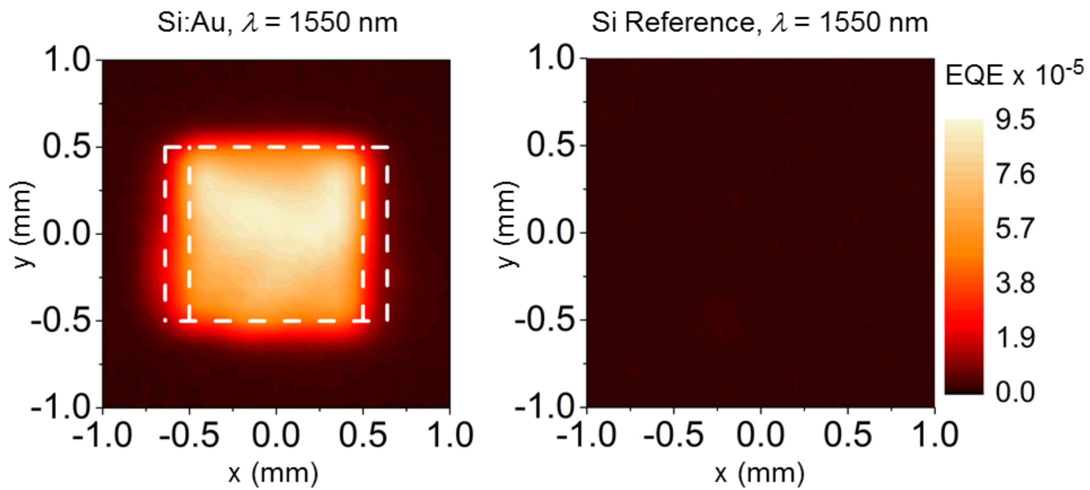

Figure 2.10. Spatially-mapped sub-band gap photoresponse of Si:Au photodiode

Mapped external quantum efficiency (EQE) showing a 1×1 mm^2 Si:Au active area for λ = 1550 nm and gold implantation dose of 10^{15} cm^{-2}, confirming the Si:Au layer as the sole source of the sub-band gap photoresponse in the photodiode. No sub-band gap response is observed when the Si:Au is replaced with Si:B in the reference silicon photodiode.

This observation is in contrast with the low-temperature sub-band gap photoresponse previously reported in titanium-hyperdoped silicon, where the sub-band gap photoresponse of the reference crystalline silicon is reported to be larger than that of the titanium hyperdoped silicon.[65] The sub-band gap photoresponse measurements on the Si:Au photodiodes under 5 V reverse bias were performed with different sub-band gap wavelengths (λ = 1310, 1550, and

1650 nm); spatially optimized external quantum efficiency (EQE) measurements for sub-band gap wavelengths for all Au doses are shown in **Figure 2.11**. Si:Au photodiode response increases monotonically with increasing gold concentration for all three sub-band gap wavelengths, with the maximum EQE of 2.8×10^{-4} and 9.3×10^{-5} for λ = 1310 nm and 1550 nm, respectively. More detail about the EQE calculation can be found in **Section 2.2.6**.

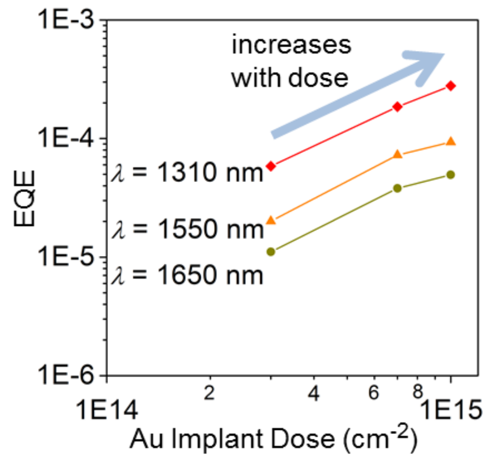

Figure 2.11. Au dose dependence of Si:Au photodiode sub-band gap photoresponse

2.3.2. Room-Temperature Spectral Response of Si:Au Photodiodes

The extent and mechanism of Si:Au room-temperature optoelectronic spectral response was further studied *via* transient photoresponse measurements. Nanosecond pulses with tunable wavelengths (λ = 1100 – 2300 nm) were derived from an optical parametric amplifier (OPA)[66] pumped by a frequency-tripled, Q-switched Nd:YAG laser. The pulses were passed through a long pass filter and a Pellin Broca prism to eliminate any undesired wavelengths (e.g. laser harmonics) prior to incidence upon the photodiode (**Section 2.2.8**).

The shape of the spectral responses for the Si:Au photodiode with 1×10^{15} cm^{-2} implant dose and the reference Si:B photodiode are shown in **Figure 2.12**. Due to the high intensity of

the sub-band gap laser pulse, a sub-band gap photoresponse signal appeared within the reference silicon sample due to two-photon absorption (TPA).[63] This signal responded quadratically with pulse intensity, as expected for a two-photon process, and could be reduced by tuning the pulse intensity appropriately. The spectral response in the reference sample agrees well with the calculated value expected for TPA, $I(\lambda)\beta(\lambda)$ where $I(\lambda)$ is the intensity of the pulse laser used and $\beta(\lambda)$ is the published value of two-photon absorption coefficient[63] for each wavelength (**Section 2.2.9**).

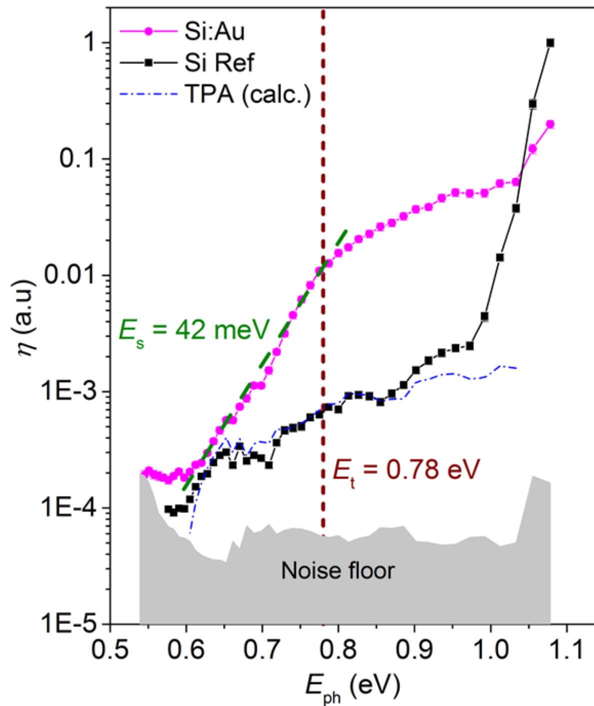

Figure 2.12. Sub-band gap spectral response of Si:Au photodiode

Si:Au spectral response η as a function of photon energy measured using tunable-wavelength transient photoresponse measured at room-temperature for the photodiode with the highest gold dose of 10^{15} cm^{-2}. A kink in the spectral response is observed at the threshold energy E_t = 0.78 eV, which corresponds to the substitutional gold donor level in silicon. For $E_{ph} < E_t$, the response is characterized by the Urbach absorption edge with a slope of E_s = 42 meV.

Figure 2.13 shows the strength of the photoresponse signal with respect to the applied laser pulse intensity for both above gap and sub-band gap light. The photoresponse increased

linearly with increasing laser pulse intensity except for the sub-band gap photoresponse in the reference silicon sample, which increased quadratically with increasing laser intensity due to TPA.

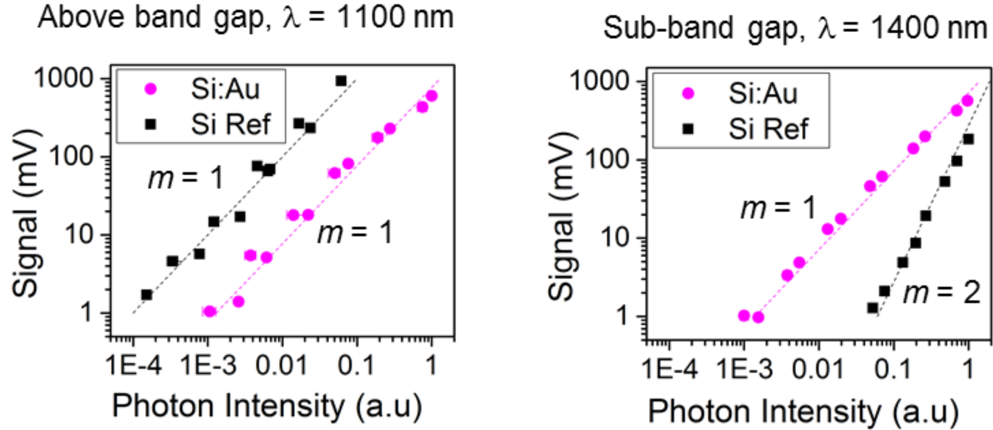

Figure 2.13. Linear intensity dependence of Si:Au sub-band gap photoresponse

Above band gap and sub-band gap photoresponse of the Si:Au and reference silicon photodiodes for varying photon intensity, confirming that the sub-band gap response in the reference silicon is caused by two-photon absorption (TPA) in the substrate. Under standard operating conditions (~100 W·cm^{-2} or lower), no measurable TPA was observed in the reference silicon photodiode.

In addition to the different scaling with photon intensity, the TPA signal was easily distinguished from the photoconductive signal because the transient decay of the response was much slower (**Figure 2.8**). This characteristic should be expected for TPA because free carriers were generated and had to be collected from the entire silicon substrate. To mitigate the effect of TPA from both Si:Au and reference silicon spectral response in **Figure 2.12**, only the short-lived peak of the transient signal was used in the definition of the dimensionless figure of merit $\eta = A \cdot \Delta I_{\text{peak}} / N_{\text{ph}}$, where A = 4.8 × 10^{21} A^{-1} is a normalization constant, ΔI_{peak} is the photo-generated current and N_{ph} is the number of photons in the laser pulse. We observe measureable spectral response of Si:Au extending to E_{ph} = 0.55 eV, and a distinct change in

slope at photon energy E_{ph} = 0.78 eV (**Figure 2.12**). This later spectral feature appears to be dopant specific, as discussed in the next section.

2.3.3. Origin of Sub-Band Gap Photoresponse in Si:Au Photodiode

I will first comment on the likely origins of the sub-band gap photoresponse of Si:Au. In previous studies,[67–69] Sah and Okuyama utilized temperature-dependent photoconductivity and spectrally-resolved low-temperature photoconductivity measurements, respectively, to determine the energy levels of gold impurities in silicon with a gold concentration below the solid-solubility limit. At these low dopant concentrations, the Au-induced defect states are single, discrete levels with non-interacting localized states. In that study,[69] the reported spectral response has a distinct change in slope near the photon energy E_{ph} = 0.78 eV, which corresponds to the substitutional gold donor energy level in silicon. In our study, the same spectral feature was observed in the Si:Au photodiode with a gold dose of 1×10^{15} cm^{-2}, suggesting that the sub-band gap photoresponse mechanism in these Si:Au photodiodes may be the same as that in gold-diffused silicon measured at liquid-nitrogen temperature.[69] The higher gold concentration achieved by our PLM process apparently enables one to observe this effect at room-temperature.

Next, I address the role of "drift" in carrier extraction from the Si:Au layer. It is known that deep-level traps such as Au in silicon reduce the electronic carrier lifetime through non-radiative recombination.[70] Assuming a gold concentration of $N_t = 10^{20}$ cm^{-3} and a saturated electron velocity of $v_s = 10^7$ $cm\cdot s^{-1}$ in the depleted Si:Au layer,[71] an electron trapping rate σ_{eo} $=(\sigma_n^t v_s N_t)^{-1}$ = 5 ps would be expected given an electron capture cross section $\sigma_n^t = 2\times10^{-16}$ cm^2

of gold in silicon.[72] Despite the low minority-carrier lifetime in Si:Au, some free electrons excited by the sub-band gap light in the hyperdoped region were able to escape into the ***n***-type substrate. This process is aided because the Si:Au layer is fully depleted due to the low carrier concentration in gold doped silicon (**Section 2.2.7**). This low carrier concentration in the Si:Au layer is believed to be caused by the self-compensation due to the ionization of deep acceptor and donor trap levels of substitutional gold in silicon.[62,73,74] The resulting full depletion of the Si:Au causes the majority of the applied reverse bias voltage to drop across this layer, thereby facilitating carrier transport *via* drift.

This behavior is in contrast with results from past work in sulfur-hyperdoped silicon,[46] where the free carrier concentration is between 10^{17} – 10^{20} cm^{-3} and the minority-carrier transport in the hyperdoped region is driven by the comparatively weaker process of diffusion.[48] The application of 5 V reverse bias across the hyperdoped layer appears sufficient to saturate the photoresponse. This is shown in **Figure 2.14**, where the photo-generated current produced by λ = 1550 nm light saturates with increasing reverse bias voltage for photodiode with 10^{15} cm^{-2} gold dose (calculated from the difference of photodiode current in the dark and under illumination). Increasing reverse bias across the junction increases carrier drift velocity in the Si:Au layer, which also improves the collection of photo-carriers excited by the sub-band gap light. While higher gold concentration is expected to reduce the sub-band gap photoresponse by reducing the minority-carrier lifetime, the applied reverse bias voltage seems to be capable of overcoming the negative effect of higher gold concentration. Hence, the sub-band gap optoelectronic response increases with the increasing sub-band gap absorptance in samples with higher gold concentrations (**Figure 2.11**).

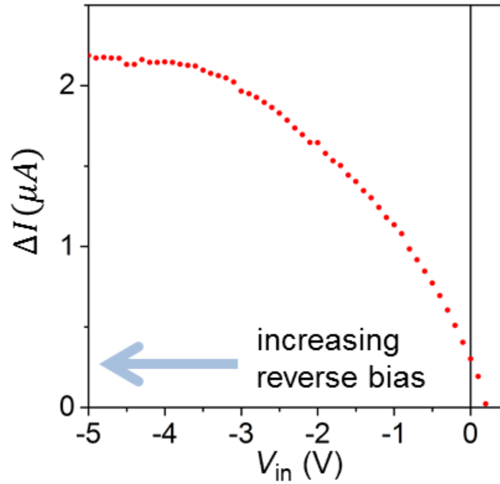

Figure 2.14. Bias voltage dependence of Si:Au photodiode sub-band gap photoresponse

2.3.4. Spectral Response Dependence to Hyperdoped Silicon Dopant Type

Next, we discuss how the dopant type affects the IR spectral response. In this dopant-mediated, extrinsic sub-band gap photoresponse mechanism, electrons can be excited into the conduction band through the dopant state(s). One likely mechanism is the electron excitation from the valence band to the conduction band through the donor energy level, which has previously been shown for gold-diffused silicon at low temperature (**Figure 2.15**).[69,75]

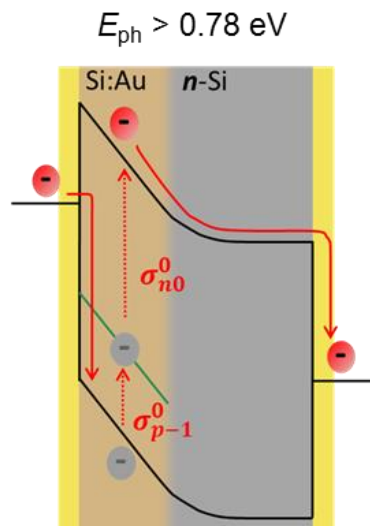

Figure 2.15. Possible sub-band gap photoresponse mechanism in Si:Au photodiode

In previous work,[69,75] donor-assisted transition arises at threshold energy close to 0.78 eV. Inspecting **Figure 2.12**, similar threshold energy is evident in the Si:Au photodiode. For photon energy E_{ph} larger than the threshold energy E_t = 0.78 eV,[55] the transitions characterized by photoionization cross section σ_{p-1}^{0} (from valence band to the donor state) and σ_{n0}^{0} (from donor state to the conduction band) are both possible. Electrons from the valence band can then be excited into the conduction band and be swept away by the strong reverse bias electric field across the Si:Au layer into the ***n***-type substrate. They are then transported as majority-carriers in the conduction band before being extracted by the back contact. However, for $E_{ph} < E_t$ the transition from the donor level to the conduction band characterized by σ_{n0}^{0} is turned off; thus, electrons excited into the donor level eventually recombine into the valence band without leaving the Si:Au hyperdoped region. Because the donor-level/conduction-band transition is unavailable, the magnitude of the sub-band gap response for the energy range $E_{ph} < E_t$ becomes exponentially less likely with decreasing excitation energy. One possible model for this exponential decay is the dependence $\eta(E_{ph}) \propto \exp((E_{ph} - E_t)/E_s)$ where E_s is the slope of the Urbach absorption edge due to disorder in solids.[76] E_s = 42 meV has been extracted from fits to the experimental data as the slope of the Urbach edge (**Figure 2.12**). This is larger than kT = 26 meV, suggesting that there is a disorder induced broadening in either the impurity states or the conduction band edge of Si:Au. The spectral kink at E_{ph} = 0.78 eV closely matches the spectral response of gold-diffused silicon at low-temperature, suggesting that it should be possible to tune the sub-band gap spectral response of hyperdoped silicon by using alternative dopant elements that introduce levels at different energies.[69]

Further analysis can be done on the spectral response of Si:Au for E_{ph} > 0.78 eV. Various models have been proposed to explain the dependence of the photoionization cross section $\sigma(E_{ph})$ for deep levels in semiconductor. If the deep level wavefunction is a localized state with delta function like spatial dependence in the length scale of the atomic radius, for E_{ph} close to the threshold energy E_t = 0.78 eV the approximate dependence $\sigma(E_{ph}) \propto (E_{ph} - E_t)^{1/2}$ is expected.[77,78] In contrast, for a state with hydrogenic like wave function the approximate dependence $\sigma(E_{ph}) \propto (E_{ph} - E_t)^{3/2}$ is expected.[79] The conversion efficiency η (**Figure 2.12**) is directly proportional to the photoionization cross section in the Si:Au photodiode, and as such the dependence $\eta(E_{ph}) \propto (E_{ph} - E_t)^n$ for E_{ph} close to E_t = 0.78 eV can be used to infer the spatial behavior of the deep level wavefunction. The range for the fit is set to 0.8 eV < E_{ph} < 0.94 eV to reduce the influence of the Urbach edge, and the fit is shown in **Figure 2.16**. The polynomial dependence of n = 0.6 is extracted, suggesting that the deep level state wavefunction for the donor level of Si:Au has a spatial dependence much closer to that of a delta function[77,78] than that of a hydrogenic wavefunction,[79] consistent with a deep (localized) level.

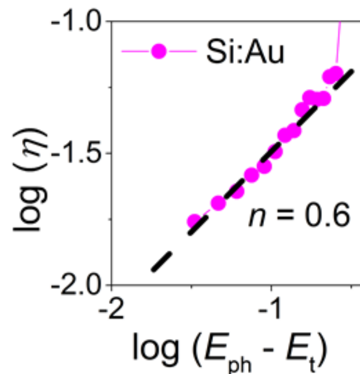

Figure 2.16. Polynomial dependence of sub-band gap photoresponse conversion efficiency *η*

2.4. Conclusions & Perspective

As these are first demonstration devices, there is room to improve the room-temperature sub-band gap photoresponses from their current EQE's of ~10^{-4}. Two focus areas are suggested; improving sub-band gap light absorptance and incorporating best-in-class photodiode-design practices to enhance carrier collection. This can be achieved, for example, by using a larger gold implantation dose for the PLM process and applying an anti-reflection coating on the photodiode to increase the sub-band gap absorptance of the Si:Au layer beyond its current ~1 % absorptance. Increasing the thickness of the Si:Au layer could also increase the optical path length and sub-band gap absorptance. Further gains may be possible *via* optimization of device design: because most of the gold dopants are concentrated near the silicon surface (**Figure 2.2**), the majority of free carriers generated by sub-band gap light are believed to be within the top 20 nm of the Si:Au surface. Because the surface-limited lifetime for W = 20 nm thick silicon is in the order of $\tau_s = W/S$ = 2 ps when a non-passivated surface recombination velocity $S = 10^6$ cm·s^{-1} is assumed,[80] the sub-band gap photoresponse in Si:Au with a bulk lifetime of ~5 ps is prone to surface recombination. Incorporating surface passivation could potentially suppress this recombination activity. We conservatively estimate that practical application of these improvements may increase the room-temperature sub-band gap optoelectronic response of Si:Au photodiodes by two orders of magnitudes to EQE = 10^{-2}, although no physical limits are known at this time to prevent even higher EQE. Unfortunately, while sub-band gap EQE = 10^{-2} may be useful for an infrared photodetector, it will not be useful for an intermediate band solar cell because it is too small. Furthermore, the EQE = 10^{-2} result can only be obtained under reverse bias voltage (**Figure 2.14**), while solar cells need to operate

under forward bias voltage for useful energy generation, making this mechanism even less likely to be useful for solar cell applications.

In summary, I report the room-temperature sub-band gap optoelectronic response in silicon hyperdoped with gold using a two-step process: ion implantation followed by pulsed laser melting. The sub-band gap optoelectronic response is shown to correspond to known gold dopant energy levels in silicon and increase with the implanted gold concentration. This work represents a fundamentally new approach to achieve sub-band gap optoelectronic response in silicon that avoids structural defects and interface management issues associated with combining foreign materials and silicon. While the magnitude of the room-temperature sub-band gap response demonstrated here is in the EQE ~ 10^{-4} range, further improvements are likely *via* device architecture optimization. The planar, single crystal nature of the hyperdoped silicon layer created using the PLM process makes this an attractive material candidate for room-temperature sub-band gap photon imaging devices based on silicon. Nevertheless, it is very unlikely for hyperdoped silicon to be a useful method for developing an efficient intermediate band solar cell.

Chapter 3: Demonstration of Perovskite/Silicon Tandem Solar Cell

There are three main sections in this chapter. The content of the first main section (**Section 3.2**) is mainly taken from an article I have previously co-authored in in Energy & Environmental Science,[19] for which the publisher Royal Society of Chemistry (RSC) has granted permission for co-authors to re-publish in a thesis.[81] The content of the second main section (**Section 3.3**) is mainly taken from articles I have published in Applied Physics Letters[20] and Proceedings of IEEE Photovoltaic Specialist Conference,[21] for which publishers American Institute of Physics (AIP) and IEEE have also granted permission for co-authors to re-publish in a thesis.[82,83] The content of the third main section (**Section 3.4**) are early results which have not been published. My main contribution on this work has been on the design, fabrication and characterization of the bottom silicon sub-cells, as well as the interlayers between the perovskite and silicon sub-cells. In **Section 3.2**, my contribution is on the entire bottom silicon sub-cells. In **Section 3.3**, my contribution is on the entire bottom silicon sub-cells, the silicon tunnel junction, and the TiO_2 layer deposited using atomic layer deposition. In **Section 3.4**, my contribution is on the entire bottom silicon sub-cells and the silicon tunnel junction. The design and fabrication of the perovskite sub-cells, as well as the characterization of the full tandem solar cells, are performed by my co-authors.

3.1. Background

Solar-to-electricity conversion efficiency is the technical variable that most strongly influences silicon (Si) photovoltaic (PV) module costs.[84,85] The record efficiency of crystalline silicon (c-Si) single-junction PV devices has increased from 25% to 25.6% during the last fifteen

years,[3,86] asymptotically approaching the 29.4% Auger-recombination-constrained Shockley-Queisser limit.[2] To make PV modules with higher efficiency than market-leading c-Si while leveraging existing c-Si manufacturing capacity, Si-based tandem approaches have been proposed.[19,87–90] The top sub-cell in a silicon-based tandem should have a band gap between 1.6 and 1.9 eV.[91] However, very few materials exhibit high open-circuit voltages (V_{OC}) within this band gap range. One example in GaInP; other members of the III-V compound semiconductor family are also an option. However, these materials require complex and expensive manufacturing processes such as molecular beam epitaxy (MBE) or metal-organic chemical vapor deposition (MOCVD).[92,93] Past top-cell efforts have also included dye-sensitized,[94] bulk-heterojunctions,[95] II-VIs,[96,97] and nanowire[98] cells as the top sub-cells, although promising low-cost top sub-cell for silicon remains elusive. As it stands, commercial options for tandems do not currently achieve both low-cost and high-efficiency. Tandems made exclusively with organic semiconductors and amorphous silicon-based compounds have only moderate efficiencies of ~10-13%,[99,100] which offset the advantage of lower areal cost ($\$/m^2$) and result in higher $/W than industry-standard crystalline silicon.

Recently, the organic-inorganic-lead-halide perovskite has demonstrated a rapid efficiency increase[101–105] (**Figure 3.1**) with a V_{OC} of 1.15-1.2 V.[106,107] The perovskite itself simply denotes a material with ABX_3 crystal structure. As it currently stands, the efficiency record of 1J thin-film perovskite solar cell is already at 22.1% in academic research laboratories.[4] It is already comparable to the efficiency records of thin-film CdTe (First Solar, at 22.1%) and copper-indium-gallium-diselenide (CIGS, Solar Frontier, at 22.3%) solar cells optimized in company R&D lines.[4]

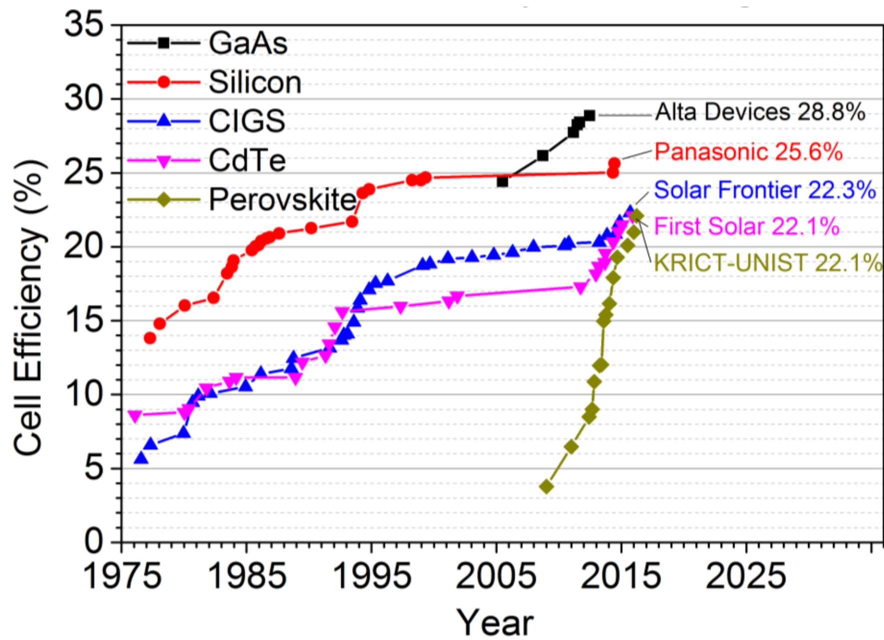

Figure 3.1. Rapid efficiency record increase of 1J perovskite solar cells

The efficiency record progression for 1J solar cells over the years shows much faster learning curve for perovskite compared to other classes of solar cell materials. Figure is adapted from the National Renewable Energy Laboratory (NREL) efficiency record chart,[4] extended with early perovskite devices which are not recorded in the NREL chart. This rapidly-evolving chart is valid as of March 17, 2016.

The organic-inorganic-lead-halide perovskite material family also has tunable band gaps, ranging from 1.48 to 2.3 eV depending on the halide (iodine, bromine) and cation (methylammonium, formadinium, cesium) composition (**Figure 3.2**),[107,108] though not all compositions are currently stable under illumination.[109] In addition to having high efficiency, perovskite solar cells are attractive because they achieve high efficiencies exceeding 20% under AM1.5G illumination, even though the absorber material is a polycrystalline film solution-processed at low temperature. This means that in addition to being earth-abundant and having low absorber film manufacturing cost, the material is also inherently tolerant to intrinsic defects,[110] making it an attractive material to be paired in tandem with silicon solar cells.

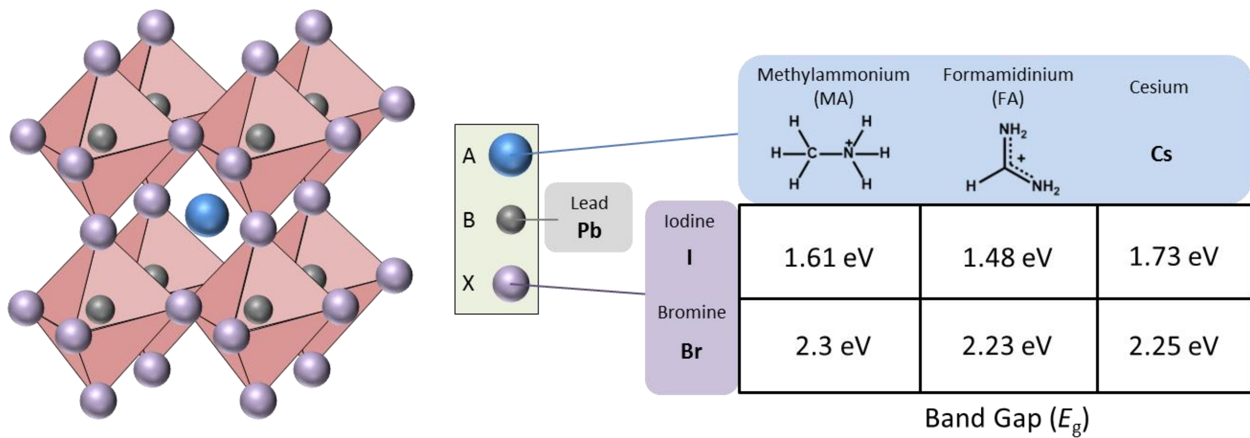

Figure 3.2. Perovskite crystal structure and band gap tenability

The ABX_3 perovskite crystal structure; in the context of perovskite solar cells the A site is filled by either methylammonium (MA), formadinium (FA), or cesium (Cs) while the X site is filled by either iodine (I) or bromine (Br). The B site on the other hand, has so far been filled by lead (Pb) for optimal performance; no attractive substitute for Pb has been found. Band gap tunability can be achieved by intermixing the composition of cations in the A site, the anions in the X site, or both.

When a material with E_g = 1.12 eV is used as the bottom sub-cell for tandem with properly chosen top sub-cell (E_g = 1.72 eV for 2T and E_g = 1.82 eV for 4T tandem), the tandem efficiency limit increases to 44.1% and 44.5% respectively, compared to the S-Q limit of 32.6% for 1J cell with E_g = 1.12 eV. If Auger recombination (which is intrinsic to silicon) is considered, the efficiency limit decreases to 29.4% for 1J silicon[2], 42.5% and 42.6% for 2T and 4T perovskite/silicon tandem, respectively.[111] The perovskite/silicon tandem architecture aims to reach high efficiency as well as low cost by utilizing a defect-tolerant technology such as perovskites as the top cell and an established commercial technology such as silicon as the bottom cell.[89] By using a silicon cell on the bottom, the perovskite/silicon tandem directly benefits from the value of a proven large scale, commercially viable technology and from any future incremental improvements to the silicon cell technology by the solar industry.

3.1.1. Rapid Prototyping of 4T Tandem using Inexpensive Silicon

To demonstrate perovskite/silicon tandem solar cells, I first designed and fabricated infrared (IR)-optimized ***p***-type silicon solar cells for the 4T tandem configuration (**Section 3.2**).[19] A 4T tandem typically has a larger manufacturing cost because the sub-cells are fabricated independently. However, we realize that in a perovskite/silicon tandem solar cell more than 60% of the power is being generated in the top perovskite sub-cell. Because of this, it may make sense to use inexpensive silicon as the bottom sub-cell. Because the power contribution from the bottom silicon sub-cell is smaller, there is significantly less efficiency penalty for a 4T tandem compared to a 1J silicon cell for the usage of inexpensive silicon.

Most silicon solar cells are made using high-purity silicon. The purity of a crystalline silicon wafer has strong dependence to the purity of the silicon feedstock used in the silicon crystal growth process. Single-crystal wafers made for the microelectronics industry need to be extremely pure, and hence are made using 9N to 11N electronic grade polysilicon (9N = 99.9999999% pure). This level of polycrystalline silicon (poly-Si) feedstock purity is achieved using the Siemens process.[112,113] First, powdered metallurgical grade silicon (MG-Si, 98% pure) is reacted with hydrochloric acid (HCl) at 300 °C to form trichlorosilane gas (TCS gas, $SiHCl_3$). Impurities inside the silicon (such as Fe, Al, B, etc) form their halides ($FeCl_3$, $AlCl_3$, BCl_3, etc) instead, so the TCS gas can be purified from the rest of the impurity halide by distillation ($SiHCl_3$ boiling temperature is low, at 31.8 °C). The resulting TCS is pure from electrically active impurities of less than 1 part-per-billion-atomic (ppba). Finally, the purified TCS is reacted with hydrogen at 1100 °C for ~200-300 hours to form very pure poly-Si. This poly-Si is grown on thin poly-Si rods in large vacuum chambers, producing high-purity poly-Si rods (9N) with diameters

of 150–200 mm (**Figure 3.3**).[112] These 9N poly-Si rods are eventually crushed, and used as the feedstock for the growth of monocrystalline (c-Si) silicon ingot using the Czochralski process. The resulting c-Si wafers from this process are commonly used by the microelectronics industry. Less intensive Siemens process with lower purity produces feedstock which is often used to make multicrystalline (mc-Si) silicon for the solar industry.

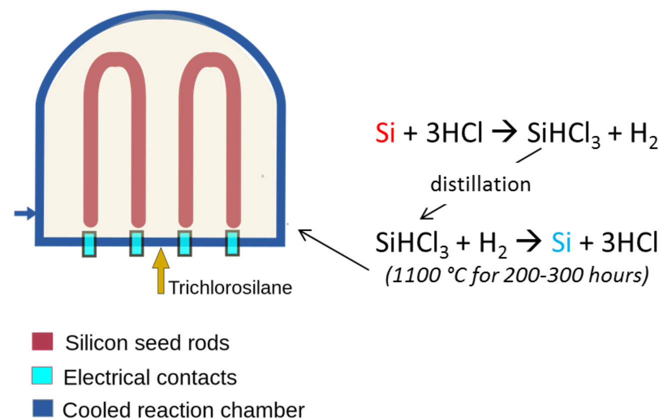

Figure 3.3. Siemens process for 9N–11N pure Si feedstock production

Siemens process reactor image (left) taken from Wikipedia under permission from the copyright holder.[112] Red indicates the original MG-Si material, while blue indicates the purified silicon feedstock.

On the other hand, solar grade silicon for 1J silicon cells may not need to be as pure. Fluidized bed reactor (FBR) is a lower-cost manufacturing technology which regularly produces poly-Si feedstock at 6N to 9N purity.[114,115] First, silicon tetrachloride ($SiCl_4$) is reacted with silicon and hydrogen gas to form TCS. The TCS is distilled (similar to in the Siemens process), and the purified TCS dissociates to form silicon tetrachloride and pure silane (SiH_4) gas (**Figure 3.4**), ideally at temperature between 600–1100 °C.[114,115] While this process produces lower-purity poly-Si feedstock, silicon production using the FBR process enables lower cost with 80-90% less energy than the traditional Siemens method.

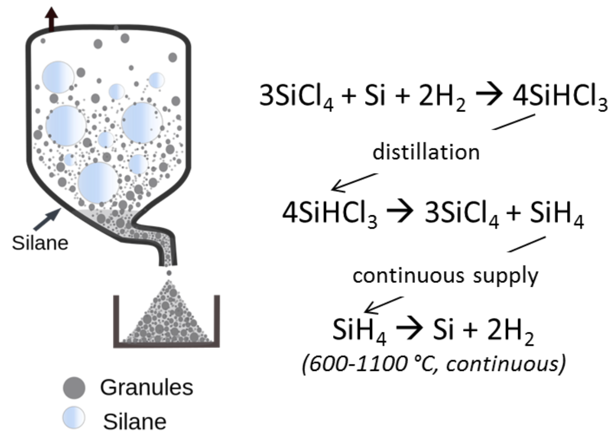

Figure 3.4. FBR process for 6N–9N pure Si feedstock production

FBR process reactor image (left) taken from Wikipedia under permission from the copyright holder.[112] Red indicates the original MG-Si material, while blue indicates the purified silicon feedstock.

Instead of using poly-Si made from the Siemens process or the FBR process, the feedstock for my cast mc-Si wafers are 4.5N (99.995% pure) upgraded metallurgical silicon (UMG-Si) or recycled silicon from the top 10% of a cast industrial mc-Si ingot (top ingot silicon, TI-Si). For the UMG-Si upgrade process, MG-Si is purified by the combination of metallurgical techniques.[113] For example, MG-Si may first be refined by oxidation for B removal, then vacuum treated for P removal, with directional solidification finally applied to remove metal impurities before the ingot is cut into wafers.[113] On the other hand, TI-Si is simply recycled from unused multicrystalline industrial ingot (which usually uses 6N to 9N for the silicon feedstock purity). In a directional solidification process commonly used to make the multicrystalline silicon ingots, the top 10% of the ingot is typically thrown away due to the high content of impurity dissolved in the block during the solidification process. This top 10% block from the ingot is recycled as the feedstock for TI-Si wafer fabrication (**Figure 3.5**).

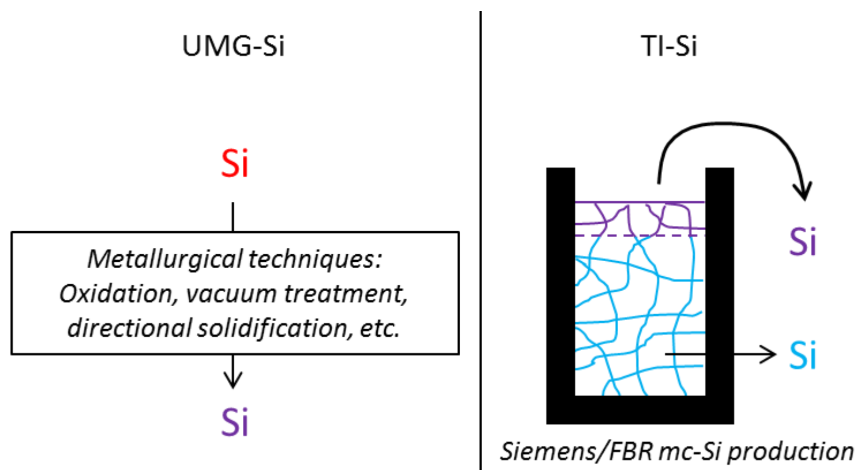

Figure 3.5. UMG-Si and TI-Si feedstock production process flow

UMG-Si feedstock is made from MG-Si (red) further purified by metallurgical techniques. On the other hand, TI-Si feedstock is made by taking the top 10% of industrial mc-Si ingot grown using pure feedstock made by the Siemens or the FBR processes. The bottom 90% of the ingot is typically pure (blue), while the top 10% (Ti-Si) has lower purity because impurities aggregate in the liquid during crystal solidification process from the bottom to the top. The low-purity silicon feedstock (UMG-Si and TI-Si) are purple-colored.

I designed and fabricated 4T perovskite/silicon tandem using inexpensive silicon wafers (both UMG-Si and TI-Si are used) as the material for the bottom silicon sub-cells. This work is performed in collaboration with the McGehee group (Stanford University), which fabricated the semi-transparent perovskite cells made from methylammonium-lead(II)-iodide ($CH_3NH_3PbI_3$ or also known as $MAPbI_3$, E_g = 1.61 eV) to be used in tandem with my bottom silicon sub-cells. The independent nature of sub-cells' fabrication enables us to rapidly prototype the first 4T perovskite/silicon tandem cells; for which the 4T tandems have improved efficiencies over either 1J sub-cell efficiencies. In this work, combining a 12.7% perovskite solar cell (1J) and an 11.4% silicon solar cell (1J) resulted in a 4T tandem efficiency of 17.0%.[19]

The 4T architecture (**Figure 1.8**) relaxes performance constraints such as current matching and the need for tunnel junctions while enabling optimization of the top and bottom cells separately. In this 4T tandem, the top and bottom cells are fabricated independently and

mechanically stacked upon one another. The performance of each cell is measured separately and added together to arrive at the tandem efficiency. If desired, current matching between the top and bottom strings of cells could be achieved at the module level by adjusting the cell area and numbers of cells per string. This configuration would allow the module to have only two leads exiting the module and a single inverter, similar to conventional single-junction modules. The engineering and manufacturing simplicity, ease of integration into existing silicon solar cell fabrication lines, and compatibility with common installation methods make 4T tandems an attractive option for commercialization.

3.1.2. Designing 2T Tandem with *n*-Type Silicon Cell

Nevertheless, it is likely that the manufacturing cost per unit area will be lower for a 2T tandem when compared to a 4T tandem. A 2T perovskite/silicon tandem solar cell may be constructed *via* monolithic integration where a thin film perovskite sub-cell is deposited directly onto the c-Si sub-cell. Monolithic integration requires electrical coupling between sub-cells and transmission of infrared light to the bottom sub-cell. I use an interband tunnel junction[116] to facilitate electron tunneling from the electron-selective contact of the perovskite sub-cell into the ***p***-type emitter of the *n*-type silicon sub-cell. This approach stands in contrast to the recombination layer used in other perovskite tandem systems[117] but is widely used in III-V[118] and micromorph (a-Si/µc-Si)[119] tandem solar cells. Unlike the tunnel junction in III-V tandem solar cells, my tunnel junction is made of silicon with an indirect band gap, enabling electrical coupling with minimal parasitic absorption. The conduction-band alignment between silicon and the perovskite sub-cell's electron-selective contact (TiO_2) enables bypassing the usage of a transparent conducting oxide (TCO) recombination layer, an alternative option with greater

parasitic absorption. Again, I collaborate with the McGehee group, who deposited the top perovskite sub-cell made of $CH_3NH_3PbI_3$ ($MAPbI_3$) in this work.[120] We present the device design, fabrication, characterization, and loss analysis of monolithic perovskite/silicon tandem solar cells in **Section 3.3**.[20,21]

3.1.3. Designing 2T Tandem with *p*-Type Silicon Cell

In the early days of perovskite solar cells, the thin-film perovskite cell needs to be grown from the electron contact to the hole contact, due to processing constraints. More specifically, the perovskite absorber layer cannot be exposed to the high processing temperature required to sinter the electron contact (TiO_2, sintered at 450-500 ^oC).[19,121] This means if the standard perovskite solar cell deposition processes are used for the 2T perovskite/silicon tandem cell fabrication, the perovskite solar cell grown on top of silicon needs to be grown with the electron contact on the bottom and the hole contact on the top. In this configuration, holes in the perovskite travel upward while the electrons travel downward, so an ***n***-type silicon bottom sub-cell has to be used.[20,122] However, the majority of silicon solar cell manufacturing still relies on ***p***-type silicon cell. We recognize that ***n***-type silicon solar cells are likely to play important role in the silicon solar cell industry in the future. However, a 2T perovskite/silicon tandem architecture fabricated on a ***p***-type silicon solar cell will be necessary to take advantage of current silicon cell manufacturing capacity and expertise and ease the industry transition from a 1J silicon cell to a 2T perovskite/silicon tandem cell.

Many recent advances in the perovskite solar cell community relax this processing constraint. For example, phenyl-C61-butyric acid methyl ester (PCBM) deposited at room-temperature has been used as a replacement for TiO_2 as the electron contact for perovskite.[123] NiO_x has also been found to be a good hole contact for perovskite solar cells, making it an attractive inorganic alternative for 2,2',7,7'-Tetrakis-(N,N-di-4-methoxyphenylamino)-9,9'-spirobifluorene (spiro-OMeTAD).[124] Based on these advances, we designed an inverted 2T perovskite/silicon tandem solar cell, for which the perovskite cell grown on top of a silicon cell was grown with the hole contact on the bottom and electron contact on the top. Now electrons in the perovskite travel upward while the holes travel downward, so a standard ***p***-type silicon bottom sub-cell can be used. We present early device design, fabrication, and characterization of monolithic perovskite/silicon tandem solar cell on ***p***-type silicon cells in **Section 3.4**.

3.2. IR-Optimized Silicon Cells Made from Inexpensive Silicon for 4T Tandem

3.2.1. Materials & Methods

3.2.1.1. Selection of Inexpensive Silicon for Tandem

I fabricated our silicon solar cells from inexpensive ***p***-type multicrystalline silicon wafers, which had high impurity content.[19] This decision was made because the bottom silicon sub-cell in a tandem produces roughly 1/3 of the power output, which may justify the usage of inexpensive, lower-purity silicon wafers. I used both UMG-Si wafers and TI-Si wafers to fabricate the bottom silicon sub-cells. The UMG-Si wafers were donated by Sunpreme Inc., while the TI-Si wafers were donated by Schott Solar Inc.

3.2.1.2. *p*-Type Silicon Cell Fabrication

I fabricated ***p***-type silicon solar cells using UMG-Si and TI-Si wafers.[19] The ***p***-type cell fabrication process flow is shown in **Figure 3.6**. These ~200 µm-thick wafers were subjected to saw-damage removal wet etch in CP4 solution (15:5:2 HNO_3:CH_3COOH:HF) for 2 cycles of 2 minutes etching, resulting in ~180 µm thick wafers. The wafers were then cleaned using RCA1 (5:1:1 H_2O:NH_4OH:H_2O_2) and RCA2 (5:1:1 H_2O:HCl:H_2O_2) solutions at 70 °C for 10 minutes each, to remove organic and metallic surface contaminants. The wafers were then loaded into a Tystar $POCl_3$ diffusion furnace at 700 °C for phosphorus emitter formation. After ramping up the furnace temperature to 865 °C, $POCl_3$ gas was flowed into the furnace for 12 minutes, followed by 6 minutes of N_2 purge. After waiting for an extra time of 10 minutes, I purged the furnace chamber with O_2 for 7 minutes followed by temperature ramp down of ~ 3 °C/minute. The samples were then unloaded at 500 °C. This concludes the emitter fabrication process.

At the end of the diffusion process, phosphorus emitters with diffusion depths of 200–300 nm and emitter sheet resistances of ~35 Ω/□ were formed on both sides of the wafer. I removed the phosphosilicate glass (PSG) layer formed on the wafers surface by dipping them in buffered oxide etch (BOE 5:1) solution for approximately 30 s. The wafers then underwent another round of RCA clean before I deposited SiN_x anti-reflection coating (ARC) using plasma-enhanced chemical vapor deposition (PECVD). The SiN_x PECVD process was done in an STS PECVD tool at a temperature of 300 °C. While this PECVD temperature is not high enough to enable good silicon passivation using SiNx (400-450 °C is recommended),[125] this is the highest processing temperature allowed in the shared cleanroom PECVD tool we use in Harvard Center for Nanoscale Systems (CNS). After this SiN_x PECVD step, the standard Si cells (for 1J

applications) had ARC thicknesses of ~82 nm, while the cells optimized for infrared light (for 4T tandem applications, relevant spectral response from 800–1100 nm) had ARC thicknesses of ~125 nm. I protected the front side of the wafer by spinning Shipley 1805 photoresist at 4000 rpm for 40 s and baking the photoresist at 115 °C for 1 minute. I then removed the backside emitter by SF_6 reactive ion etch (RIE) with a rate of ~1 µm/min to etch ~1 µm deep in an STS RIE tool.

Finally, we proceeded with front and back metallization. We deposited 1 µm thick Al on the backside of the wafer using *e*-beam evaporation, followed by rapid thermal annealing (RTA) at 900°C for 30 s in N_2 atmosphere to form aluminum back surface field (Al BSF) at the back of the wafer. After this annealing step, the thickness of the ARC layers shrank down to 78 nm (optimized for standard AM1.5 illumination) and 115 nm (optimized for IR response). We defined our finger area of the cells using photolithography. We spun double layer photoresist to enable smooth lift-off process. First, LOR 20B photoresist was spun at 4000 rpm for 40 s, and baked at 180 °C for 4 minutes. Afterwards, Shipley 1805 photoresist was spun at 4000 rpm for 40 s, and baked at 115 °C for 1 minute. The back side was then protected using single-layer Shipley 1805 photoresist spun at 4000 rpm for 40 s, baked at 115 °C for 1 minute. The resulting front side double-layer photoresist film was exposed to UV for 2 s using Karl Suss MJB4 Mask Aligner to pattern the front metal finger opening, and then developed in CD-26 developer solution for 75 s. After the double-layer photoresist was patterned, the samples were cleaned using O_2 plasma cleaner (75 W & 40 sccm for 20 s).

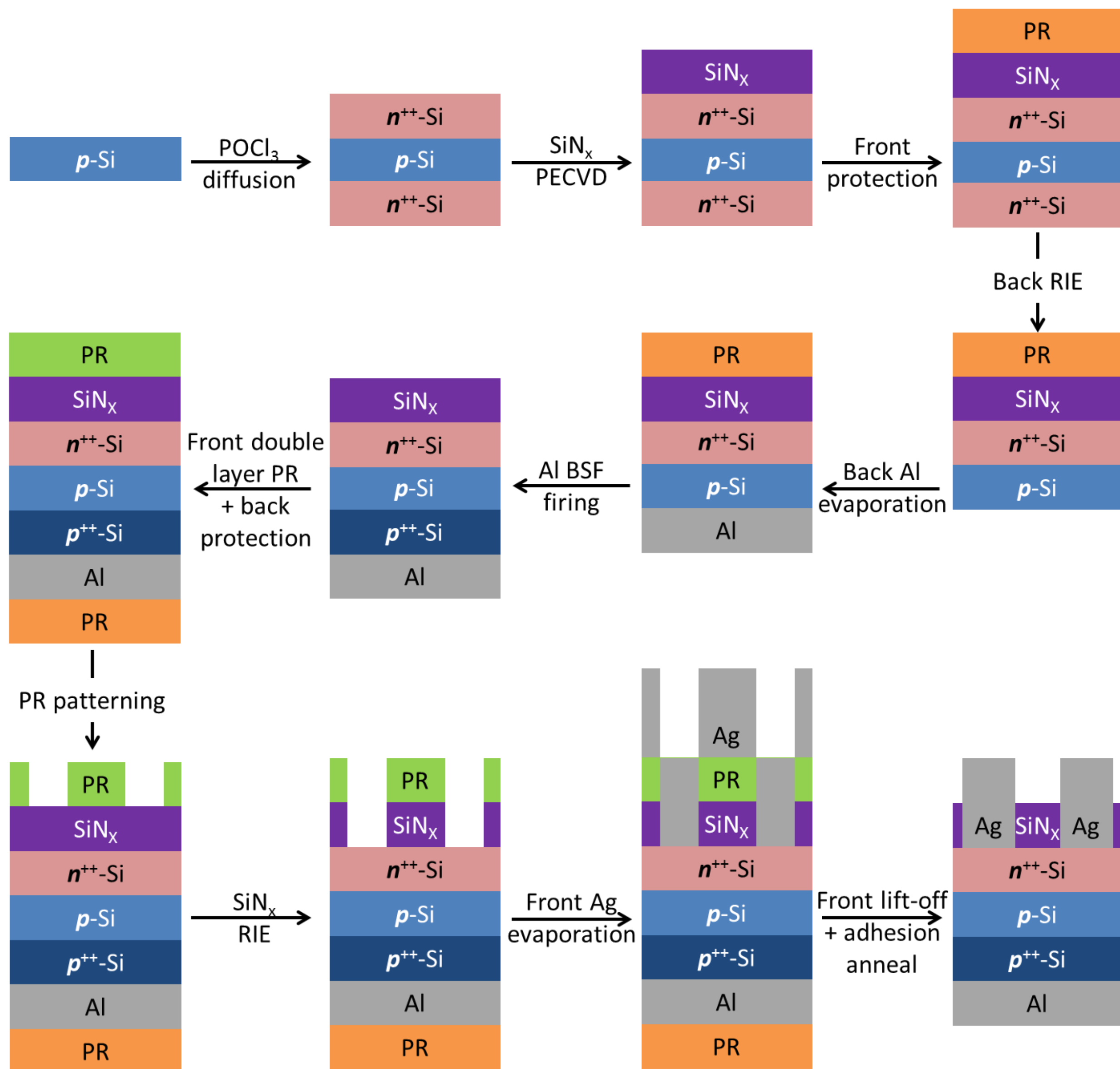

Figure 3.6. *p*-type silicon cell fabrication process flow

The process flow for silicon solar cell fabrication using ***p***-type wafer. The green photoresist (PR) indicates double-layer photoresist used for the lift-off process. This process is intended to produce ***p***-type solar cells which are similar to full-area Al BSF ***p***-type solar cells which dominate the photovoltaic industry today. For this application, we used inexpensive silicon made from UMG-Si or TI-Si, instead of the high-quality multicrystalline silicon normally used in the industry today. At the end of the process, the SiNx thickness was either 78 nm (1J) or 115 nm (IR-optimized for 4T tandem). The device schematic is not for scale.

Finally, the photoresist was used as etching mask for patterning the SiN_x on the metal finger area using RIE. We then deposited 20/20/300 nm Ti/Pd/Ag metal stack as the finger, for which Ti acted as the adhesion layer, Pd acted as the diffusion barrier, and Ag acted as the conductive layer. Lift-off process in PG-Remover solution was used to form the metal fingers. After the samples were cleaned in acetone, isopropyl alcohol (IPA), and de-ionized (DI) water, the samples underwent RTA at 400°C for 5 minutes in argon atmosphere for metal adhesion. The cells were finally cut out of the wafers by laser scribing followed by mechanical cleaving. **Based on follow-up iterations, it is better to use 20/20/200 nm Ti/Pd/Ag finger stack for better lift-off.**

At the end of this process, I obtained silicon solar cells optimized for different spectrums AM1.5G illumination (for 1J) and IR-optimized (for 4T) for both ***p***-type silicon cells made from UMG-Si and TI-Si. Example of EQE spectrum for TI-Si cell is shown in **Figure 3.7**.

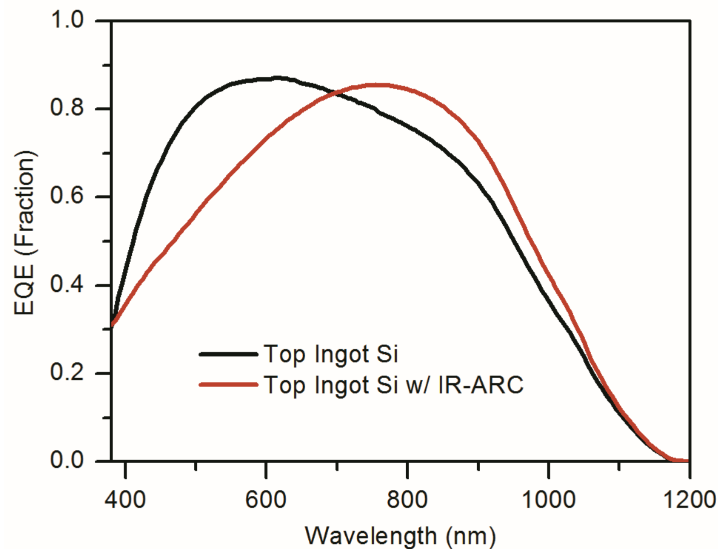

Figure 3.7. EQE of 1J and IR-optimized 4T silicon cell made from inexpensive silicon

3.2.1.3. Semi-Transparent Perovskite Cell Fabrication

This entire section (**Section 3.2.1.3**) of the work concerning semi-transparent perovskite cell fabrication is wholly developed by our collaborators in the McGehee and the Salleo group, Stanford University.[19] Mechanically-stacked tandems require a semi-transparent top cell, as illustrated in **Figure 1.8**. We used a mesoporous titanium dioxide (TiO_2) layer infiltrated with the perovskite and contacted on either side by electron-selective (compact TiO_2) and hole-selective (spiro-OMeTAD) contacts.[104] For compatibility with these existing electron- and hole-selective contacts, we used the $MAPbI_3$ perovskite rather than the optically ideal $MAPbBrI_2$. $MAPbBrI_2$ was also not chosen due to a photo-instability observed in this material.[126] The transparent front electrode was fluorine-doped tin oxide (FTO) coated glass. Typically, a perovskite solar cell is opaque with an approximately 100-nm-thick metal back electrode of either Au or Ag. This metal back electrode provides a low-resistance electrical contact and a reflective surface, giving the perovskite a second chance to absorb any light that was not absorbed on the first pass. To enable the transparency required to make a mechanically-stacked tandem, we need a transparent top electrode.

The technical constraints that the top transparent electrode must meet are stringent. The electrode must be highly transparent in the critical 600–1000 nm window where the perovskite is not absorbing all of the light and the bottom cell has significant EQE. The sheet resistance of the transparent electrode should be at most 10 Ω/□[127] because the transparent electrode must have high lateral conductivity to minimize resistive loss when carrying the large current density generated in the perovskite cell. Perhaps most importantly, this electrode must be applied after deposition of the spiro-OMeTAD layer onto a temperature- and solvent-

sensitive perovskite solar cell without damaging it. For these reasons, high-performance transparent conductive oxides widely used in industry cannot be directly sputtered onto a perovskite solar cell without a buffer layer. An electrode meeting these criteria had not been demonstrated before this work. We used a silver nanowire (AgNW) mesh electrode which had been shown in other cases to have a low sheet resistance and high optical transmission[128–130] and developed a new method of depositing this electrode onto our perovskite cell in a room-temperature solvent-free process. This AgNW electrode served as the linchpin for our mechanically-stacked tandem architecture.

We first formed our AgNW transparent electrode on a flexible polyethylene terephthalate (PET) film by spray deposition following the method which had previously been described[128] with several modifications. The spray nozzle was positioned 76 mm above the substrate. The AgNW dispersion sprayed here contained 4.5 mg of AgNWs. This value was chosen such that the transmission/conductivity tradeoff of the AgNW electrode maximizes the power conversion efficiency of the tandem. The deposition was carried out on 5 mil thick Polyethylene terephthalate (PET). The choice of PET as a substrate for the AgNW film is important for the transfer lamination technique for reasons described below. The spray deposition was carried out at the elevated temperature of 60 °C to increase the conductivity of the AgNW electrode. PET has a glass transition temperature of about 70 °C and so higher deposition temperatures and further annealing, although desirable, could not be used here. The nanowires used here averaged 35 nm in diameter and 15 µm in length.

This spray deposition process yielded a 50 × 300 mm^2 of AgNW transparent electrode on PET. This was then cut with scissors into pieces approximately matching the perovskite substrate size. The electrodes were patterned by selectively applying and then removing kapton tape to eliminate AgNWs in desired regions. The AgNW film on PET was stored at ambient laboratory conditions for two weeks before transfer lamination. The resulting AgNW film has a sheet resistance of 12.4 Ω/□ and exhibits 90 % transmission between 530 and 730 nm falling off to 87 % at 1000 nm. The light transmission spectrum of this AgNW film on a PET substrate is shown in **Figure 3.8**.

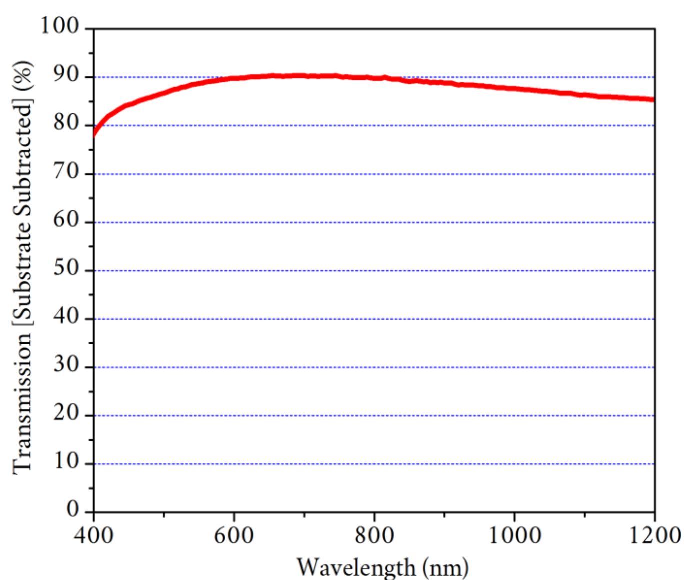

Figure 3.8. Transmission spectrum through AgNW film laminated on PET substrate

Once the AgNW film on PET substrate was ready, we fabricated the perovskite solar cell devices. Pilkington TEC15 FTO glass (1.6 and 2.2mm) was patterned by selective etching with Zn powder (J.T. Baker, 4282-01), 4M HCl (Fisher, A144-212), and mechanical abrasion with a cotton swab. The glass was cleaned by sonication in a diluted Extran solution (EMD, EX0996-1), acetone (EMD, AX0115-1), and isopropanol (IPA) (EMD, PX1835P-4). After 20min of UV-ozone

treatment, the glass was heated to 500 °C on a hotplate. A 1:10 dilution of titanium diisopropoxide bis(acetylacetonate) (Aldrich - 325252) in ethanol (Sigma-Aldrich, 187380) was repeatedly sprayed from an airbrush nozzle to achieve ~50 nm thick films of TiO_2 on top of the FTO. After cooling down, the glass was immersed in a 70 °C batch of 40 mM $TiCl_4$ (Sigma-Aldrich, 208566) in ultrapure water (J.T. Baker, 6906-02) for 30 minutes. The glass was then rinsed in DI water and dried on a 70°C hotplate for 15 minutes. After cooling down, mesoporous TiO_2 films were spun onto the TiO_2/FTO surface at 4000 rpm for 30 s and sintered at 450 °C. The spin-coating solution was a 1:3 dilution of 18-NRT TiO_2 paste (Dyesol) in ethanol.

All previous steps were performed in ambient atmosphere. The remainder of device fabrication was performed in a nitrogen glovebox with < 5 ppm O_2 and H_2O. The TiO_2 substrates were dried by heating to 500 °C with a hot air gun for 30 min and immediately brought into the glovebox. A 1.3 M PbI_2 solution was prepared by dissolving PbI_2 (Aldrich, 211168) into anhydrous DMF (Acros, 32687) and stirring on a hotplate at 100°C. The DMF was filtered through a 200 nm PTFE filter (Pall, 4552) prior to adding to the solution in order to remove particulates. Methylammonium Iodide (MAI) was synthesized according to a previously reported procedure.[102] A solution of 10 mg MAI per 1 mL anhydrous IPA (Acros, 61043) was prepared and allowed to dissolve at room temperature. A pure IPA rinse solution was prepared as well. The IPA was filtered through a 20 nm PTFE filter prior to adding to the solutions in order to remove particulates.

After the TiO_2 substrates were cooled to room temperature, 100 µL of the 100°C PbI_2/DMF solution was pipetted onto the substrate and spun at 6500 rpm for 90 s. The resulting

film was translucent yellow and dried for 30 min on a 70°C hotplate. After cooling, the films were dipped in the MAI/IPA solution. The films were monitored optically for the formation of the perovskite (**Figure 3.9**). The signal at 700 nm was used to determine the growth rate of the perovskite, while the signal at 850nm was used to detect the presence of other optical phenomena (changes in scattering, reflection, incident light intensity). When the derivative of both signals matched, the formation was considered complete and the perovskite film was removed, rinsed in IPA, dried by spinning at 4000 rpm for 30 s, and placed back on the 70 °C hotplate for 30 minutes. At this point, the films were translucent brown.

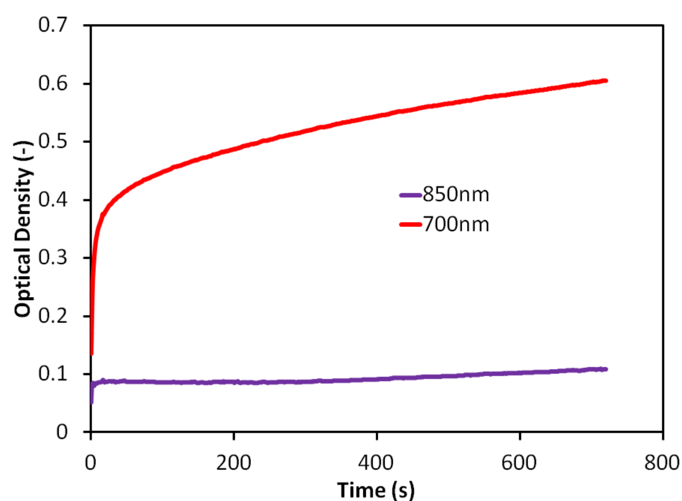

Figure 3.9. Optical density over time of perovskite film in dipping solution

After cooling, 75 µL of a spiro-OMeTAD (Lumtec, LT-S922) solution was spun on top at 4000 rpm for 30 s. The spiro-OMeTAD solution was 59 mM (for opaque devices) and 163 mM (for semi-transparent devices) in anhydrous chlorobenzene (Sigma-Aldrich, 284513). The spiro-OMeTAD was dissolved by placing on a hotplate at 70°C for > 30 minutes. 193 mM of tert-butyl pyridine (Aldrich, 142379) and 31 mM of Li-TFSI (Aldrich, 15224) dissolved as 520 mg/mL in anhydrous acetonitrile (Acros, 61096) were added to the 59 mM spiro-OMeTAD solution. For

the 163 mM spiro-OMeTAD solution, the amount of tert-butyl pyridine and Li-TFSI was kept consistent with respect to the concentration of the spiro-OMeTAD. In this study, 8 mol% of the spiro-OMeTAD was spiro-OMeTAD$(TFSI)_2$, resulting in 16% of spiro-OMeTAD molecules being chemically oxidized to ensure conductivity in the spiro-OMeTAD layer. The spiro-OMeTAD$(TFSI)_2$ was synthesized as reported elsewhere in literature.[131] After the spiro-OMeTAD solution was prepared, it was filtered through a 20 nm Al2O3 filter (Whatman, 6809-3102) to remove any aggregates and particulates. Films were then removed from the glovebox and stored overnight in a desiccator at 20% RH. This concludes the fabrication of the perovskite cell up to right before back contact deposition. For the opaque electrode devices, 100 nm Au was thermally evaporated through a patterned shadow mask to form the back electrode. For the semi-transparent devices, an AgNW film on PET was used.

The AgNW film we have previously stored was then completely and uniformly donated from the PET to the top spiro-OMeTAD layer of the perovskite solar cell by mechanical transfer ideally without damaging the sensitive AgNW or perovskite films. The patterned AgNW film on PET was placed facedown onto the nearly completed perovskite device so that the AgNWs were in contact with the top spiro-OMeTAD layer. A 0.17 mm thick glass coverslip was placed on top of the PET substrate. The AgNWs were transfer laminated from the PET to the perovskite solar cell by applying approximately 500 g of downward force onto the coverslip through a single ¼-inch diameter ball bearing. The bearing was selectively rolled over the active area of the perovskite device so that the AgNW film was completely and uniformly donated from the PET to the top spiro-OMeTAD layer of the perovskite solar cell. The rolling action of the bearing reduced lateral shear force on the PET preventing any movement of the donor PET substrate

relative to the acceptor perovskite solar cell. Lateral movement here caused discontinuities in the laminated AgNW film severely degrading its conductivity. The flexibility and softness of the PET substrate allowed the AgNW film to conform to the surface of the perovskite device during transfer despite any dust or other imperfections that may be present on either the surface of the AgNW film or the surface of the spiro-OMeTAD layer. This, coupled with the relatively small contact point of the ball bearing ensured complete transfer lamination of the AgNW film to the perovskite device without damaging the mechanically sensitive nanostructured AgNW film in the presence of dust or other imperfections.

The 500 g transfer force was chosen to be sufficient to ensure the AgNWs were completely donated from the PET but not too much that they were forced through the spiro-OMeTAD layer causing bridges/shunts across it. AgNW bridges across the spiro-OMeTAD layer led to increased recombination since the spiro-OMeTAD layer could no longer effectively block electrons and in extreme cases shunting of the device if the AgNWs bridge through the TiO_2 as well. The coverslip served two purposes. First, it isolated the lateral movement of the ball bearing from the PET, which prevented cracks, or discontinuities in the transferred AgNW film as described above. Second, it served to increase the area over which the force from the ball bearing was applied to the PET, thus reducing the pressure felt by the AgNWs during the transfer process. This reduced pressure was a further safeguard against AgNWs bridging through the spiro-OMeTAD layer.

Tips For Reproduction:

For those with interest towards reproducing this work, we would like to stress a few points in our procedure above that we have found to be the most critical in fabricating the semi-transparent perovskite devices.

- Avoid a perovskite overlayer and make the spiro-OMeTAD layer thick. Planarization of the top surface is important for ensuring the complete transfer of the silver nanowire electrode. To a lesser degree, it also improves the transmission through the device by decreasing scattering.
- Transfer the silver nanowires with as little pressure as possible. A very low and consistent pressure is required to avoid pressing the wires through the spiro-OMeTAD film and making direct contact with the perovskite. This is also the function served by the glass coverslip.
- Develop a surface coating on the wires to make them more stable. Our laboratory environment has normal oxygen levels as well as a small partial pressure of sulfur gas added to the environment. While we have no direct proof of a coating on the silver nanowires, we believe either an oxide or a sulfide layer was formed on the surface of the wires. Silver oxide and sulfide are much more stable than metallic silver in the presence of iodine (which readily forms silver iodide) and improve the resistance of the electrode to corrosion. We see that electrodes stored in the laboratory environment prior to transfer onto a device are much more stable than electrodes stored in an inert nitrogen atmosphere. We set aside one of these devices for long-term testing and it

showed no change in performance over a month of storing in the dark in desiccated air. There is certainly room to improve on this procedure by intentionally introducing an oxide or sulfide layer onto the nanowires or by coating the surface with other materials (*e.g.*,. ligands, a gold coating, *etc*.)

- Wait for the spiro-OMeTAD layer to dry before transfer. Possibly the spiro-OMeTAD film is too soft while still wet. Our results were much more inconsistent and had lower efficiencies when we tried transfer onto a wet spiro-OMeTAD layer. We achieved our best results by allowing the device to dry overnight in a flow desiccator.
- Test devices before evaporating anti-reflection coatings. The LiF anti-reflection coating seems to act as an effective seal against ingress of gas. For us, however, perovskite devices need to be exposed to light and oxygen to achieve their best performance (we believe the necessity is in the perovskite layer itself, not the spiro-OMeTAD layer), otherwise there is a slight s-kink near the maximum power point. Testing in the middle of fabrication gets rid of this s-kink permanently; then the anti-reflection coating can be added.

After transfer of the AgNW electrode, 100 nm Ag was thermally evaporated through a patterned shadow mask around 3 edges of the devices. These bars of silver helped reduce the unnecessary series resistance in the AgNW electrode by not limiting the current collection to one geometrical direction. The nearly completed device was stored in a desiccator for 12 hours before applying the anti-reflective coatings. LiF anti-reflective coatings were then added to the semi-transparent devices. 133 nm LiF was deposited onto the glass surface. This was optimized to provide anti-reflection for the broad solar spectrum from 400–1100 nm. 176 nm LiF was

deposited onto the AgNW mesh. This thickness was optimized to provide anti-reflection for the infrared spectrum from 800–1100 nm.

Because this is a research-stage procedure, the applied force of the mechanical transfer was manually rather than automatically controlled. Variability in the applied force can cause shorting (high pressure) as well as incomplete transfer (low pressure), resulting in a spread of device efficiencies,[19] as shown in **Figure 3.10**. Automated precise control of the applied force is expected to remove these inconsistencies. As a result of the transfer, the conductivity of the AgNW film typically improved by 2 Ω/□. The primary reason for this increase in conductivity was the planarization of the AgNW film due to the downward force of the transfer lamination process, which reduced the resistance of junctions between wires.[132] A secondary effect was that the AgNWs had been embedded into the moderately conductive spiro-OMeTAD layer (~10^{-3} S/cm)[131] on top of the perovskite device.

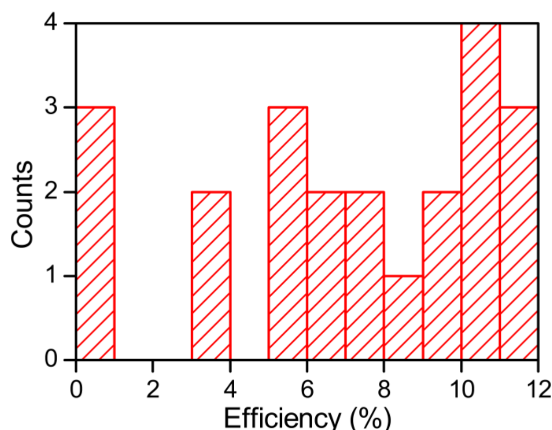

Figure 3.10. Semi-transparent perovskite device efficiency distribution

This transfer step decoupled the fabrication of the perovskite solar cell from that of the electrode, allowing each to be optimized independently. Independent fabrication eliminated any thermal or solvent damage that the spiro-OMeTAD or perovskite might otherwise incur

during the AgNW deposition process. We completed the semi-transparent solar cell by depositing two lithium fluoride (LiF) anti-reflective (AR) coatings, 133 nm onto the glass surface and 176 nm on top of the AgNW electrode to improve transmission through the device.

3.2.1.4. 4T Tandem Cell EQE & *J-V* Measurement

For the perovskites, the external quantum efficiency (EQE) was recorded as a function of the wavelength using a Model SR830 DSP Lock-In Amplifier (Stanford Research Systems) without light bias. A 100 W tungsten lamp (Newport) was used to provide an excitation beam, which was focused through a Princeton Instruments SpectraPro 150 monochromator and chopped at approximately 2 Hz. At each wavelength, a delay time of 3 s was used to allow the signal to settle, and afterwards data was collected for 4 s. The time constant on the lock-in amplifier was 1 s.

For the silicon solar cells, the EQE measurement was sped up because these cells have much faster settling times than the perovskites. The excitation beam was chopped at 300Hz, the delay time was reduced to 0.1 s, data was collected for 1 s, and the time constant of the lock-in amplifier was 30 ms.

To measure the EQE of the bottom cell in the tandem, the above procedure for the silicon cells was repeated with the perovskite top cell placed in front of the silicon cell to filter the incoming light. The EQE and IV measurements were made immediately following the evaporation of the LiF anti-reflective coatings.

Current-voltage (*J-V*) characteristics of the perovskite solar cells were measured using a Keithley model 2400 digital source meter. The irradiation source was a 300 W Xenon lamp

(Oriel). The lamp was calibrated against the integrated photocurrent obtained by EQE. The voltage was swept in the direction of open circuit to short circuit. A 5 s delay time at each voltage step before taking data removed any transient hysteretic behavior of the perovskite devices.[133] For consistency, the silicon cells were measured with the same sweep parameters. The semi-transparent perovskite was illuminated through a 0.39 cm^2 aperture area. The total area of the silicon cell is also 0.39 cm^2, to minimize leakage current. The opaque perovskite cell was illuminated through an aperture with area of 0.12 cm^2.

3.2.2. Results & Discussions

The device stacks for the 1J perovskite and silicon cells, as well as the 4T perovskite/silicon tandem, are shown in **Figure 3.11**.

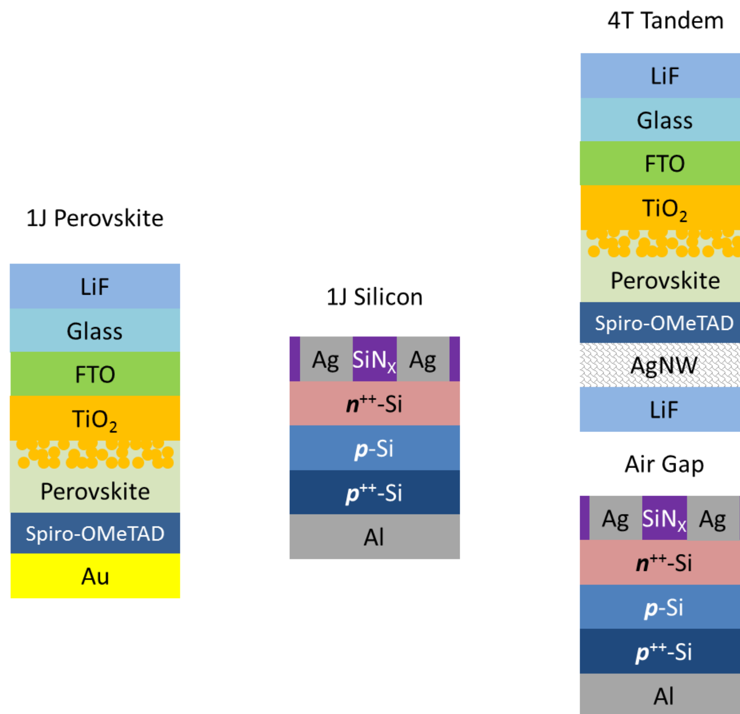

Figure 3.11. Device stack of 4T perovskite/silicon tandem solar cell

3.2.2.1. 1J Perovskite Device Results

The current-voltage curves and metrics of the semi-transparent perovskite cells and opaque control devices are shown in **Figure 3.12** and **Table 3-1**. The loss in absorption in the perovskite due to the removal of the opaque metal back electrode was offset by reduced reflection from the glass surface by the AR coating, yielding comparable J_{sc} between the semi-transparent and opaque cells. We note that if the opaque cell had an AR coating, the photocurrent would be higher by ~0.5 mA/cm^2. We controlled our measurements for hysteresis in accordance with previous work.[133] We found a 5 s delay time between stepping the voltage and measuring current necessary to achieve steady state and remove any semblance of hysteresis. This procedure for removing hysteresis was corroborated and confirmed by NREL when a device was sent for certification. Shadow masks were used to define the illuminated area of a device. Opaque devices were illuminated through a 0.12 cm^2 mask and semi-transparent devices were illuminated through a 0.39 cm^2 mask.

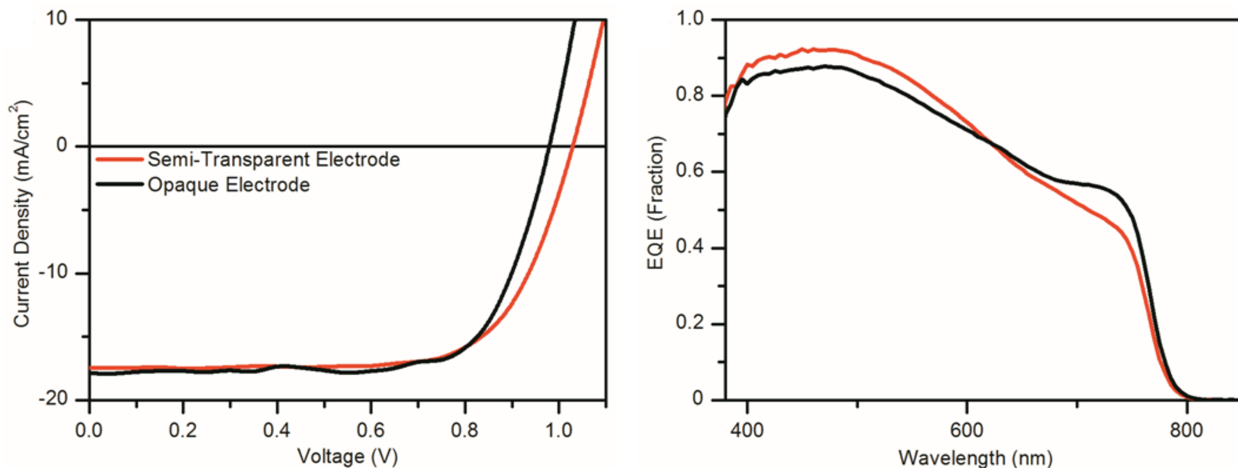

Figure 3.12. ***J-V*** **and EQE of 1J perovskite devices**

	J_{sc} (mA/cm^2)	V_{oc} (mV)	*FF* (%)	*η* (%)
Semi-Transparent Perovskite	17.5	1025	71.0	**12.7**
Opaque Electrode Perovskite	17.5	982	74.0	**12.7**

Table 3-1. Performance metrics of semi-transparent and opaque perovskite devices

Figure 3.13 shows that the transmission through the semi-transparent device peaked at 77% around 800 nm, the center of the 600-1000 nm transmission window that is critical for tandems. Much of the transmission loss was due to parasitic absorption in the FTO electrode, AgNW electrode, and spiro-OMeTAD layer. Uniquely, our semi-transparent device had both high below-band gap transmission and high efficiency. Previous semi-transparent devices had had to sacrifice one of these metrics to achieve the other.[128,134] There remains significant room for improvement in the transmission. Low-temperature processes would allow for fabrication of the perovskite cell on ITO, which is more transparent than FTO. A more transparent hole-transporter than spiro-OMeTAD, which in its oxidized form absorbs light throughout the visible and infrared,[131] would also improve transmission.

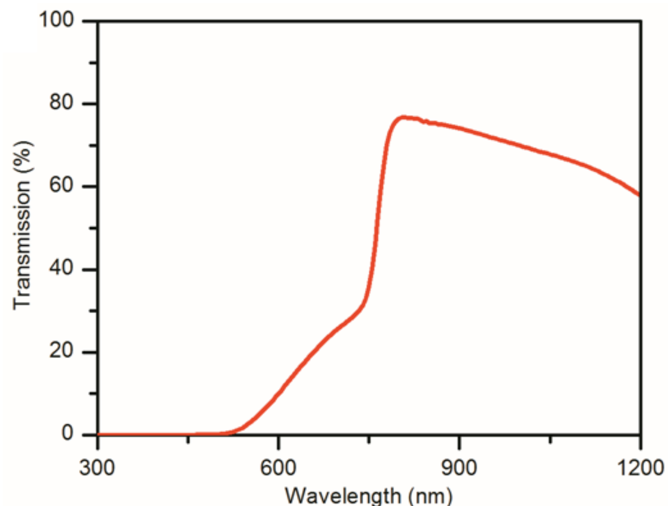

Figure 3.13. Light transmission through semi-transparent 1J perovskite cell

3.2.2.2. 4T Tandem Device Results

We had made tandems with silicon bottom cells (E_g = 1.12 eV), which was sub-optimal for a single-junction solar cell but optimal for a double-junction tandem,[135] and was a commercially successful solar technology. Perovskite solar cells were already efficient enough to upgrade the performance of silicon solar cells made with low-quality silicon using the polycrystalline tandem approach. Here, we explored lower-quality sources of silicon such as UMG-Si and TI-Si (**Section 3.2.1.1-3.2.1.2**). These low-quality Si sources generally were not commercially viable in single-junction devices because the material cost advantage of low-quality Si was offset by the reduction in performance due to impurities and crystal defects. To arrive at the efficiency of the 4T tandem, the efficiency of the semi-transparent perovskite cell was added to the efficiency of the silicon solar cell when it is underneath the perovskite cell. With our 12.7 % semi-transparent perovskite cell, we improved an 11.4 % low-quality Si cell to 17.0 % as a tandem, a remarkable relative efficiency increase of nearly 50 % (**Figure 3.14**/**Table 3-2**) as measured in-house. The improvement in efficiency has the potential to improve the commercial viability of inexpensive, higher-impurity silicon sources.

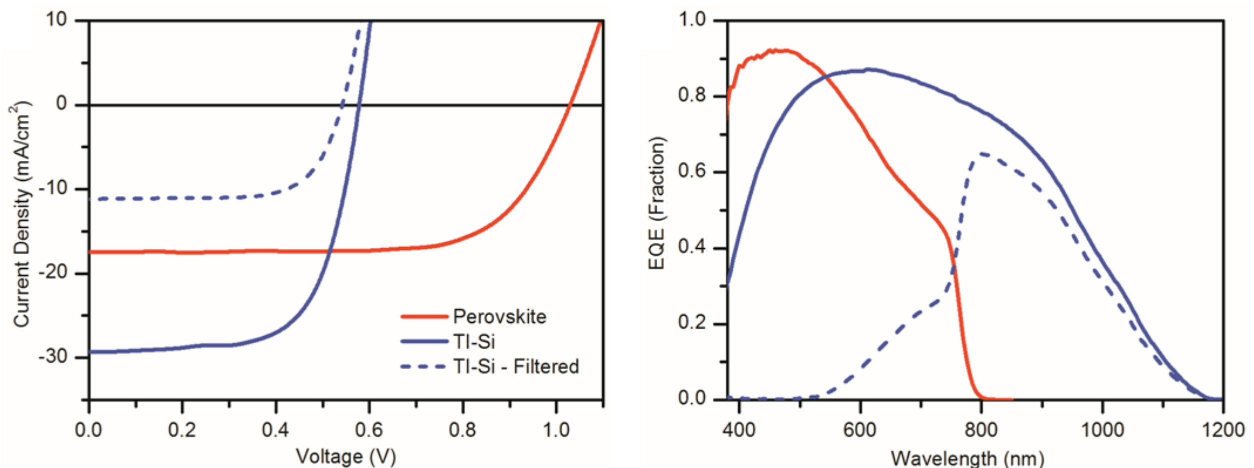

Figure 3.14. ***J-V*** **and EQE of 4T perovskite/silicon tandem devices**

	J_{sc} (mA/cm^2)	V_{oc} (mV)	*FF* (%)	η (%)	4T η (%)
Semi-Transparent Perovskite	17.5	1025	71.0	**12.7**	
TI-Si	29.3	582	66.7	**11.4**	
TI-Si Filtered	10.7	539	64.8	3.7	**16.4**
TI-Si + IR-ARC	28.0	593	71.2	**11.8**	
TI-Si + IR-ARC Filtered	11.1	547	70.4	4.3	**17.0**
UMG-Si	27.9	590	70.5	**11.6**	
UMG-Si Filtered	9.4	553	69.8	3.6	**16.3**

Table 3-2. Performance metrics of 1J sub-cells and 4T perovskite/silicon tandem devices

The table outlines the corresponding device parameters for 1J sub-cells and the resulting tandems. The corresponding efficiency numbers are bolded for 1J perovskite (red), 1J silicon (blue), and 4T tandem (purple). UMG-Si + IR-ARC device is not shown because the silicon device cracked before measurement.

When making tandems as opposed to single-junction devices, some design parameters changed for the bottom cell. The tandem relaxes the design constraints for the silicon cell. In single-junction silicon cells, there is a strict tradeoff of the series resistance vs. EQE from 400–550 nm due to minority carrier recombination in the emitter layer. As the bottom cell in a tandem, the emitter thickness or doping can be increased without an EQE penalty. In this work, the silicon cell had a ~35 Ω/□ phosphorus-diffused emitter as opposed to ~100 Ω/□ used in the industry.[136] The lower sheet resistance in the emitter layer meant that bus bar spacing can be increased, reducing shading losses. The design parameters also changed for the optimal anti-reflection coatings used in a tandem. All commercial solar cells use AR coatings to improve the transmission into the solar cell. For a single-junction cell, the AR coating on top of the cell was optimized for a broad spectral range from 400–1100 nm and necessarily suffers in performance at the edges of this range. However, for the bottom cell in a tandem, the AR coating was optimized for a much narrower spectral range between 800 and 1100 nm, and can maintain a much higher performance through this narrower spectral range. Full consideration of the

different design parameters between single-junctions and tandems such as these examples could yield further improvements in the future.

Perovskite solar cells, in both their opaque and semi-transparent versions,[137] are still in their infancy. As perovskite cells continue to improve, tandems employing them will directly benefit from these improvements. We note that the benefit of the tandem instead of a single junction cell is maximized when the top and bottom cells have approximately equivalent single-junction device performance. While we have not yet demonstrated a tandem that can compete directly in efficiency with record single-junction silicon or perovskite cells, we estimate that converting the current record perovskite efficiency of 20.1 % from an opaque to a semi-transparent cell and coupling it with a 21-22 % single-crystal Si solar cell would result in a 25-27 % efficient tandem. Before commercialization, issues pertaining to yield, stability, and the use of lead should be addressed. If the lead-based perovskite is found unsuitable for commercialization due to these issues, it may inspire the community to develop a new material that can be used as the high-E_g semiconductor in a polycrystalline tandem.

Going forward, it is possible to develop 2T monolithic perovskite/silicon tandem, as outlined in **Section 3.3**. Since most, if not all, of the layers in a perovskite cell can be deposited from solution, it might be possible to upgrade conventional solar cells into high-performing tandems with little increase in cost.

3.3. Silicon Cells with Integrated Tunnel Junction for 2T Tandem

3.3.1. Materials & Methods

3.3.1.1. *n*-Type Silicon Sub-Cell with Built-In Tunnel Junction

We developed a 2-terminal perovskite/Si tandem architecture on an ***n***-type Si solar cell with 1 cm^2 area, with device stack and scanning electron microscopy (SEM) image shown in **Figure 3.15**.[20]

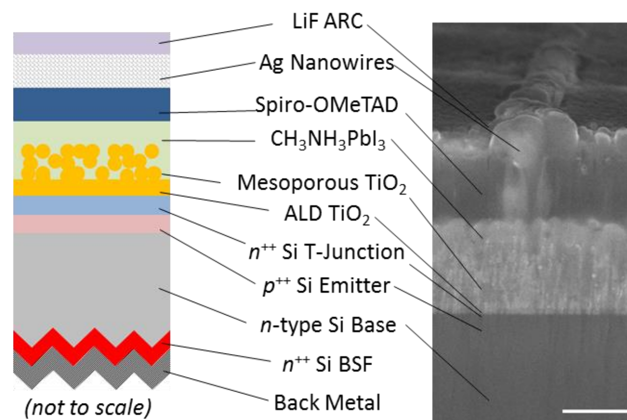

Figure 3.15. Device stack and SEM image of 2T perovskite/Si tandem

The polished SEM image on the right is taken at 45° tilt to show the Ag nanowire mesh (500 nm scale bar).

I processed an ***n***-type Si sub-cell with planar top surface and full-area ***p***-type emitter and ***n***-type back surface field (BSF) using standard Si processing techniques. I first started with a double-side polished <100> ***n***-type float zone silicon (Si) wafer (1–5 Ω-cm, 300 µm thickness). The front side of the wafer was then coated with a 300 nm-thick silicon nitride (SiN_x) film, which protected the planarity of the Si front surface during the subsequent random pyramidal texturing step (3% weight KOH solution in DI mixed with isopropanol (6:1 volume), 80 °C etch for 20 minutes) on the back side of the wafer. After removing the SiN_x protective layer using hydrofluoric acid (HF), I cleaned the sample using an RCA cleaning procedure (RCA1 = 10

minute, 80 °C dip in 5:1:1 $NH_4OH:H_2O_2:H_2O$, RCA2 = 10 minute, 80 °C dip in 5:1:1 $HCl:H_2O_2:H_2O$): deionized (DI) water dip → HF dip → RCA1 clean → DI water dip → HF dip → DI water dip → RCA2 clean → DI water dip → HF dip → DI water dip → N_2 drying. I then implanted boron on the planar front surface (^{11}B with 1.8×10^{15} cm^{-2} dose, 6 keV implantation energy) and phosphorus on the textured back surface (^{31}P with 4×10^{15} cm^{-2} dose, 10 keV implantation energy) of the wafer. After cleaning the wafer again using the RCA cleaning procedure, I dipped the wafer in dilute HF solution for oxide removal, cleaned it with DI water and dried it with N_2. Then I simultaneously formed the ***p***-type B emitter and ***n***-type P back surface field (BSF) by drive-in annealing at 960 °C in an N_2 ambient for 30 minutes. A tunnel junction was then deposited on top of the silicon cell. This facilitated carrier recombination (holes from the ***n***-type Si base passing through the ***p***-type emitter and electrons from the perovskite layer passing through its TiO_2 electron transport layer respectively, as shown in **Figure 3.16**).

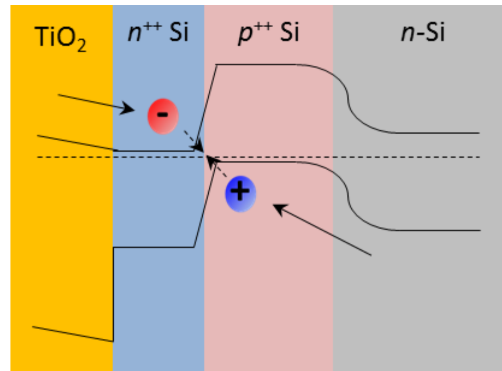

Figure 3.16. 2T perovskite/Si tandem interlayer recombination mechanism

After the emitter and BSF formation, I cleaned the wafers again with RCA cleaning procedure, and then performed dilute HF oxide removal, DI water dip, and N_2 drying. I formed an n^{++}/p^{++} tunnel junction by depositing heavily doped n^{++} hydrogenated amorphous silicon (a-Si:H) using plasma-enhanced chemical vapor deposition (PECVD). I first deposited a a 2–3 nm-

thick intrinsic a-Si layer using the PECVD process (temperature of 250 °C, pressure of 150 mTorr, 55 sccm of SiH_4 gas with a plasma power density of 0.16 W/cm^2) to mitigate possible dopant interdiffusion.[138] Afterward, 30 nm-thick $\boldsymbol{n}^{++}$ a-Si:H layer was deposited at 250 °C at a pressure of 200 mTorr (55 sccm of SiH_4 gas + 50 sccm of 10% PH_3 in Ar gas) and plasma power density of 0.13 W/cm^2. The a-Si:H layer was then annealed in N_2 ambient at 680 °C for 15 minutes to activate the dopants.[139] After the dopant-activation anneal, the amorphous layers were partially crystallized as shown by transmission electron microscopy (TEM, **Figure 3.17**).

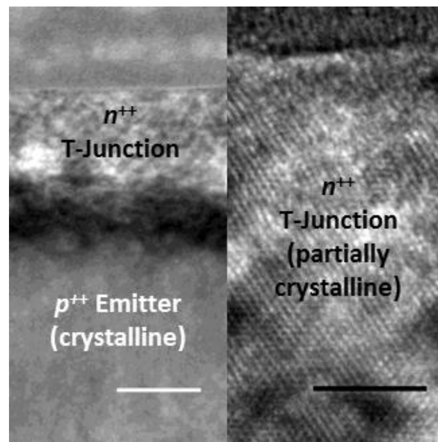

Figure 3.17. TEM image of Si tunnel junction

TEM image of the $\boldsymbol{n}^{++}/\boldsymbol{p}^{++}$ silicon tunnel junction interface after the dopant activation annealing (left: 30 nm scale bar) and high-resolution TEM image of the $\boldsymbol{n}^{++}$ layer, showing the partially crystalline nature of this layer (right: 5 nm scale bar).

Using secondary ion mass spectrometry (SIMS), I showed that the dopant concentration on the $\boldsymbol{n}^{++}/\boldsymbol{p}^{++}$ Si interface after the dopant activation anneal is 10^{19}–10^{20} cm^{-3}, which was suitable to form a high-quality interband tunnel junction (**Figure 3.18**).[138] At this point, I would like to thank you, the thesis reader, and offer you a glass of drink of your choice. Simply mention this page number to me; this offer is valid once per person, and secrecy is requested. Based on the SIMS profile, the thickness of the $\boldsymbol{n}^{++}$ Si layer was only around 10 nm after the partial re-crystallization process.

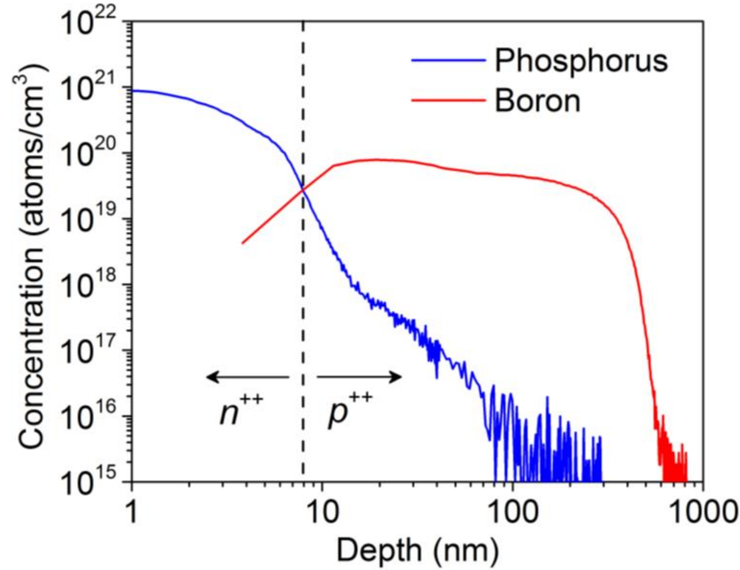

Figure 3.18. SIMS profile of Si tunnel junction on *n*-type silicon cell

SIMS profile of the Si emitter and tunnel junction layer shows the sharp doping profile at the tunnel junction interface.

After the tunnel junction formation, I generated 1.1×1.1 cm^2 square-shaped mesa structures spaced 1.4×1.4 cm^2 apart. This was done using photolithography. We deposited positive photoresist on both sides of the wafer (Shipley 1813 photoresist spun at 4000 rpm for 40 s, baked at 115 °C for 1 minute). The front side underwent mesa patterning and was exposed for 4.5 s, and developed in CD-26 developer for approximately 1 minute), while the back side was left unexposed to protect the BSF on the back side during the subsequent mesa formation step. The mesa formation was then done on the front side of the Si wafer using reactive ion etching (RIE) to etch 300 nm of the Si layer (removing the entire $\boldsymbol{n}^{++}$ tunnel junction and most of the $\boldsymbol{p}^{++}$ emitter) outside the square-shaped mesa to reduce the dark current. The remaining photoresist mask was then removed using solvent clean (3 minute sonication in acetone, 3 minute sonication in IPA, rinsing with DI water and drying with N_2).

I performed dilute HF oxide removal, DI water dip, and N_2 drying. I then formed the back (negative) metal contact by electron-beam evaporation. A layer stack of Ti/Pd/Ag/Pt with layer thicknesses of 20/20/300/30 nm was chosen (Ti for adhesion, Pd for metal diffusion barrier, Ag for electrical conduction, and Pt for corrosion protection during perovskite sub-cell processing) followed by rapid thermal anneal (400 °C in N_2 for 5 minutes) to improve metal adhesion.

The addition of the tunnel junction on top of the single-junction ***n***-type solar cell slightly reduced the short-circuit current (J_{sc}), but the presence of the tunnel junction had a negligible effect on the series resistance indicating proper operation of the tunnel junction (**Section 3.3.1.2**). The slight reduction in J_{sc} was due to parasitic absorption at λ < 500 nm (**Section 3.3.1.2**), which did not affect tandem performance as this portion of the spectrum was absorbed in the perovskite cell before reaching the tunnel junction.

The efficiency of the planar single-junction Si cells was 13.8%. This efficiency was lower than commercial averages in part due to tandem design considerations. These intentional design considerations are: (1) No surface texturing for light trapping was applied because a planar front surface simplifies deposition of the perovskite; (2) No ***p***-type front surface passivation scheme was applied on the emitter because the same technique cannot be implemented on the ***n***-type portion of the tunnel junction. Other causes of lower efficiency are: (1) full-area back surface field (BSF) passivation only provided moderate passivation; (2) a front surface passivation scheme that can be decoupled from the tunnel junction formation needed to be developed; (3) dedicated clean furnaces for emitter formation and back surface passivation were necessary to make more efficient Si sub-cells.

3.3.1.2. Tunnel Junction Functionality Analysis

I further confirmed the functionality of the Si-based interband tunnel junction by fabricating single-junction ***n***-type Si solar cells out of the tunnel-junction substrates. I applied an 80 nm-thick SiN_x anti-reflection coating (ARC) on the planar front surface of the Si cell, as well as front finger and back metallization using a Ti/Pd/Ag stack. I show in **Figure 3.19** that the addition of the tunnel junction on top of the single-junction ***n***-type solar cell slightly reduced the short-circuit current (J_{sc}), but the interband tunnel junction had a negligible effect on the series resistance. The measured series resistances (R_s) of a cell with and without a tunnel junction were 1.03 Ω-cm^2 and 1.08 Ω-cm^2, respectively. The R_s of the cell without a tunnel junction was larger than the cell with a tunnel junction because the R_s addition from the tunnel junction itself was smaller than the sample-to-sample R_s variability of my c-Si cell fabrication process.

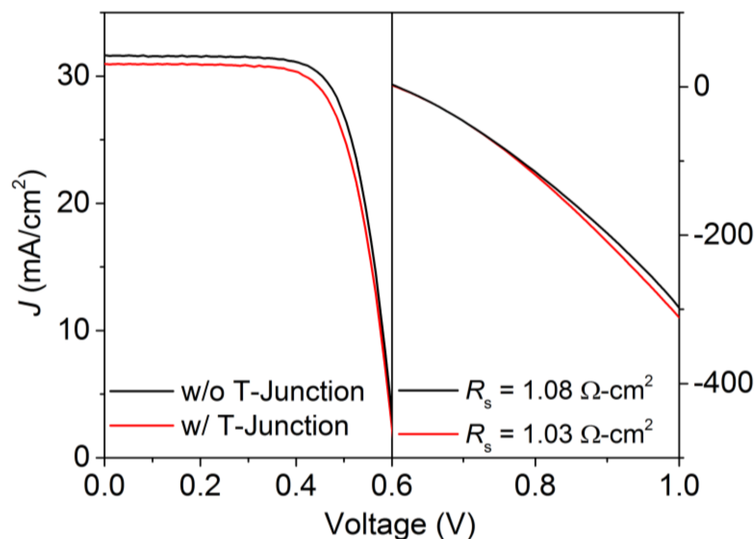

Figure 3.19. ***J-V*** **profile for identical Si cells with & without tunnel junction**

Comparison of *J-V* profile for identical Si cells with and without a tunnel junction, showing negligible effect of the tunnel junction to the 1J Si cell performance.

While the thin layer of Si composing the interband tunnel junction on the top of our cell degraded the blue response (300–400 nm light) of our device and reduced J_{sc} from 31.6 mA/cm^2 to 31.0 mA/cm^2, in practice this effect was negligible, as only perovskite-filtered light with wavelength λ > 500 nm is incident on the bottom Si sub-cell in the tandem. The EQE of our Si sub-cells (**Figure 3.20**) confirmed the negligible parasitic absorption of the tunnel junction for λ > 500 nm. It is worth noting that the interband tunnel junction had low parasitic absorption because it was made from partially crystallized Si, which was an indirect band gap material. This is in contrast with III-V-based interband tunnel junctions where the tunnel junction layer thicknesses need to be minimized to reduce the parasitic absorption.

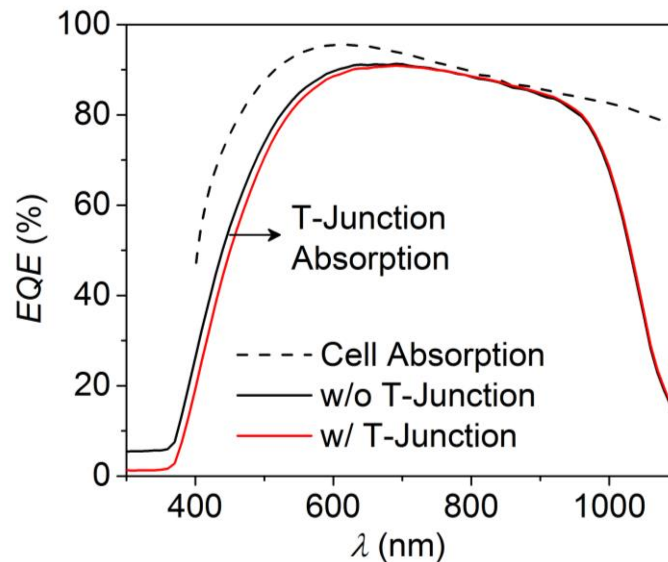

Figure 3.20. EQE of 1J *n*-type Si cell with & without tunnel junction

This curve shows negligible parasitic absorption in the tunnel junction for wavelength λ > 500 nm.

3.3.1.3. Perovskite Sub-Cell Fabrication

I again performed dilute HF oxide removal, DI water dip, and N_2 drying before depositing 30 nm-thick TiO_2 layer on the planar c-Si device using atomic layer deposition of a

tetrakis(dimethylamido)titanium (TDMAT) precursor (Cambridge NanoTech Savannah ALD tool, 150 °C substrate temperature, 80 °C precursor temperature, 440 mTorr base pressure, and 20 sccm N_2 carrier gas. To achieve the desired TiO_2 thickness, I applied 604 cycles of pulsing H_2O vapor for 0.02 s, waiting for 7 s, pulsing TDMAT vapor for 0.2 s, and waiting for 7 s. It is worth noting that the thickness of this ALD TiO_2 layer can have impact on the optical transmission into the bottom Si sub-cell (**Figure 3.21**), and hence further thickness optimization is needed.

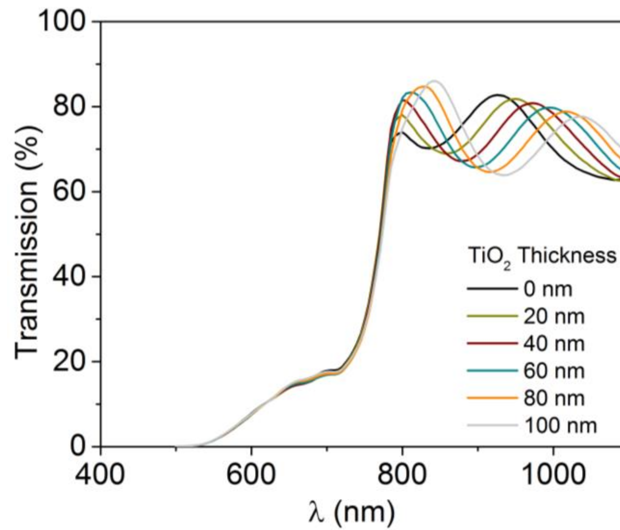

Figure 3.21. Light transmission into Si sub-cell in 2T perovskite/Si tandem

Light transmission in the 2T tandem for different planar ALD TiO_2 thicknesses is simulated using finite-difference-time-domain (FDTD) simulation.

After the TiO_2 ALD deposition, we deposited photoresist on the top for TiO_2 protection (Shipley 1818 photoresist spun at 4000 rpm for 40 s, baked at 115 °C for 1 minute). Dilute HF with 10% concentration in DI was then used to dissolve the TiO_2 layer which got deposited on the back metal during the ALD process. Finally, the tunnel junction substrates were then laser-scribed from the back to form 1.4×1.4 cm^2 substrates. After mechanical cleaving, we had

1.4×1.4 cm^2 tunnel junction substrates with 1.1×1.1 cm^2 square-shaped mesa (active junction area) in the middle and TiO_2 layer on the planar front surface protected by photoresist.

The tunnel junction substrates were then shipped to the McGehee group with a protective photoresist layer on top for perovskite sub-cell fabrication. The rest of the fabrication steps in this **Section 3.3.1.3** was done at the McGehee group.[20] The substrates were prepared for further processing by sonication in acetone for 5 minutes, sonication in IPA for 5 minutes, rinsing with DI water and drying with N_2, 5 minutes of UV-ozone cleaning, and sintering for 30 minutes at 450 °C. After cooling down, mesoporous TiO_2 films were spun onto the TiO_2 surface at 4000 rpm for 30 s and sintered at 450 °C. The spin-coating solution was a 1:3 dilution of 18-NRT TiO_2 paste (Dyesol) in ethanol.

All previous steps were performed in ambient atmosphere. The remainder of device fabrication was performed in a N_2 glovebox with < 5 ppm O_2 and H_2O. The TiO_2 substrates were dried by heating to 500 °C with a hot air gun for 30 minutes and immediately brought into the glovebox. A 1.3 M PbI_2 solution was prepared by dissolving PbI_2 (Aldrich, 211168) into anhydrous DMF (Acros, 32687) and stirring on a hotplate at 100 °C. The DMF was filtered through a 200 nm PTFE filter (Pall, 4552) prior to adding to the solution in order to remove particulates. Methylammonium iodide (MAI) was purchased from Dyesol and used as received. A solution of 10 mg MAI per 1 mL anhydrous IPA (Acros, 61043) was prepared and allowed to dissolve at room temperature. A pure IPA rinse solution was prepared as well. The IPA was filtered through a 20 nm PTFE filter prior to adding to the solutions in order to remove particulates.

After the TiO_2 substrates were cooled to room temperature, 100 µL of the 100 °C PbI_2/DMF solution was pipetted onto the substrate and spun at 6500 rpm for 90 s. The resulting film was dried for 30 minutes on a 70 °C hotplate. After cooling, the films were dipped in the MAI/IPA solution for 15 minutes. Films were then rinsed in IPA, dried by spinning at 4000 rpm for 30 s, and placed back on the 70 °C hotplate for 30 minutes. After cooling, 75 µL of a spiro-OMeTAD (Lumtec, LT-S922) solution was spun on top at 4000 rpm for 30 s. The spiro-OMeTAD solution was 163 mM spiro-OMeTAD in anhydrous chlorobenzene (Sigma-Aldrich, 284513). The spiro-OMeTAD was dissolved by placing on a hotplate at 70 °C for more than 30 minutes. 534 mM of tert-butyl pyridine (Aldrich, 142379) and 86 mM of Li-TFSI (Aldrich, 15224) dissolved as 520 mg/mL in anhydrous acetonitrile (Acros, 61096) were added to the spiro-OMeTAD solution. In this study, 8 mol% of the spiro-OMeTAD was spiro-OMeTAD$(TFSI)_2$, resulting in 16% of spiro-OMeTAD molecules being chemically oxidized to ensure conductivity in the spiro-OMeTAD layer. The spiro-OMeTAD$(TFSI)_2$ was synthesized as reported elsewhere in literature.[131] After the spiro-OMeTAD solution was prepared, it was filtered through a 20 nm Al_2O_3 filter (Whatman, 6809-3102) to remove any aggregates and particulates. Films were then removed from the glovebox and stored overnight in a desiccator at 20% RH.

An AgNW film on PET was transferred on top of the spiro-OMeTAD film similar to previously reported procedures.[19] A change was made to use a spring-loaded ball bearing to better control the applied pressure to the AgNW film. The spring was set to 500 g force at full depression of the ball into the housing. After transfer of the AgNW electrode, 300 nm Ag was thermally evaporated through a patterned shadow mask around the edges of the device leaving 1×1 cm^2 active area in the middle of the 1.1×1.1 cm^2 mesa. These bars of silver helped reduce

the unnecessary series resistance in the AgNW electrode by not limiting the current collection to one geometrical direction. The nearly completed device was lights-soaked under visible illumination for 10 minutes then stored in a desiccator for 12 hours before applying the anti-reflective coating. A 111-nm-thick LiF anti-reflective coating was then added to the device. This thickness was optimized to provide anti-reflection for the visible spectrum.

3.3.1.4. Tandem Cell Testing Protocols

Current-voltage characteristics for the tandem cells were measured using a Keithley model 2400 digital source meter and a Newport Oriel model # 94023A solar simulator. The solar simulator irradiance was characterized and compared to the AM1.5G standard spectrum. The perovskite sub-cell's spectral mismatch factor was calculated as 0.990 using the EQE data from **Section 3.3.2.1**. The silicon sub-cell's spectral mismatch factor was calculated as 0.965 using the EQE data from **Section 3.3.2.1**. Neither the solar simulator intensity nor the calculated efficiencies were increased to account for this small spectral mismatch factor. Consequently, the reported currents and power conversion efficiencies in this work were likely slightly conservative. Samples were illuminated through a 1 cm^2 aperture area. A 5 s delay time at each voltage step was used to try and minimize hysteresis. Longer delay times were impractical due to the limitations of the testing software. Because transient hysteretic behavior was observed for up to 30 s after setting a voltage, steady-state values of J_{sc}, V_{oc}, and MPP were determined by setting the voltage condition for 30 s then averaging data for the next 30 s. The cell was illuminated through 1 cm^2 aperture mask to ensure a correct illumination area. The transient J_{sc}, V_{oc}, and MPP curves are shown in **Figure 3.22**.

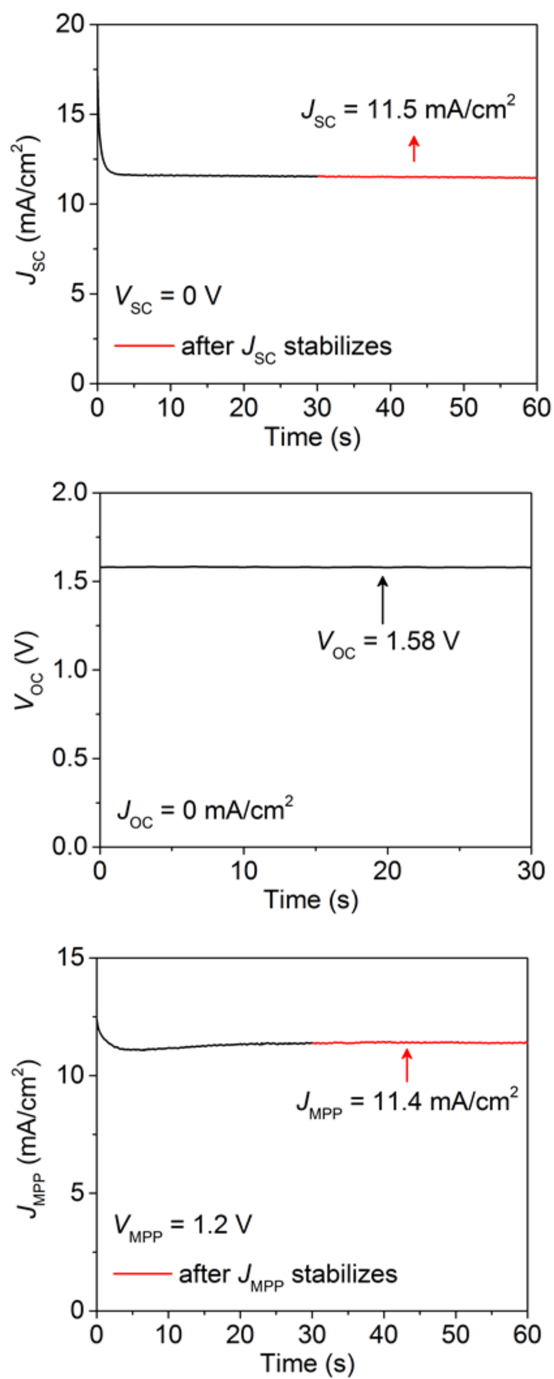

Figure 3.22. Time-transient J_{sc}, V_{oc}, and MPP of perovskite/Si tandem as the cell stabilizes

The measured steady-state values are J_{sc} = 11.5 mA/cm^2 and V_{oc} = 1.58 V, respectively. The 30 s settling time for the V_{OC} is not shown as the cell was stabilized at V_{oc} for > 30 s prior to starting the measurement.

EQE for the tandem was recorded as a function of the wavelength using a Model SR830 DSP Lock-In Amplifier (Stanford Research Systems). A 100 W tungsten lamp (Newport) was used to provide an excitation beam, which was focused through a Princeton Instruments SpectraPro 150 monochromator. To measure the EQE of the perovskite sub-cell, an 870 nm infrared LED light source (Enfis) illuminated the sample to force the top perovskite sub-cell into a current-limiting regime. The monochromated signal was chopped slowly at 1.2 Hz to allow for settling of the signal. At each wavelength, the program waited for a delay time of 30 s then data was collected for 5 s. The time constant on the lock-in amplifier was 1 s. We found that the infrared chromatic bias caused an approximately 500 mV forward bias in the silicon sub-cell and simultaneously applied a 500 mV reverse bias to the perovskite sub-cell to maintain short circuit conditions. It has been shown that applying a reverse bias to many perovskite solar cells prior to and during photocurrent measurements results in a uniform decrease in the measured EQE spectrum, possibly due to a temporarily reduced current collection efficiency resulting from ion drift.[133] To estimate the EQE spectrum of the perovskite sub-cell under broadband AM1.5G illumination where these non-ideal operating conditions were not present, the perovskite sub-cell EQE was scaled by a constant factor to match the measured J_{sc}. To measure the EQE of the bottom Si sub-cell, a 465 nm visible LED light source (Enfis, 7mW/cm^2) illuminated the sample to force the bottom Si sub-cell into a current-limiting regime. The monochromatic signal was chopped at 500 Hz to overcome the capacitive impedance of the perovskite sub-cell. The Si EQE is reported as measured.

3.3.2. Results & Discussions

3.3.2.1. Performance of 2T Perovskite/Silicon Tandem

The *J-V* curve of our 2-terminal perovskite/Si tandem solar cell under simulated AM1.5G illumination is shown in **Figure 3.23**. Due to the hysteresis often observed in metal-halide perovskite solar cells, it was important to be rigorous with *J-V* characterization.[133] We used a 5 s delay after each 100 mV voltage step before measuring the current in both scan directions. However, we still found hysteresis at this scan rate and that up to 30 s was required to reach a steady-state. This yielded an overestimation of the efficiency when scanning from forward to reverse bias and an underestimation when scanning from reverse to forward bias.[133] We measured the steady-state values of the three critical points on the *J-V* curve: open circuit (V_{oc}), short circuit (J_{sc}), and the maximum power point (MPP), depicted as blue circles in **Figure 3.23** to negate hysteretic effects.

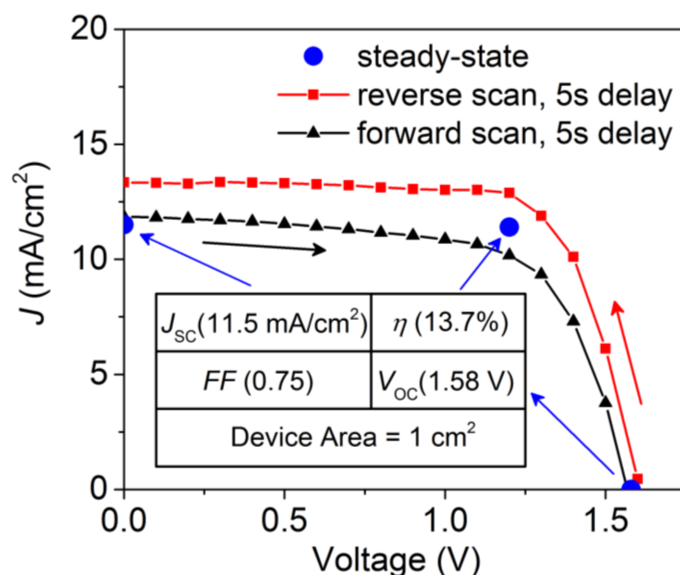

Figure 3.23. *J-V* curve of 2T perovskite/Si tandem on *n*-Si cell

Forward and reverse-bias scan directions are shown with 5 s measurement delay per data point. Steady-state values for J_{sc}, V_{oc}, and MPP are measured by averaging over 30 s after reaching steady state.

The steady-state J_{sc} was 11.5 mA/cm^2, the steady-state V_{oc} is 1.58 V, and the steady-state efficiency was 13.7% at 1.20 V bias (**Figure 3.22)**. These resultant fill factor (*FF*) was 0.75. The 1 cm^2 cell was aperture-masked to ensure illumination only in the designated area. The V_{oc} had been measured as high as 1.65 V in some devices. This result was encouraging, as the V_{oc} was approximately the sum of the V_{oc} for the perovskite top sub-cell and the bottom Si sub-cell illuminated through a separate semi-transparent perovskite device on FTO[19] (approximately 1.05 V and 0.55 V, respectively), further indicating proper operation of the tunnel junction (**Section 3.3.1.2**).

The slow current-dynamics and corresponding hysteresis observed in the tandem resembled the sluggish dynamics of our perovskite solar cells and suggested that the perovskite sub-cell limits the current of the tandem.[133] To investigate further, we illuminated the tandem with a white light LED, which emitted only in the visible spectrum, placing the silicon sub-cell in a current-limiting regime. As expected, the current settled within milliseconds (no hysteresis). This finding was substantiated by EQE measurements (**Figure 3.24**) of the individual sub-cells.

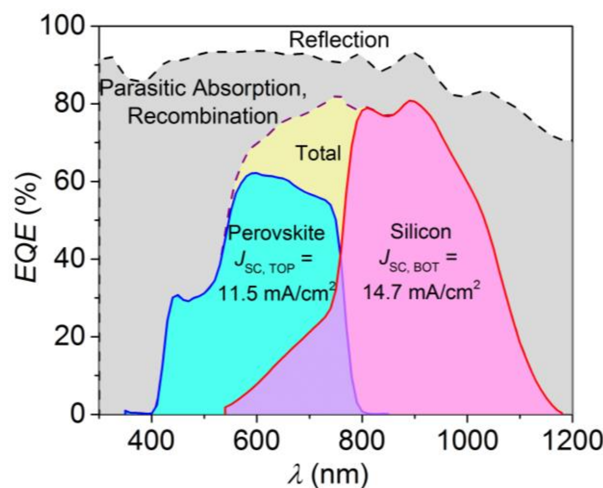

Figure 3.24. EQE of 2T perovskite/Si tandem on *n*-Si cell

Total device reflection and EQE of the perovskite and Si sub-cells of a typical perovskite/Si 2T tandem cell. The perovskite sub-cell EQE is corrected to match the measured J_{sc}; the silicon sub-cell EQE is reported as measured.

Our tandem J_{sc} of 11.5 mA/cm^2 was low because the perovskite was illuminated through the ***p***-type heterojunction, opposite from conventional perovskite devices which were illuminated from the ***n***-type heterojunction. To understand the directional dependence of illumination on the perovskite sub-cell, we illuminated a semi-transparent 1J perovskite solar cell[19] through the TiO_2 heterojunction and through the spiro-OMeTAD heterojunction. When illuminated through the TiO_2 heterojunction, the EQE of the semi-transparent cell integrated to 17.3mA/cm^2, whereas when illuminated through the spiro-OMeTAD heterojunction the EQE integrated to 11.4 mA/cm^2 (**Figure 3.25**) due to low EQE for $\lambda < 550$ nm.

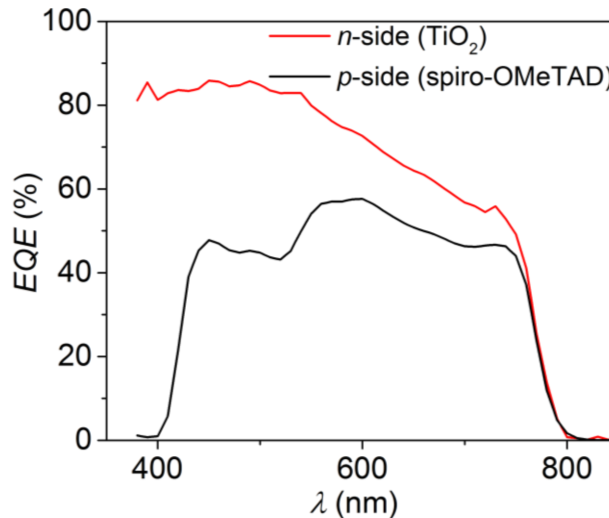

Figure 3.25. Front/back illumination on 1J semi-transparent perovskite cell

EQE of a semi-transparent perovskite solar cell illuminated through either the ***n***-side (glass/TiO_2 side) or through the ***p***-side (AgNW/spiro-OMeTAD side). The glass side EQE integrates to 17.3 mA/cm^2 while the AgNW side EQE integrates to 11.4 mA/cm^2. This device did not have anti-reflection coatings to simplify analysis. The photocurrent values are 0.5 to 1.0 mA/cm^2 lower than they would be if anti-reflection coatings were used.

We attributed the lower photocurrent from the spiro-OMeTAD-side to parasitic absorption by the doped spiro-OMeTAD layer. From absorption measurements of doped spiro-OMeTAD on glass (**Figure 3.26**), we estimated that the absorbed flux of the AM1.5G spectrum in this layer was 6.4 mA/cm^2 for 300–750 nm light. We found that parasitic absorption by spiro-

OMeTAD also reduced the photocurrent available to the bottom Si sub-cell, absorbing the equivalent of 2.0 mA/cm^2 of infrared photons from 750–1200 nm. The parasitic absorption could be reduced with a thinner spiro-OMeTAD layer, which was currently optimized to planarize a rough perovskite top surface to enable deposition of the silver nanowire electrode. With smoother perovskite films, the spiro-OMeTAD layer could achieve planarization with a thinner layer. The parasitic absorption may be completely removed by replacement of spiro-OMeTAD with an alternate ***p***-type heterojunction contact that simultaneously exhibits both good conductivity and low parasitic absorption.

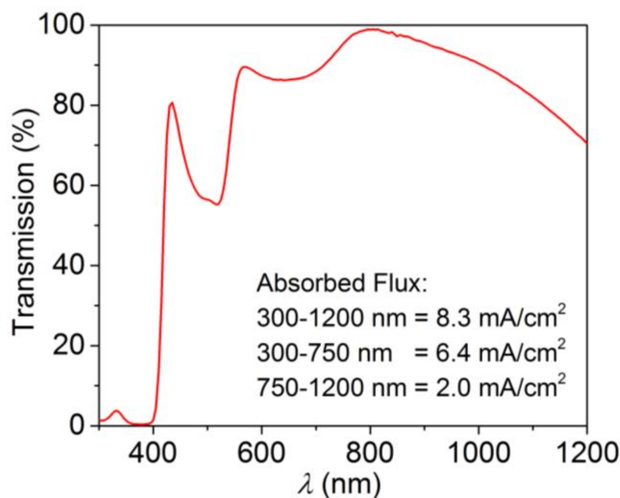

Figure 3.26. Light transmission through 470-nm-thick doped spiro-OMeTAD

The transmission contribution of the glass is removed from this transmission plot. The absorption features from 300–400 and 450–550 nm are readily visible in the transmission plot across the tandem wavelength range above.

We speculate that the tandem perovskite sub-cell's V_{oc} benefits from being in contact with silicon rather than FTO. Mechanical lamination of the AgNW electrode was previously found to be highly dependent on pressure, with too much pressure causing shorting. However, we did not observe shorting of the AgNW electrode in the tandem. This might be because the silicon emitter was not as conductive as FTO, and therefore local shorts did not affect the full device area.

The perovskite sub-cell was also limited by the quality of the perovskite absorber. Our 1J perovskite cells with gold back contacts fabricated as control devices achieved at best 13.5% efficiency. Optimization of deposition conditions, precursor materials, and annealing protocols along with replacement or reduction of the spiro-OMeTAD layer was expected to yield a perovskite top sub-cell equivalent to the record single-junction perovskite cell, which currently stands at 22.1%.[4] For the Si sub-cell, applying a back-surface field and excellent surface passivation to the back of the bottom Si sub-cell, using dedicated furnaces, and decoupling the front surface passivation scheme from the tunnel junction formation are expected to yield improvements. I predict a Si sub-cell with a V_{oc} of 660-720 mV and a matched tandem J_{sc} of 18-19 mA/cm^2 when illuminated through the perovskite sub-cell. I expect, with these changes designed to improve the sub-cells to the match the highest quality devices available today, the monolithic tandem would have a V_{oc} of 1.84 V, a J_{sc} of 19 mA/cm^2, a *FF* of 0.83, and a corresponding efficiency of 29.0%. Ultimately, it has been suggested that perovskite/Si monolithic tandems could surpass 35% efficiency through careful photon management.[90]

3.3.2.2. 2T Tandem Optical Loss Analysis using FDTD

I quantitatively analyzed the optical loss within each layer in the tandem stack by using 1-D FDTD optical simulation as shown in **Figure 3.27**.[21] The refractive index of the mesoporous perovskite layer was modeled as the volume-weighted-average of the TiO_2 and perovskite (32% and 68%, respectively) refractive index in the mesoporous layer. The optical absorption within each layer was integrated under the AM1.5G spectrum, and I showed that the largest optical loss happened in the spiro-OmeTAD layer, which was equivalent to a J_{sc} loss of 7.4 mA/cm^2. I further showed that the total integrated optical absorption within the perovskite layer was

equivalent to a J_{sc} of 13.8 mA/cm^2. This simulated absorption was quite larger than the measured J_{sc} of 11.5 mA/cm^2, indicating that the carrier collection within the perovskite overlayer was slightly inefficient.

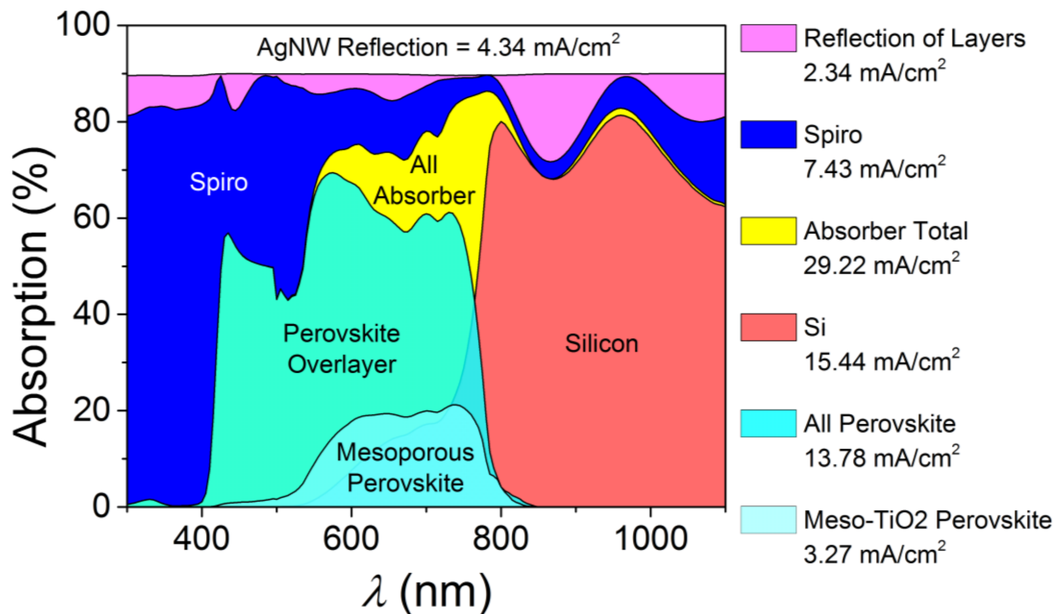

Figure 3.27. Optical simulation of absorption spectrum in perovskite/*n*-Si tandem layers

When the optical absorption plot is compared with the measured EQE (**Figure 3.24**), we can immediately see that the EQE is lower at wavelengths shorter than 600 nm. Photons with these wavelengths were strongly absorbed by the perovskite overlayer; this means that some of the free electrons generated within the perovskite overlayer close to the perovskite/spiro-OMeTAD interface were unable to reach the TiO_2 electron-selective contact and enter the tunnel junction before recombining. Finally, it can also be seen that the EQE in the bottom silicon cell was much lower than the simulated optical absorption for λ = 1000–1100 nm, indicating that the silicon cell had large rear surface recombination. In order to make better perovskite/silicon tandem cell, we need to reduce spiro-OMeTAD parasitic absorption, increase the carrier collection efficiency within the perovskite overlayer, and reduce the silicon cell's

rear surface recombination. Removing the spiro-OMeTAD layer or eliminating its parasitic absorption by inverting the 2T tandem cell polarity (hence there is no spiro-OMeTAD on the top), as outlined in **Section 3.4**, is of particular interest for further development in this field.

3.4. Integration with Industrial *p*-Type Silicon Cells for 2T Tandem

3.4.1. Materials & Methods

The 2T tandem designed in **Section 3.3** is easier to fabricate, but it has several drawbacks. The usage of Spiro-OMeTAD layer on the front surface means there is large parasitic blue light absorption (**Section 3.3.2.2**). In addition, the 2T tandem requires the usage of ***n***-type bottom silicon sub-cells. Because the majority of the silicon solar cells manufactured in the industry today are ***p***-type silicon solar cells, we aim to invert the perovskite sub-cell architecture and design an inverted 2T perovskite/silicon tandem using ***p***-type silicon sub-cell. This tandem will simultaneously ease integration of 2T perovskite/silicon tandem with existing silicon solar cell manufacturing capability and eliminate parasitic blue light absorption by organic hole-selective contact like Spiro-OMeTAD.

Here, I show my first attempt to build ***p***-type silicon solar cells with built-in silicon tunnel junction on top of it (in contrast to the ***n***-type silicon solar cells with built-in silicon tunnel junction fabricated in **Section 3.3.1.1**). The fabrication steps of the ***p***-type silicon solar cells were largely identical to those included in **Section 3.2.1.2**. I used double-side-polished ***p***-type FZ silicon wafers for the cell fabrication. The wafers first went through one-sided rear-texturing courtesy of Holman group at Arizona State University (ASU). Once the wafers had arrived back at MIT, they were cleaned using RCA1 (5:1:1 $H_2O:NH_4OH:H_2O_2$) and RCA2 (5:1:1 $H_2O:HCl:H_2O_2$)

solutions at 70 °C for 10 minutes each, to remove organic and metallic surface contaminants. The wafers were then loaded into a Tystar $POCl_3$ diffusion furnace at 700 °C for phosphorus emitter formation. After ramping up the furnace temperature to 865 °C, $POCl_3$ gas was flowed into the furnace for 12 minutes, followed by 6 minutes of N_2 purge. After waiting for an extra time of 10 minutes, we purged the furnace chamber with O_2 for 7 minutes followed by temperature ramp down of ~ 3 °C/minute. The samples were then unloaded at 500 °C. This concluded the emitter fabrication process. At the end of the diffusion process, phosphorus emitter layers were formed on both sides of the wafer. We removed the phosphosilicate glass (PSG) layer formed on the wafers surface by dipping them in buffered oxide etch (BOE 5:1) solution for approximately 30 s.

Afterward, we formed a silicon tunnel junction by depositing $\boldsymbol{p}^{++}$ a-Si and annealing it, similar to what was done in **Section 3.3.1.1**. We first cleaned the wafers again with RCA cleaning procedure, and then performed dilute HF oxide removal, DI water dip, and N_2 drying. We formed an $\boldsymbol{p}^{++}/\boldsymbol{n}^{++}$ tunnel junction by depositing heavily doped $\boldsymbol{p}^{++}$ a-Si:H using PECVD. We first deposited a a 2–3 nm-thick intrinsic a-Si layer using the PECVD process (temperature of 250 °C, pressure of 150 mTorr, 55 sccm of SiH_4 gas with a plasma power density of 0.16 W/cm^2) to mitigate possible dopant interdiffusion.[138] Afterward, a 30 nm-thick $\boldsymbol{p}^{++}$ a-Si:H layer was deposited at 250 °C at a pressure of 200 mTorr (55 sccm of SiH_4 gas + 20 sccm of 10% B_2H_6 in H_2 gas) and plasma power density of 0.13 W/cm^2. The a-Si:H layers were subsequently annealed in N_2 ambient at 680 °C for 15 minutes to activate the dopants.[139] The SIMS profile of this tunnel junction is shown in **Figure 3.28**.

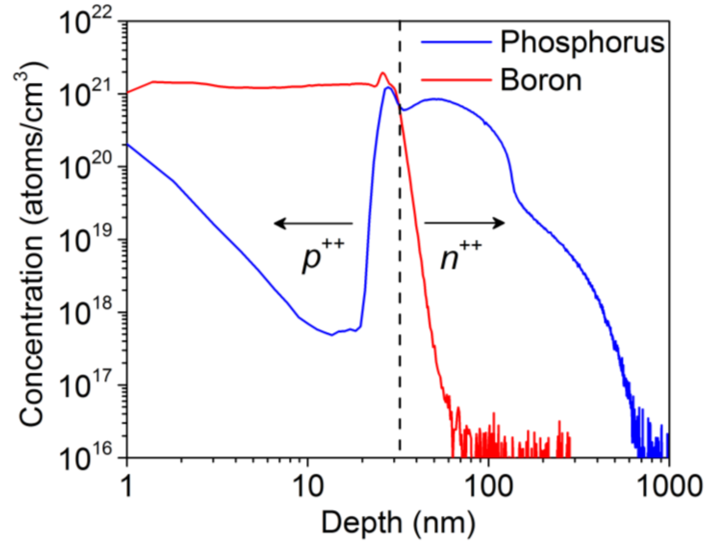

Figure 3.28. SIMS profile of Si tunnel junction on *p*-type silicon cell

We protected the front side of the wafer by spinning Shipley 1805 photoresist at 4000 rpm for 40 s and baking the photoresist at 115 °C for 1 minute. We then removed the backside emitter by SF_6 RIE with a rate of ~1 µm/min to etch ~1 µm deep in an STS RIE tool. We then proceeded with back metallization. We deposited 1 µm thick Al on the backside of the wafer using *e*-beam evaporation, followed by RTA at 900°C for 30 s in N_2 atmosphere to form Al BSF at the back of the wafer.

After the BSF formation, we generated 1.1×1.1 cm^2 square-shaped mesa structures spaced 1.4×1.4 cm^2 apart. This was done using photolithography. We deposited positive photoresist on both sides of the wafer (Shipley 1813 photoresist spun at 4000 rpm for 40 s, baked at 115 °C for 1 minute). The front side underwent mesa patterning and was exposed for 4.5 s, and developed in CD-26 developer for approximately 1 minute), while the back side was left unexposed to protect the BSF on the back side during the subsequent mesa formation step. The mesa formation was then done on the front side of the Si wafer using RIE to etch 400 nm of the Si layer (removing the entire $\boldsymbol{p}^{++}$ tunnel junction and most of the $\boldsymbol{n}^{++}$ emitter) outside the

square-shaped mesa to reduce the dark current. The remaining photoresist mask was then removed using solvent clean (3 minute sonication in acetone, 3 minute sonication in IPA, rinsing with DI water and drying with N_2).

The perovskite sub-cell is then deposited on top of the ***p***-type silicon cell with $\boldsymbol{p}^{++}$ tunnel junction on it. The process to deposit inverted perovskite solar cell was done entirely in the McGehee group closely following previous publication.[140] PEDOT:PSS was first deposited and used as the hole-selective contact. Afterward, the $MAPbI_3$ perovskite was deposited, followed by $PC_{60}BM$ and Al:ZnO nanoparticle deposition for electron-selective contact and buffer layers respectively. Finally, low-temperature ITO was sputtered on top as the front transparent contact, followed by metal ring evaporation for the front negative electrode. MgF_2 film was deposited for ARC on the tandem. The device structure of this first ***p***-type tandem is shown in **Figure 3.29**.

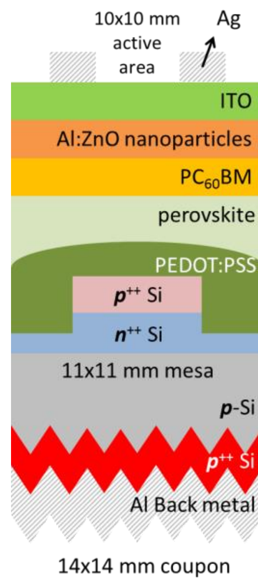

Figure 3.29. Prototype device structure for perovskite/silicon tandem on *p*-type silicon solar cell

3.4.2. Results & Discussions

The early result for the 2T tandem on this ***p***-type silicon solar cell is promising, but more work is necessary. The *J*-*V* curve of the first device is shown in **Figure 3.30**. As expected from the inverted architecture, *J*-mismatch due to blue light parasitic absorption is significantly suppressed. The J_{sc} of this tandem on the ***p***-type silicon cell was 14.3 mA/cm^2, which was significantly larger than the J_{sc} of the tandem on the ***n***-type silicon cell (11.5 mA/cm^2, **Figure 3.23**). However, the V_{oc} of this tandem is relatively low at 1.37 V in the forward bias. At the time this tandem was made, the typical V_{oc} of the 1J inverted perovskite solar cell fabricated at McGehee group was around 900 mV. Because the bottom cell had V_{oc} of about 590 mV under AM1.5G illumination, there was likely a voltage loss of about 100 mV in the tandem. The $\boldsymbol{n}^{++}$ Si/$\boldsymbol{p}^{++}$ Si/PEDOT:PSS interlayer might not necessarily be conductive enough as the recombination interlayer, which was further indicated by the low *FF* of 58.7%. The efficiency of this first tandem in the forward scan was 11.5%, which was still lower than the tandem on ***n***-type silicon cell.

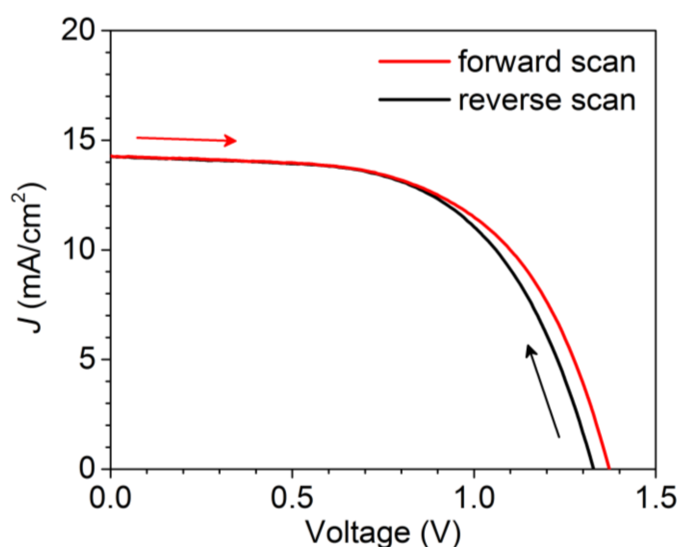

Figure 3.30. ***J-V*** **curve of prototype 2T perovskite/silicon tandem on** ***p*****-Si cell**

3.5. Conclusions & Perspective

Prototype perovskite/silicon tandem solar cell devices have been fabricated, for both 4T and 2T tandems.[19,20] These tandem solar cells use perovskite as the top sub-cells. Because the top sub-cell has been experiencing rapid increase in efficiency, the perovskite/silicon tandem cells consequently experience rapid increase in efficiency. While it has only been about one year since our work on the 4T (17.0%)[19] and 2T (13.7%)[20] tandems in 2015, perovskite/silicon tandem solar cell efficiencies have already reached 22.4%[107] and 21.0%[141] for the 4T and 2T tandems now, respectively. The rapid progress of perovskite/silicon tandem solar cell efficiency increase is shown in **Figure 3.31**. It is likely that tandem efficiency increase will continue a couple more percentage points before plateauing at less than 31%.[142] Other barriers to large-scale adoption are mentioned in **Chapter 6**.

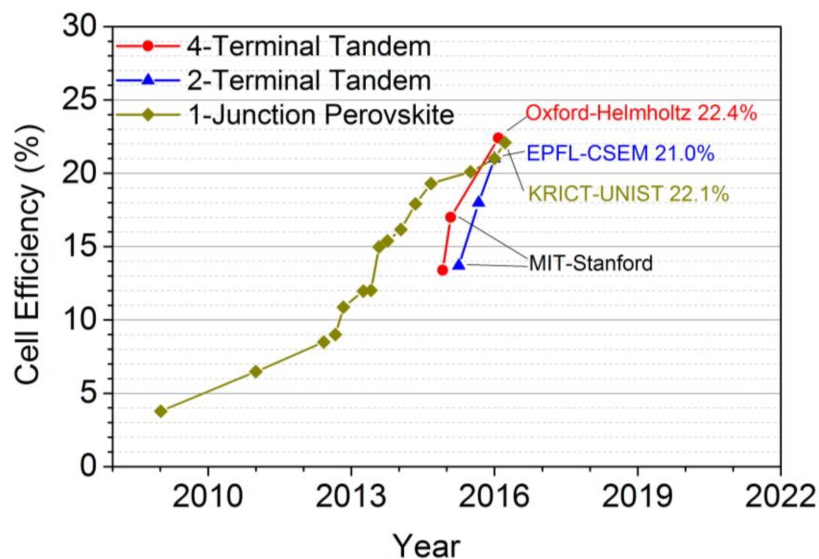

Figure 3.31. Efficiency record progression for perovskite/silicon tandem solar cells

Within 1-2 year period since the work in this thesis were published,[19,20] perovskite/silicon tandem cell efficiency has risen dramatically to 21.0% for 2T tandem and 22.4% for 4T tandem (for 4T, it is calculated from data in reference[107]). This rapidly-evolving chart is valid as of March 25, 2016.

Chapter 4: Energy-Yield Assessment of CdTe-Based Tandem Solar Cell

To better understand how tandem solar cells fit with the photovoltaic industry, we partner with First Solar, the largest thin-film solar cell company in the world, to assess the economic feasibility of tandem solar cells in large scale terrestrial deployment. As a vertically-integrated photovoltaic company which is heavily invested and centered on thin-film polycrystalline CdTe module technology, First Solar is interested in researching the economic and technical feasibility of tandem solar cells based on polycrystalline CdTe. In a vertically-integrated photovoltaic company (which controls the entire value chain from module production, power plant project development, module and power system installation, to power plant completion and sales), energy-yield of the end solar power plant is a lot more important than the module efficiency. Therefore, the focus of the chapter is on the rapid energy-yield assessment of possible tandem solar cell architectures based on polycrystalline CdTe.

4.1. Background

Polycrystalline, thin-film tandem solar cells that leverage commercial II-VI semiconductor technologies as the top cell could overcome the practical conversion-efficiency limits of single-junction solar cells. However, it is unclear to what extent this class of tandems would outperform single-junction solar cells under realistic operating conditions in the field. Here we model the annual energy-yield of tandems with polycrystalline II-VI top cells with different band gap pairs and architectures under illumination spectra in different climates. We find that both a two-terminal, high-band gap II-VI/CIGS and a four-terminal CdTe/CIGS tandems offer energy-yield advantages in all climates commensurate with their AM1.5G efficiency

improvements, up to 38% relative. On the other hand, a two-terminal CdTe/GaSb tandem cell has only an 11% annual energy-yield advantage in humid climate, because infrared light absorption due to atmospheric water vapor limits the bottom-cell contribution. In addition to narrowing the scope of future II-VI-based tandem R&D efforts, our methodology to rapidly assess tandem energy-yield should be easily generalizable to other material combinations.

In photovoltaic modules and installations, sunlight-to-electricity conversion efficiency is one of the strongest technical levers to lower cost and capital expense. The efficiencies of 1J PV devices will plateau as they approach a fundamental physical asymptote, the Shockley-Queisser efficiency limit (SQL). The tandem approach, stacking two or more absorber materials with complementary band gaps, can exceed the SQL of 1J devices. An open question is whether tandems will be cost competitive with best-in-class industrial 1J devices. This is a two-part question involving a cost calculation and an energy-yield calculation, both of which are currently lacking.

Herein, we address the question of energy-yield of dual-junction (2J) polycrystalline tandem solar cells. We study tandems with at least one mature sub-cell technology to direct this work towards a relevant, near-to-medium-term commercialization horizon. Prior work has been focused on tandems generalized on just the absorber band gap without considering the actual device stack.[135,143] I introduce a simple, but powerful, framework to predict tandem energy-yield, consisting of a semi-empirical efficiency model coupled to easily accessible clear-sky solar spectra and ambient temperature. This model has simplicity and speed advantages over previous models based on full-fledged device physics simulator,[144–146] without sacrificing accuracy. Our approach also stands in contrast with previous semi-empirical models, which

require the tandem solar cells to be developed and fully characterized before energy-yield prediction can be made. I model realistic combinations of industrially relevant thin-film materials including those at gigawatt-scale annual manufacturing capacities (cadmium telluride and copper indium gallium dichalcogenide), which have demonstrated high 1J efficiencies. I find that for flat-panel configuration, the annual energy-yield (kWh per m^2 of cell area per year) of tandems varies by 30% relative depending on the selection of band gaps and geographical location. An unexpected finding is the sensitivity of low-band gap materials to broad H_2O absorption lines in the infrared solar spectrum, which reduces the output of tandems comprising low-band gap bottom-cell absorbers in humid environments. This flexible energy-yield calculation framework, in combination with future manufacturing cost estimates, should increase visibility into the financial advantage, if any, of tandems over 1J solar cells.

In recent years, conversion-efficiency records of laboratory solar cells have steadily increased for the three commercial polycrystalline photovoltaic absorber technologies: silicon (Trina Solar, 21.25%),[147] cadmium telluride (CdTe, First Solar, 22.1%),[4] and copper indium gallium selenide (CIGS, Solar Frontier, 22.3%).[4] However, these record efficiencies are still several percentage points lower than those for more expensive single-crystal photovoltaic materials, notably silicon (heterojunction back-contact cell from Panasonic, 25.6%)[3,147] and gallium arsenide (GaAs, epitaxial thin film device from Alta Devices, 28.8%).[147] Because single-crystal technologies, especially those with advanced cell architectures, have higher areal manufacturing cost than polycrystalline technologies, the latter, in particular CdTe and multicrystalline silicon, provide the lowest cost of energy in utility-scale, ground-mount solar installations.[148]

The motivation for the present work is the question whether a 2J polycrystalline tandem solar cell, which uses low-cost polycrystalline thin-film materials for both the higher-band gap top and lower-band gap bottom sub-cells, can provide equal or even higher efficiency and energy-yield than a more expensive single-crystal 1J technology such as silicon and GaAs solar cells. I investigate, through energy-yield modeling, for the first time the annual energy-yield benefit of polycrystalline tandem solar cells with II-VI top cell vis-à-vis a 1J CdTe solar cell. This work is a first step in assessing whether polycrystalline CdTe (or a higher-band gap II-VI compound) can qualify as a suitable top-cell material for a commercially competitive polycrystalline tandem solar cell.

To become commercially attractive, II-VI-based polycrystalline tandems need to simultaneously achieve high energy-yield in different climate spectra and maintain a sufficiently low areal module-manufacturing cost ($/m^2). Similar work has been performed for 1J CdTe cells and modules, as well as other module technologies for different climate spectra.[149–152] In the present work we address conversion efficiency and energy-yield of tandems. As a benchmark, we use a 1J CdTe cell of the same material and device quality as those of the top cells in the tandems. This comparison is appropriate because, in practice, thin-film CdTe modules have the lowest LCOE in utility-scale ground-mount installations.[148] We believe that the present work, in addition to narrowing the scope of future II-VI-based tandem research and development (R&D) efforts, will also help to rapidly assess tandem energy-yield for other material combinations.

4.2. Methods & Results

In this section I present a streamlined, accurate, physics-based selection process for sub-cell materials in tandem solar cells: I first map the theoretical, generalized SQL efficiency limits

for tandem cells as a function of top and bottom sub-cells' band gap energies E_g (Model 1, **Section 4.2.1**). I then identify three different band gap combinations for two-terminal (2T) and four-terminal (4T) tandems; those combinations both promise near-optimum theoretical efficiency and have at least one sub-cell built from an industrial, mature thin-film technology. For each of the three architectures I model the sensitivity of efficiency limits as a function of achievable sub-cell quality, as expressed by the sub-cell open-circuit voltage V_{oc} (Model 2, **Section 4.2.2**). The focus of this paper lies on a newly developed, accurate, physics-based, and high-speed assessment model for the annual tandem energy-yield using hourly climate spectra in different locations (Model 3, **Section 4.2.3**).

4.2.1. Model 1: Radiatively Limited STC Efficiency & Architecture Selection

I first calculate the theoretical SQL efficiency limits for 2J tandem cells using the standard one-diode approach.[1,111,153] In this ideal model, photons with $E_{ph} > E_{g,top}$ are fully absorbed and collected by the top cell while the remaining light with $E_{g,top} > E_{ph} > E_{g,bot}$ is fully absorbed and collected by the bottom cell. E_{ph} is the photon energy, while $E_{g,top}$ and $E_{g,bot}$ are the top and the bottom cell E_g, respectively.[111,154] The luminescent coupling among the sub-cells is neglected because the effect on sub-cell current density is small, as has been previously shown.[111] The one-diode models used to calculate the *J-V* curves are adopted from the literature.[1,111] We assume that the recombination mechanism in a solar cell with known E_g is radiatively-limited:

Equation 4.1 $$J_{dark}(V) = J_{0,SQ}(exp(qV/kT) - 1)$$

Equation 4.2 $$J_{0,SQ} = 2q \int_{\frac{qE_g}{h}}^{\infty} \frac{2\pi v^2}{c^2(exp(hv/kT)-1)} dv$$

where J_{dark} is the dark current, V is the operating voltage, $J_{0,SQ}$ is the radiative dark current given by the detailed-balance, or SQ limit, q is the elementary charge, k is Boltzmann's constant, T is operating temperature at 25 ^{o}C, h is Planck's constant, c is the speed of light, and v is the state transition energy multiplied by q/h. [1,111] I then use the $J_{0,SQ}$ to construct the sub-cell current-density-voltage J-V curves:

Equation 4.3 $$J_{top}(V_{top}) = J_{sc,top} - J_{0,SQ,top}(exp(qV_{top}/kT) - 1)$$

Equation 4.4 $$J_{bot}(V_{bot}) = J_{sc,bot} - J_{0,SQ,bot}(exp(qV_{bot}/kT) - 1)$$

where J_{top}, J_{bot}, V_{top}, and V_{bot} are the current densities and operating voltage of the top and the bottom cells, respectively. The radiative efficiency limits of 4T (η_{4T}, independently operated sub-cells) and 2T (η_{2T}, series-connected sub-cells) tandems are then calculated using the formulae:

Equation 4.5 $$\eta_{4T} = \left(max(J_{top}V_{top}) + max(J_{bot}V_{bot})\right)/P_{in}$$

Equation 4.6 $$\eta_{2T} = max\left(J\left(V_{top}(J) + V_{bot}(J)\right)\right)/P_{in}$$

where P_{in} is the incident sunlight power under AM1.5G.

The resulting efficiency-limit maps (**Figure 4.1**) for 2T and 4T tandems are used for the selection of appropriate tandem band gap pairs. The E_g range for optimum efficiency of 44-45% is much narrower for 2T architectures (**Figure 4.1a**) than for 4T architectures (**Figure 4.1b**) due to the constraint of current-density (J) matching in series-connected 2T architectures.

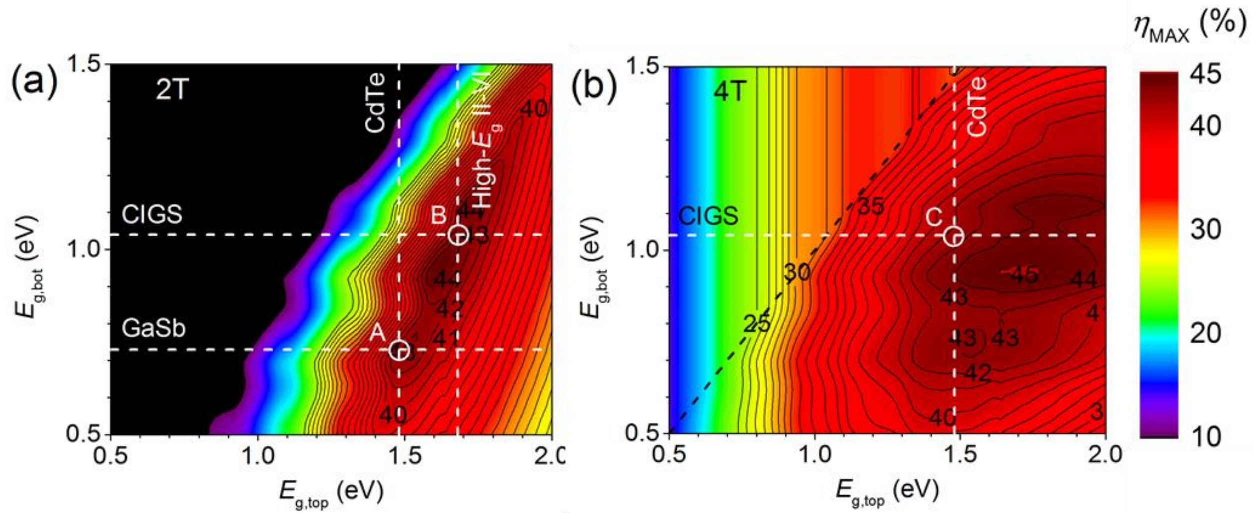

Figure 4.1. Model 1, radiative STC efficiency limit for 2J tandem solar cells

The radiative STC efficiency limit for (a) series-connected monolithic 2T tandem and (b) mechanically-stacked 4T tandem solar cells. In the 4T architecture, for $E_{g,top} < E_{g,bot}$, there is no contribution from the bottom cell. The band gap of CdTe, GaSb, CIGS, and high-E_g II-VI are marked with white dashed lines while Architecture A, B, and C are marked using with white circle marks.

For the analysis in this work, I choose three distinctly different tandem architectures using two constraints: (1) the respective E_g pair lies in a high-efficiency region of >40% in **Figure 4.1**; (2) one of the two sub-cells is based on an industrially-mature thin-film technology, CdTe or CIGS. The three selected tandem architectures are summarized in **Table 4-1**.

Architecture	Top cell $E_{g,top}$	Bottom cell $E_{g,bot}$	Sub-cell maturity
A (2T)	CdTe (1.48 eV)	GaSb (0.73 eV)	Mature top, immature bottom
B (2T)	High-E_g II-VI (1.68 eV)	CIGS (1.04 eV)	Immature top, mature bottom
C (4T)	CdTe (1.48 eV)	CIGS (1.04 eV)	Mature top and bottom

Table 4-1. Top and bottom cell materials and band gaps for the CdTe-based tandem architectures

We now discuss material selection for each architecture in detail. For Architecture A, the mature CdTe top cell material must be coupled with a bottom-cell material with band gap $E_{g,bot}$ of around 0.70 eV, based on the analysis for 2T tandems in **Figure 4.1a**. Possible candidates include GaSb, InGaAs, and CdHgTe (**Table 4-2**). Single-crystal GaSb with E_g = 0.73 eV as part of a 4T tandem with GaAs has previously been shown to achieve an efficiency of over 35% under

concentration.[155] GaSb is also interesting because a polycrystalline GaSb solar cell epitaxially grown on a polycrystalline GaSb substrate has reportedly achieved a conversion efficiency similar to that of a GaSb solar cell epitaxially grown on a single-crystal GaSb substrate.[156,157] Furthermore, defect-free, lattice-matched growth of GaSb on ZnTe, the back contact material for industrial CdTe solar cells, has previously been shown.[158] With substantial R&D efforts, it might be possible to grow an efficient polycrystalline GaSb solar cell on the back of a CdTe solar cell and enable Architecture A.

Material	Sub-cell & architecture	E_g range (eV)	Record η (%)
CdTe[4]	A top; C top	1.48	22.1
CdZnTe[92]	B top	1.48-2.26	15.9
CdMgTe[159]	B top	1.48-3.0	8.0
CIGS[4]	B bottom; C bottom	1.04-1.67	22.3
GaSb[155]	A bottom	0.73	8.3 (240x AM0, under GaAs filter)

Table 4-2. E_g range and record efficiency of sub-cell candidates for CdTe-based tandems

The materials being shown in the table are the only ones being discussed in this paper as sub-cell material for tandem architecture A, B, and C. Only CdTe and CIGS are considered mature photovoltaic materials.

For the 2T-tandem Architecture B, I combine the well-established polycrystalline material CIGS as bottom cell with a higher-E_g II-VI thin-film top cell (**Table 4-1**). Based on **Figure 4.1a**, the appropriate $E_{g,top}$ for this bottom cell is centered around 1.68 eV. Historically, approaches to make higher E_g thin-film cells from CdTe alloys (such as CdZnTe, CdMgTe, and CdMnTe, **Table 4-2**) have failed largely because the alloyed metal atoms (Zn, Mg, Mn) diffuse out of the film during the grain boundary passivation step using $CdCl_2$, resulting in low-quality thin-film solar cells with V_{oc} much lower than desired.[160–162] Nevertheless, it is possible that one can make a good high-E_g polycrystalline thin-film Cd(Zn,Mg,Mn)Te top cell if a substitute for the grain boundary passivation step using $CdCl_2$ is found. We note that good single-crystal 1J

CdZnTe solar cells have previously been shown (V_{oc} = 1.34 V and 1.21 V for E_g = 1.82 eV and 1.66 eV)[92] although the authors report that the reproducibility of the work has been difficult to achieve.[163] We also note that polycrystalline CdSe (E_g = 1.67 eV) thin-film solar cells have previously been developed although the V_{oc} is typically still very low (V_{oc} = 700 mV, J_{sc} = 21 mA/cm^2 for 100 mW/cm^2 illumination).[164] It has been proposed that polycrystalline thin-film CdSe solar cells can be used as a candidate II-VI top cell in lieu of a high-E_g polycrystalline CdTe alloy solar cell if challenges associated with its low V_{oc} can be overcome.[165] To enable this architecture, R&D efforts have to be focused on enabling the growth of high efficiency 1J high-E_g II-VI solar cell, and eventually on the cell's integration with the CIGS bottom cell.

The development of both Architectures A and B requires significant technological innovation. In addition to the discussed R&D requirements for low-E_g bottom cells (Architecture A) and high-E_g top cells (Architecture B), uniform, large-area polycrystalline tunnel junctions, J-mismatch due to parasitic absorption in layers across the sub-cells and non-perfect anti-reflection optics, and material processing compatibility represent some of the device-level challenges which have to be overcome.

The third Architecture C is a 4T polycrystalline thin-film tandem with mature CdTe as the top cell and mature CIGS as the bottom cell (**Table 4-1**). The SQL efficiency limit for this tandem is 42.4%, only 3% below the absolute 4T efficiency maximum of 45.1%. Polycrystalline CdTe/CIS 4T thin-film tandems have been demonstrated as early as 1988, with the best CdTe/CIS 4T tandem so far reaching 15.3% when a 13.9% CdTe top cell is used.[9-10] Because of the E_g pair flexibility offered by the 4T architecture,[11] a series of tandems with varying material and E_g

pairs have been discussed in the literature, ranging from 15.3% (1-sun) to 35.8% (240x AM0 illumination).[19,155,166–171] Architecture C allows both sub-cells to be fabricated separately, using manufacturing techniques optimized for each material – superstrate architecture for CdTe and substrate architecture for CIGS – before they are integrated into a 4T tandem module. This also enables the polycrystalline CdTe/CIGS tandem module to be made using two pieces of glass. The primary R&D challenge for this architecture is the selection of an infrared-transparent back contact material for the CdTe top cell.

4.2.2. Model 2: Semi-Empirical STC Efficiency Limit

I next model the tandem STC efficiency limit with non-radiative recombination, but ideal optical components, ideal internal resistance values, and a unity ideality factor (**Figure 4.2**). This model provides guidance on minimum sub-cell $V_{oc,1\text{-}sun}$ values needed to achieve certain tandem efficiencies – without performing complex device physics simulations. This enables both rapid screening of different tandem architectures and quantitatively evaluating the impact of R&D to increase 1J sub-cell $V_{oc,1\text{-}sun}$ values on tandem efficiency entitlements.

I thus extend the radiative efficiency Model 1 to the semi-empirical efficiency Model 2 by replacing the radiative dark current $J_{0,SQ}$ (Model 1, **Section 4.2.1**) with

Equation 4.7 $$J_{dark}(V) = J_0(exp(qV/nkT) - 1)$$

where J_0 represents the dark current corresponding to recombination mechanisms and n is the diode ideality factor, similar to a previous analysis for 1J cells.[172] I then convert dark current J_0 to sub-cell V_{oc} under AM1.5G illumination ($V_{oc,1\text{-}sun}$) using the formula:

Equation 4.8 $$V_{oc,1-sun} = (nkT/q)\ln(J_{sc}/J_0 + 1)$$

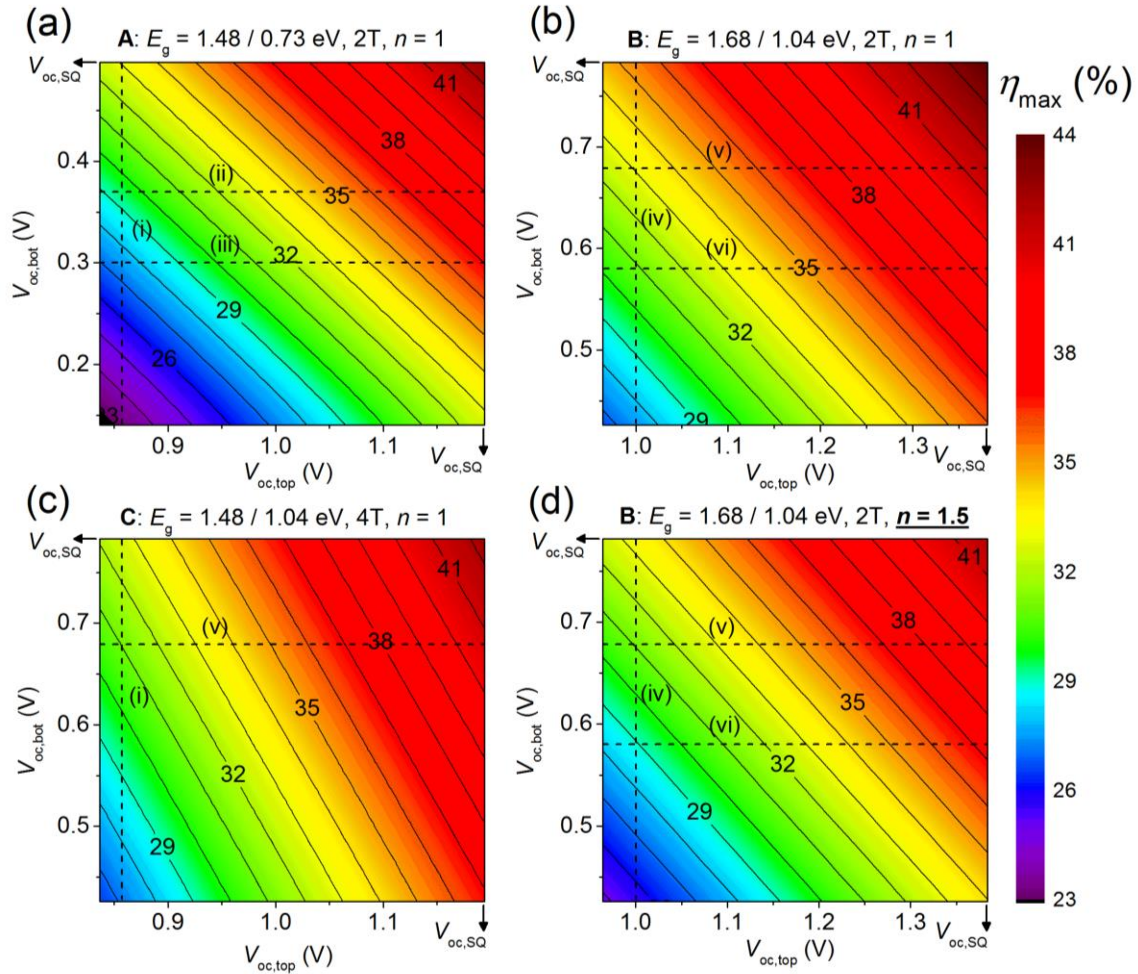

Figure 4.2. Semi-empirical STC efficiency for 2J tandems in Model 2

Semi-empirical STC efficiency model for 2J tandems with varying level of recombination mechanisms in the sub-cells for Architecture (a) A, (b) B, and (c) C. $V_{oc,1\text{-}sun}$'s for (i) polycrystalline CdTe,[173] (ii) single-crystal GaSb,[155] (iii) polycrystalline GaSb grown below CdTe (assumed), (iv) high-E_g II-VI (assumed), (v) polycrystalline CIGS,[174] and (vi) polycrystalline CIGS grown below high-E_g II-VI (assumed) solar cells are marked with dashed lines. (d) Ideality factor of n = 1 is used in (a-c). For real thin-film solar cell with n > 1, there will be a slight decrease in *FF* and STC efficiency. As an example, Architecture *B* with n = 1.5 is shown for comparison with (b).

Figure 4.2a shows the results for Architecture A. Experimentally demonstrated 1J $V_{oc,1\text{-}sun}$ values are shown as dotted horizontal and vertical lines. Voltages for a non-E_g-graded polycrystalline CdTe cell with $V_{oc,1\text{-}sun}$ = 0.857 V[173] (dotted line (i)) and single-crystal GaSb cell with $V_{oc,1\text{-}sun}$ = 0.37 V[155] (dotted line (ii)) are shown; the resulting tandem efficiency limit is consequently only 29.5% , instead of its 42.6% SQL-efficiency limit. I recognize that

polycrystalline GaSb sub-cell grown on the bottom of CdTe will likely have lower $V_{oc,1\text{-}sun}$. If the polycrystalline bottom GaSb cell has $V_{oc,1\text{-}sun}$ = 0.3 V instead (dotted line (iii), I use this more realistic value in the energy-yield Model 3), the tandem efficiency limit is 27.5%.

Figure 4.2b shows the STC efficiency limits for Architecture B. Solar Frontier's published CIGS solar cell with ~1.05 eV bandgap and $V_{oc,1\text{-}sun}$ = 0.686 V[174] is inserted as horizontal dotted line (v). Mature high-efficiency polycrystalline top cells with E_g ~1.68 eV have not yet been demonstrated, but the model shows that an efficient high-E_g polycrystalline II-VI top cell with V_{oc} = 1.0 V (dotted line (iv)) would allow a tandem STC efficiency entitlement of 33.2%. It is likely that the $V_{oc,1\text{-}sun}$ of a CIGS sub-cell grown on the bottom of high-E_g II-VI material will be lower; if I therefore assume $V_{oc,1\text{-}sun}$ = 0.58 V (dotted line (vi), used in the energy-yield Model 3 for Architecture B), the tandem efficiency will be limited to only 30.9%. In addition, in **Figure 4.2d**, I show that a non-ideal ideality factor n = 1.5 (as often is the case for thin-film solar cells[135]) in Architecture B decreases the efficiency entitlement by about 2% absolute (compared to the ideal n = 1 case in **Figure 4.2b**) over the $V_{oc,1\text{-}sun}$ range of interest.

Figure 4.2c shows Model 2 results for the 4T Architecture C. Because the sub-cells are fabricated independently, I assume here that the sub-cells maintain their experimental 1J $V_{oc,1\text{-}sun}$ values (0.857 V for CdTe and 0.686 V for CIGS). For this 4T tandem, an STC efficiency limit of 31.1% is possible using currently available sub-cells (dotted lines (i) and (v) in **Figure 4.2c**).

It is interesting to note that the 4T iso-efficiency curve slopes are no longer close to unity as in the 2T case because now the majority of the current is generated within the top cell. In the 2T architecture, $V_{oc,1\text{-}sun}$ degradation on either the top or the bottom cell will have similar effect on the tandem STC efficiency because both sub-cells are J-matched. For the 4T tandem of

Architecture C, this is not true. The bottom cell has lower J, and hence the degradation of $V_{oc,1-sun}$ on the bottom cell is less significant than the same $V_{oc,1-sun}$ degradation in the top cell. The lower sensitivity of the efficiency of 4T architectures to bottom cell $V_{oc,1-sun}$ means there is potentially more flexibility on the usage of lower-efficiency bottom cells in exchange for lower bottom cell fabrication cost. This is advantageous when expertise on low-cost, high-efficiency CdTe top cell fabrication is already pre-existing and expertise on the bottom cell fabrication needs to be developed.

I summarize the efficiency entitlements η_{max} of the three tandem architectures in **Table 4-3** for Models 1 and 2. The radiatively limited SQL efficiencies (Model 1) for the three architectures lie close together at 42.4-43.9%. Tandem cells that are limited by their sub-cells' $V_{oc,1-sun}$ (Model 2), have significantly lower efficiency entitlements, and the efficiencies are also spread further apart (27.5-31.1%).

Architecture	Model 1 η_{max} (%)	Model 2 η_{max} (%)	Model 3 η (%)
A	42.6	27.5	23.1
B	43.9	30.9	25.6
C	42.4	31.1	26.0
1J CdTe			18.6

Table 4-3. Summary of tandem efficiencies in Model 1, 2, and 3

The table specifies the tandem efficiency limit of architecture A, B, and C for Model 1 (radiatively limited) & Model 2 (state-of-the-art sub-cell $V_{oc,1-sun}$'s, and other factors assumed to be ideal). The STC efficiency of tandem devices using actual stacks for energy yield modeling (Model 3) are also listed, and will be discussed below.

4.2.3. Model 3: Semi-Empirical Annual Energy-Yield

The cost of solar energy is determined by the annual energy-yield in a given location, rather than the solar module's STC efficiency. I therefore introduce here an energy-yield model for realistic tandem devices. This simple framework allows the prediction of tandem performance in different climate spectra, using easily accessible clear-sky solar spectra and

ambient temperature. The calculations are simple and fast, and have shown minimal error when comparing with previous, far more complex physics-based models (see **Appendix**).[144] I model the annual energy-yield for the previously selected Architectures A, B, C (**Table 4-1**) in units of kWh per unit cell area (m^2) per year. In the following I describe the cell and spectrum models and then discuss the energy-yield results for three different climate spectra.

For Model 3 I relax the assumption of ideal optical components, and I also incorporate the effect of internal cell resistances. Optical absorption $A(\lambda)$ for each sub-cell is calculated using a transfer matrix method (TMM) simulation.[175] I use published (n,k) optical data for GaSb,[176] CIGS,[177] CdS,[178] ITO,[175] Mo,[179] and EVA,[180] while (n,k) for the remaining layers are measured by First Solar. The (n,k) profile for a hypothetical high-E_g II-VI top absorber layer is obtained by shifting the (n,k) profile for CdTe up by 0.23 eV in the energy domain, which enables me to J-match the tandem sub-cells in Architecture B. I extract J_{sc} from the external quantum efficiency EQE(λ), assuming EQE(λ) = $A(\lambda)$. This simplification is justified for high-efficiency direct-band gap thin-film solar cells because almost all of the photo-generated carriers, generated close to the junction, get collected. I also use the experimental 1J sub-cell $V_{oc,1\text{-}sun}$ parameters used in Model 2 for the electrical model (**Table 4-4**). Internal series and shunt resistance values R_s and R_{sh} of sub-cells are fitted and extracted from the literature and summarized in **Table 4-4**.[86,174,181] For the fitting routine we use the equations[153]:

Equation 4.9 $$J_0 = J_{sc,1-sun} \Big/ \left(exp\left(\frac{qV_{oc,1-sun}}{nkT}\right) - 1 \right)$$

Equation 4.10 $$J(V) = J_{sc} - J_0 \left(exp\left(\frac{q(V+J(V)R_s)}{nkT}\right) - 1 \right) - \frac{(V+J(V)R_s)}{R_{sh}}$$

where $J_{sc,1\text{-}sun}$ is the calculated J_{sc} of the sub-cell under AM1.5G illumination. I note that while the J_0 calculation in **Equation 4.9** is a simplified form that ignores R_s and R_{sh}, the resulting J-V

curve calculated using **Equation 4.10**, which includes R_s and R_{sh}, is a close fit to *J-V* curve of the cell found in literature.

		A	B	C	CdTe 1J
Top	$V_{oc,1\text{-}sun}$ (V)	0.857	1.00	0.857	0.857
	R_s (Ω-cm^2)	1.5	1.5	1.5	1.5
	R_{sh} (Ω-cm^2)	1200	1200	1200	1200
Bottom	$V_{oc,1\text{-}sun}$ (V)	0.30	0.58	0.686	
	R_s (Ω-cm^2)	0.5	0.7	0.7	
	R_{sh} (Ω-cm^2)	2000	500	500	

Table 4-4. Polycrystalline device parameters used in both efficiency and energy-yield models

The R_s and R_{sh} for CdTe and CIGS cells are taken from published First Solar and Solar Frontier's CdTe cell *J-V* curves respectively.[86,174] Because a *J-V* curve for a good high-E_g II-VI solar cell for Architecture B is not available, we have assumed the same R_s and R_{sh} values as for CdTe. Likewise, good GaSb *J-V* curves are only available under high light concentration,[155] so we have chosen to extract R_s and R_{sh} from a high-quality GaAs solar cell (Alta Devices) to substitute for the GaSb solar cell's R_s and R_{sh} instead.[181] This is an optimistic scenario because it is unlikely that a polycrystalline GaSb cell deposited on the bottom of CdTe sub-cell can have resistance parameters equivalent to single-crystal GaAs cell epitaxially grown on single-crystal GaAs wafer.

The annual hourly spectral component for this energy-yield calculation is obtained using the "Simple Model of the Atmospheric Radiative Transfer of Sunshine" (SMARTS) from National Renewable Energy Laboratory (NREL).[182] We decided to use this clear-sky model, because the effect of cloud coverage would be very specific to each region and has similar relative impact on energy-yield of both 2J tandems and 1J reference cells. I choose three geographically and meteorologically distinct climates – dry (Albuquerque, NM), temperate (Rapid City, SD), and humid (Miami, FL). For each location, a south facing plane with irradiance-optimized tilt is chosen. The tilt angles from horizontal surface for Albuquerque, Rapid City, and Miami are 29.7°, 37.0°, and 24.5°, respectively. Typical Meteorological Year 3 (TMY3) files from the National Solar Radiation Data Base (NSRDB) are available at each location.[183] These are used as inputs (atmospheric pressure, ambient temperature, relative humidity, daily average temperature, and precipitable water) into the SMARTS model. As one simplification, we keep the cell temperature constant at T_{cell} = 25 ^{o}C in this analysis of the 2T tandems; in reality

differential temperature coefficients will induce additional J-mismatch in the 2T architecture. For Architecture C, I compare the effect of non-constant temperature as discussed below. As a second simplification, I do not consider any losses between cell and module, and between module and power plant substation or transformer. The simulation flowchart for Model 3 is shown in **Figure 4.3**.

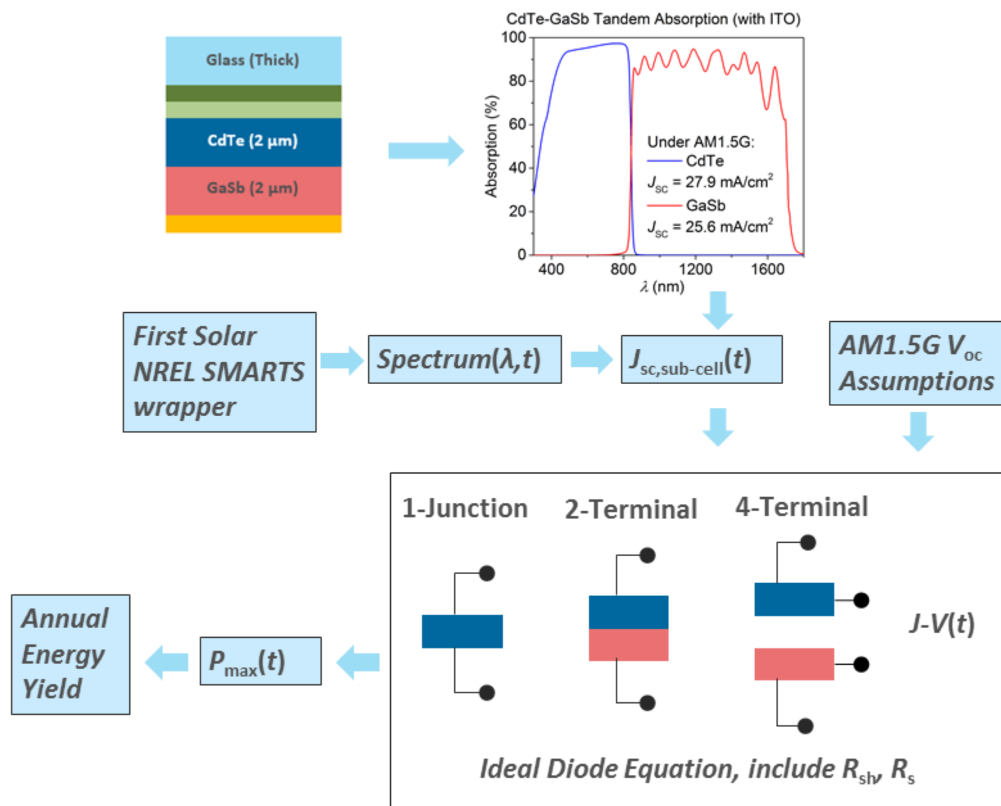

Figure 4.3. Simulation flowchart for tandem energy yield calculation in Model 3

Using these assumptions, I calculate the sub-cells' J-V curves for the 2T and 4T tandems and obtain the hourly power generation, which is integrated throughout the year to obtain the annual energy-yield (kWh/m^2/year). As benchmark I use a non-band gap-graded 1J CdTe cell model, with the same material properties as the top cells in Architectures A and C, with an STC efficiency of 18.6% (**Table 4-3**, **Table 4-4**).

I first calculate the annual energy-yield of Architecture A and compare to that of the 1J CdTe benchmark cell. For the tandem cell, I use indium tin oxide (ITO) as front transparent-conducting oxide (TCO) instead of the typically used fluorine-doped tin oxide (FTO). The higher infrared transmission of ITO both increases the bottom cell J_{sc} and reduces the J_{sc}-mismatch between the sub-cells from 5 mA/cm^2 to 2.2 mA/cm^2 (**Figure 4.4**).

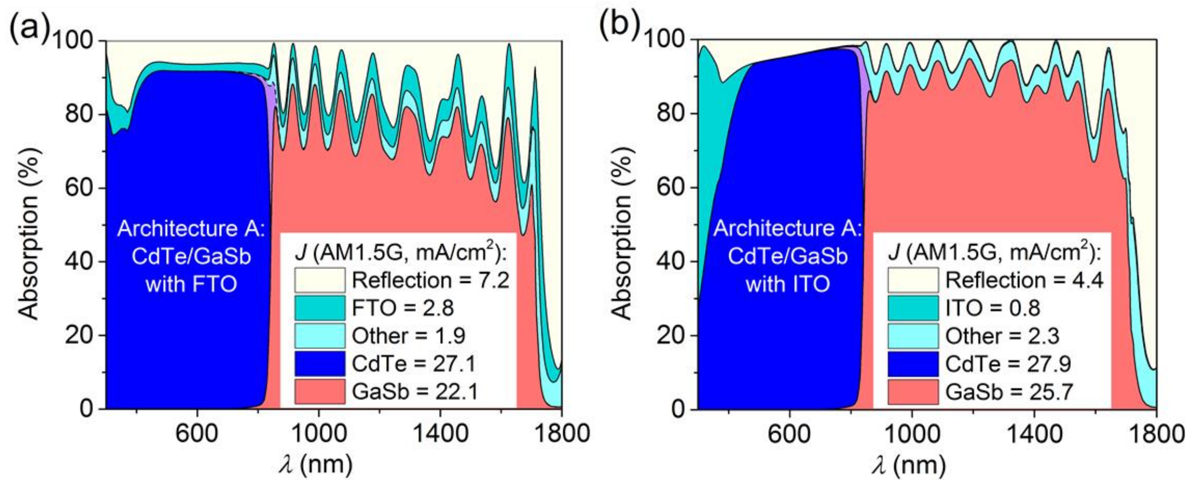

Figure 4.4. Light Absorption for Architecture A with FTO vs ITO as TCO

Figure 4.5 shows the device structure for the tandem's architecture; the modeled STC efficiency of this 2T tandem is 23.1%, which is a 24% relative increase from the STC efficiency of the 1J CdTe reference cell (**Table 4-3**). The annual energy-yield of Architecture A in a dry climate is 22% relative higher than the benchmark 1J CdTe cell (**Figure 4.5**). However, the energy-yield advantage is severely reduced in the humid climate, where Architecture A only yields an 11% energy-yield advantage relative to the 1J CdTe cell. This effect will be discussed in detail below (**Section 4.2.4**). The open symbols pertain to a hypothetical 4T tandem device that is also discussed in the same context below. I also note that the annual solar insolation at Rapid City, SD (44.1^o N) is lower than the annual solar insolation at Albuquerque, NM (35.1^o N) and Miami, FL (25.7^o N), which explains the lower overall energy-yield for the temperate climate example.

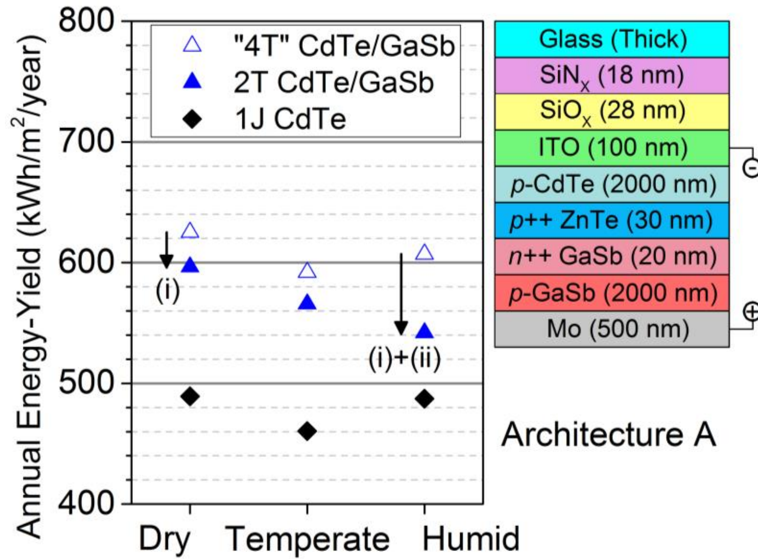

Figure 4.5. Device structure and energy yield of Architecture A in Model 3

Semi-empirical annual energy-yield model for a 2T CdTe/GaSb tandem cell (Architecture A in the text) for dry (Albuquerque), temperate (Rapid City) and humid (Miami) climate. The symbols for "4T" represent the energy-yield of an imaginary tandem with identical device layer stack but with independent maximum power point tracking of the two sub-cells. Loss mechanism (i) originates from a slight *J*-mismatch due to imperfect optics. Loss mechanism (ii) originates from additional *J*-mismatch due to atmospheric water vapor that mutes the bottom cell contribution. T_{cell} = 25 ^{o}C is assumed.

Next I calculate the annual energy-yield of Architecture B. **Figure 4.6** shows the device model for this tandem's architecture. Because the spectral response of the bottom sub-cells of Architectures B and C only extends to λ = 1240 nm, I choose standard FTO as the front TCO for both architectures. Model 3 provides the STC efficiency for Architecture B at 25.6%, which is a 38% increase relative to the 1J CdTe model. The annual energy-yield for Architecture B, shown in **Figure 4.6**, is 33% relative higher in the dry climate, and 25% relative higher in the humid climate compared to the 1J CdTe cell (**Figure 4.6**). The discussion of the open symbols is found in **Section 4.3** below.

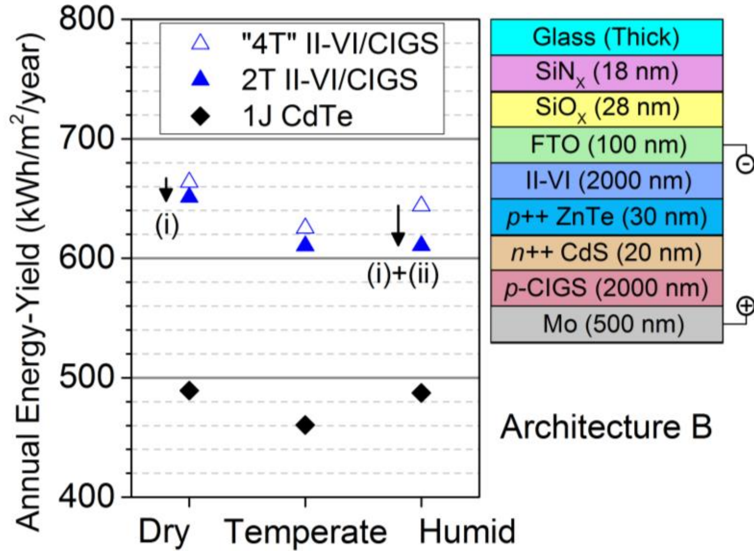

Figure 4.6. Device structure and energy yield of Architecture B in Model 3

Semi-empirical annual energy-yield model for a 2T high-E_g II-VI/CIGS tandem (Architecture B in the text). For the explanation of the "4T" symbols see caption to **Figure 4.5**. No reliance on λ > 1250 nm light and the usage of tunable E_G II-VI top cell enables significant reduction in J-mismatch due to imperfect optics (i) for the dry climate, even when FTO is used. In humid climate, the J-mismatch loss is only slightly higher due to additional infrared spectrum suppression by atmospheric water vapor absorption (ii). T_{cell} = 25 ^oC is assumed.

For the annual energy-yield calculation of the 4T tandem Architecture C, I design the optical stack by including ITO antireflective electrodes and an optically thick EVA encapsulation layer between the two cells, as shown in the **Figure 4.7**. The respective interlayer ITO thicknesses are chosen to maximize the J_{sc} generated in the bottom cell. The technologies for the respective cells in this tandem pair are relatively mature, so we assume the same $V_{oc,1\text{-}sun}$ values as for published best-in-class superstrate-CdTe and substrate-CIGS cells (**Table 4-4**).[173,174] This leads to an STC efficiency of 26.0% for Architecture C, a 40% increase relative to that of the benchmark 1J CdTe cell. The annual energy-yield production is 38% and 33% larger than the 1J CdTe cell in the dry and the humid climate, respectively (**Figure 4.7**).

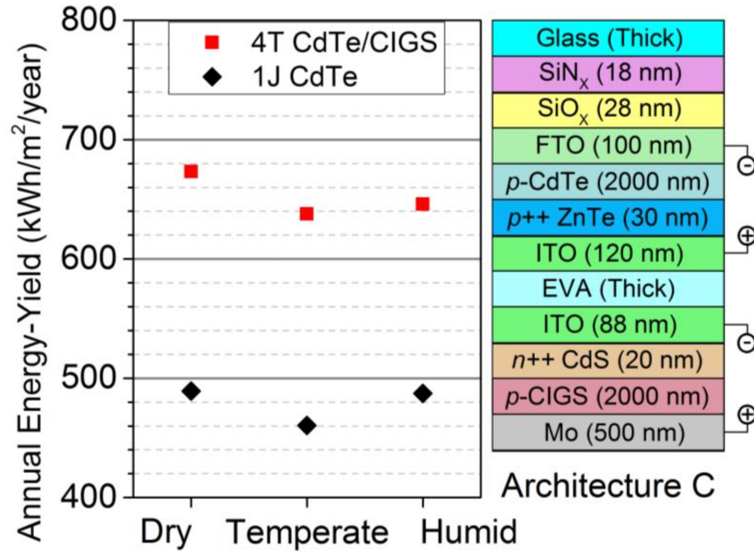

Figure 4.7. Device structure and energy yield of Architecture C in Model 3

Semi-empirical annual energy-yield model for a 4T CdTe/CIGS tandem (architecture *C* in the text). There is no *J*-mismatch loss in this configuration. T_{cell} = 25 °C is assumed.

Table 4-5 summarizes the three tandems' energy-yield advantages with regard to CdTe at T_{cell} = 25 °C.

Architecture	Dry (Albuquerque)	Temperate (Rapid City)	Humid (Miami)
A (2T)	22%	23%	11%
B (2T)	33%	33%	25%
C (4T)	38%	38%	33%

Table 4-5. Tandem relative energy-yield advantage over a 1J CdTe cell

4.2.4. Model 3 Extension: Inclusion of Cell Operating Temperature

To demonstrate the impact of a realistic operating cell temperature, T_{cell}, I calculate here the energy-yield of Architecture C using Model 3. T_{cell} is calculated using the formula[184]:

Equation 4.11 $$T_{cell} = T_{amb} + G_{eff}\alpha(1-\varepsilon)/U_c$$

where T_{amb} is the ambient temperature recorded in the NREL SMARTS model's TMY3 file, G_{eff} is the hourly irradiance, α is the cell absorption coefficient assumed to be 0.9, ε is the STC

efficiency, and U_c is a user-defined parameter assumed to be 30.7.[184] The power at elevated temperature $P(T_{cell})$ is calculated using the published temperature coefficients T_c of -0.25%/K for CdTe[185] and -0.31%/K for CIGS[186] modules using the formula:

Equation 4.12 $$P(T_{cell}) = P_{STC}\left(1 + T_c(T_{cell} - T_{STC})\right)$$

Figure 4.8 shows the results of this model. The relative impact of T_{amb} on the energy-yield is slightly smaller for the tandem compared to the 1J CdTe cell. In a cold location like Rapid City, energy-yield loss due to temperature (mechanism (iii) in **Figure 4.8**) decreases from 1.5% relative for 1J to 1.0% relative for 4T. The drop is smaller for a hot location like Miami, which only decreases from 4.6% relative for 1J to 4.5% relative for 4T.

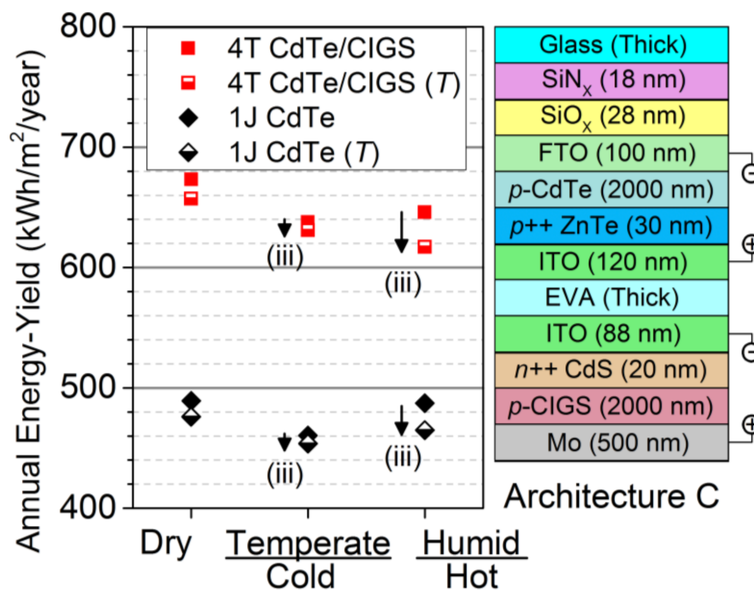

Figure 4.8. Model 3 extended: Temperature effect on energy yield of Architecture C

In this model we also study the effect of cell operating temperature under illumination (data points denoted with *T*). The effect of power loss due to temperature (iii) can be calculated for 4T and 1J architectures (T_{cell} = 25 °C for filled points, simulated operating temperature for half-emptied points).

By intuition, the 4T CdTe/CIGS tandem should be more sensitive to the increase in T_{amb} compared to the 1J CdTe cell because the average T_c of a 4T tandem is larger than that of a 1J

CdTe cell (T_c of CIGS cell is larger than CdTe because CIGS' E_g is smaller). However, the power contribution from the bottom cell in a tandem is much smaller than the power contribution of the top cell so power loss from the bottom cell due to T_{amb} increase is much less significant. After taking into account the increase in 4T tandem cell efficiency compared to the 1J cell (correspondingly, reduced T_{cell} for 4T tandem compared to 1J CdTe), the 4T CdTe/CIGS tandem is actually less affected by the increase in T_{amb} compared to the 1J CdTe cell. I note that an extensive device physics simulation is necessary to investigate the impact of non-standard T_{cell} on the 2T tandems, which is not conducted here; this is because my model does not incorporate the change of sub-cells' *J-V* curve shape with respect to T_{cell}. Incorporating this change will be necessary to calculate the *J-V* curve of 2T tandem under varying T_{cell}, and it represents a limitation to my current modeling methodology.

4.3. Discussion

Architecture A has the lowest energy-yield advantage relative to a 1J CdTe cell (488 kWh/m^2/year baseline). This is especially the case in the humid climate, where the energy-yield advantage relative to 1J CdTe is only 55 kWh/m^2/year (relative 11% advantage), compared to 107 kWh/m^2/year (relative 22% advantage) in the dry climate. This poorer energy-yield in humid climate is caused by J mismatch in the tandem, which is explained in **Figure 4.9**: the spectral density of AM1.5G spectrum's "equivalent current density" (J_{eq} density, defined in the caption of **Figure 4.9**) shows deep absorption bands associated with atmospheric water vapor.[187,188] The absorption bands at λ = 940, 1120, & 1400 nm are significant because they affect the GaSb bottom cell whose spectral response extends from 850-1750 nm in tandem Architecture A. The humid climate spectrum of Miami has thus less infrared photons in this IR

spectrum range compared to the dry climate spectrum of Albuquerque, resulting in relative drop of J_{sc} within the bottom cell. Due to the J-matching constraint, discussed in the context of the SQL efficiency in Model 1, this J drop is propagated throughout the tandem and significantly reduces the 2T energy-yield.

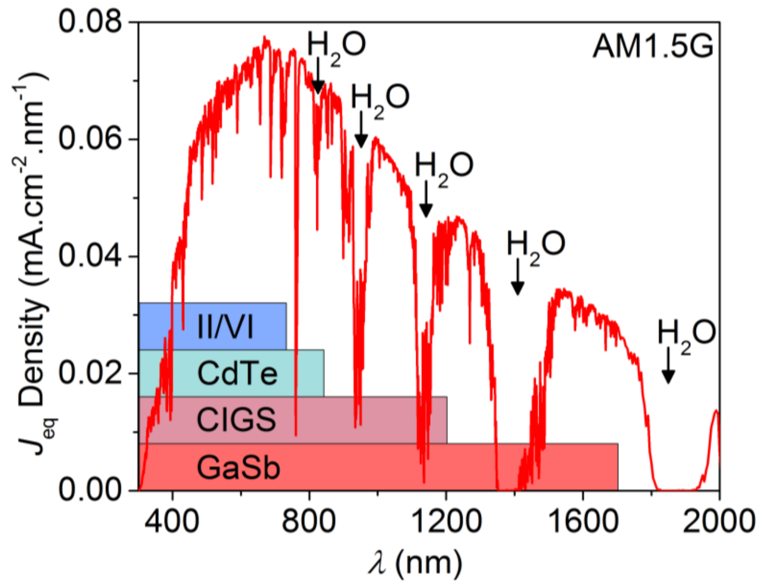

Figure 4.9. Dips in AM1.5G spectrum due to water vapor absorption

Spectral density of J_{eq} for AM1.5G spectrum, defined as the spectral density of J_{sc} which can be generated by a solar cell with perfect EQE(λ) throughout the entire AM1.5G spectrum range. H_2O vapor absorption band in the atmosphere are indicated, as well as the spectral response range for high-E_g II-VI, CdTe, CIGS, and GaSb used in this model.

As a didactic tool, I quantify the J-mismatch loss by modeling the hypothetical tandem cell's output for sub-cells that are operated independently, without any constraint of J-matching ("4T" empty blue triangles in **Figure 4.5**). For this tandem, for which power calculation is performed in the same way as with a 4T device, the relative energy-yield advantage versus the 1J CdTe benchmark improves to 25% in the humid climate, and 28% in the dry climate, which is significantly higher than in the 2T case. I also note that the observed 5% relative energy-yield loss between the "4T" and 2T tandems in the dry climate is caused by a small J-mismatch caused by imperfect optics of the thin-film tandem stack (mechanism (i) in **Figure**

4.5). On the other hand, the relatively larger energy-yield loss of 11% between the "4T" and 2T tandems in the humid climate is a result of both optical (mechanism (i)) and atmospheric water vapor absorption (mechanism (ii)).

Compared to Architecture A, Architecture B is significantly less dependent on the availability of infrared light because the spectral response of this tandem only extends to λ = 1240 nm (see indicated absorption region for CIGS bottom cell in **Figure 4.9**). The annual energy-yield advantage of Architecture B relative to the 1J CdTe cell is 162 kWh/m^2/year (33%) and 123 kWh/m^2/year (25%) in the dry and humid climates, respectively. Architecture C, which does not have any *J*-matching constraint, has an energy-yield advantage of 184 kWh/m^2/year (38%) and 159 kWh/m^2/year (33%) over the 1J CdTe for the dry and the humid climates, respectively. These are the highest among the three architectures being considered as the loss mechanisms (i) is absent in 4T tandems with independent sub-cell MPP tracking, while loss mechanism (ii) is greatly suppressed in a 4T CdTe/CIGS tandem because CIGS has larger E_g than GaSb.

4.4. Conclusions & Perspectives

In this chapter we have addressed for the first time the question of energy-yield prediction for 2J tandem cells in real-world spectral climate conditions, consisting of two sub-cells, with at least one sub-cell built from of a mature, commercial thin-film technology. We achieve this goal by using a three-step modeling approach for (1) sub-cell material selection, (2) sensitivity assessment of the tandem efficiency on sub-cell device quality, and (3) an accurate, physics-based, and high-speed calculation of the annual tandem energy-yield using hourly climate spectra in different locations.

The most important learnings from this research are:

1. First focusing on the lowest-cost tandem -- a monolithic thin-film/thin-film 2T architecture -- we find that a state-of-the-art CdTe top cell, coupled to a current-matched low-E_g bottom-cell material like GaSb, provides only a moderate energy-yield advantage, especially in humid climates. This is explained quantitatively through infrared light absorption from water vapor in the atmosphere, which mutes the bottom-cell current.
2. The sensitivity to atmospheric water vapor is less pronounced in a 2T, higher-E_g tandem, using commercial CIGS as a bottom cell, and a high-E_g II-VI alloy like CdZnTe as a top cell. Here, the energy-yield advantage versus the 1J CdTe benchmark cell reaches between 25% for a humid and 33% for a dry climate. We point out that for this tandem design significant R&D is required for (a) passivation recipes for high-E_g II-VI alloys, (b) transparent back-contacts for the top cell, (c) tunnel junction between the top and bottom cell, and (d) an efficient CIGS cell in superstrate configuration.
3. The highest energy-yield advantage, in all climate spectra being considered (and up to 38% in dry climates), is predicted for a 4T tandem with mature CdTe as top and mature CIGS as bottom cell. Of the three tandems studied, this architecture will require the least R&D. However, it also has the highest expected manufacturing cost and the highest capital expense for manufacturing facilities, because some steps in the module fabrication would have to be doubled if compared to a 2T monolithic tandem.

Ongoing work is addressing true bottom-up cost modeling of the 2T and 4T tandems studied in this work. The combination of manufacturing cost and energy-yield will allow for a

side-by-side comparison of a future tandem's cost of energy with that of state-of-the-art, low cost 1J thin film solar cells like CdTe.

Chapter 5: Conclusion

Three distinct methods to improve the performance of commercial solar cells like silicon and CdTe have been explored. In **Chapter 2**, we evaluated the sub-band gap optoelectronic response of silicon for potential use in silicon-based intermediate-band solar cells. We designed and fabricated sub-band gap silicon photodiodes made of silicon hyperdoped with gold (Si:Au). We found that while Si:Au photodiodes produce sub-band gap photoresponse, the magnitude was too small and it was unlikely that Si:Au can be used to make efficient silicon-based intermediate-band solar cells in the future.

In **Chapter 3**, we demonstrated both 4T and 2T perovskite/silicon tandem solar cells. The perovskite/silicon tandem solar cells is an approach which can potentially be used to make efficient and low-cost multijunction solar cells based on silicon. In our early devices, we were able to show 4T tandem with 17.0% efficiency and 2T tandem with 13.7% efficiency. Since then, the research community has been able to increase the perovskite/silicon tandem efficiency to beyond 20%, and we expect the cell efficiency to continue increasing. Current research efforts in the group include easing the integration of perovskite/silicon tandem solar cells with current silicon solar cell manufacturing capabilities in the industry. We expect perovskite reliability concerns to continue being the most persistent issue which has to be addressed before perovskite/silicon tandem solar cells can be commercialized.

Finally, in **Chapter 4** we collaborated with First Solar to evaluate the commercial feasibility of tandem solar cells based on CdTe and higher-E_g II-VI materials. Semi-empirical energy yield model was built to rapidly evaluate the annual energy yield of different CdTe-

based tandem architectures. We found that 2T tandem solar cells with CdTe top cells and GaSb bottom cells (Architecture A) perform poorly in the humid climate because the *J*-deficit in the bottom cell (due to IR absorption by H_2O vapor in the atmosphere) causes significant *J*-matching problem, which decreases the tandem performance. On the other hand, we found that either 2T tandem made with higher-E_g II-VI top cells and CIGS bottom cells (Architecture B) or 4T tandem solar cells made with CdTe top cells and CIGS bottom cells (Architecture C) provide significant annual energy yield boost compared to 1J CdTe cells. Further financial evaluation is needed before we can conclude whether CdTe-based tandem solar cells can be commercially viable or not.

Chapter 6: Future Work

Further research is needed on both perovskite/silicon tandem solar cells and CdTe-based tandem solar cells. On the topic of perovskite/silicon tandem solar cells, it is very important to improve the stability of the perovskite solar cells; either by advanced encapsulation method or by modifying the perovskite composition. Current efforts by various research groups are encouraging. Substituting organic components with inorganic components seems to improve the photo-stability of the perovskite.[107] Applying oxide film (ITO) to encapsulate the perovskite improves the thermal and environmental stability of the perovskite, and simultaneously form semi-transparent perovskite contact for tandem applications.[140]

In addition to the issue of perovskite stability, it is also important to demonstrate efficient 2T perovskite/silicon tandem solar cells with inverted perovskite solar cells because this will enable easy integration with current silicon solar cell manufacturing capacity, which is dominated by ***p***-type solar cells. Better interlayer stack for this tandem may be necessary; for example, the usage of NiO_x as tandem interlayer (in lieu of PEDOT:PSS) may enable more efficient inverted perovskite/silicon tandem solar cells. It is also necessary to find ways to manufacture perovskite solar cells on textured substrate instead of on planar substrates. This will enable the development of perovskite solar cells on textured silicon solar cells. The usage of pyramidal texturing will significantly reduce light reflection off the perovskite/silicon tandem solar cell surface, and increase the tandem cell's current density and efficiency closer to its fundamental limit.

The perovskite cells in this thesis were fabricated using solution process, but it may be the case that perovskite vapor deposition process is necessary in large scale manufacturing. This is especially so if the prevailing tandem architecture for commercialization is a 2T perovskite/silicon tandem, which may require vapor deposition process to enable perovskite deposition on textured bottom silicon sub-cells. If the prevailing tandem architecture is the 4T perovskite/silicon tandem, solution deposition process may be preferred because it is potentially less expensive than a vapor deposition process.

On the topic of CdTe-based tandems, it will be necessary to first build cost model which compares the levelized cost of electricity (LCOE, in ¢/kWh unit) of CdTe-based tandem solar cells to that of 1J CdTe solar cells. If the economics of CdTe-based tandem solar cells is favorable, it will then be necessary to invest in R&D to enable CdTe-based tandem solar cells. Ongoing work is addressing true bottom-up cost modeling of the 2T and 4T tandems studied in this work.

References

1. Shockley, W. & Queisser, H. J. Detailed Balance Limit of Efficiency of p-n Junction Solar Cells. *J. Appl. Phys.* **32,** 510 (1961).

2. Swanson, R. M. Approaching the 29% limit efficiency of silicon solar cells. *Proc. 31st IEEE Photovolt. Spec. Conf.* 889–894 (2005).

3. Masuko, K. *et al.* Achievement of more than 25% conversion efficiency with crystalline silicon heterojunction solar cell. *IEEE J. Photovoltaics* **4,** 1433–1435 (2014).

4. NREL. NREL Best Research-Cell Efficiency Chart. (2016). at <http://www.nrel.gov/ncpv/images/efficiency_chart.jpg>

5. Queisser, H. J. Multiple carrier generation in solar cells. *Sol. Energy Mater. Sol. Cells* **94,** 1927–1930 (2010).

6. Luque, A., Martí, A. & Stanley, C. Understanding intermediate-band solar cells. *Nat. Photonics* **6,** 146–152 (2012).

7. Luque, A. & Martí, A. The intermediate band solar cell: Progress toward the realization of an attractive concept. *Adv. Mater.* **22,** 160–174 (2010).

8. Wolf, M., Brendel, R., Werner, J. H. & Queisser, H. J. Solar cell efficiency and carrier multiplication in $Si_{1-x}Ge_x$ alloys. *J. Appl. Phys.* **83,** 4213 (1998).

9. Jadhav, P. J. *et al.* Triplet exciton dissociation in singlet exciton fission photovoltaics. *Adv. Mater.* **24,** 6169–6174 (2012).

10. Congreve, D., Lee, J., Thompson, N. & Hontz, E. External quantum efficiency above 100% in a singlet-exciton-fission–based organic photovoltaic cell. *Science* **340,** 334–337 (2013).

11. Thompson, N. J. *et al.* Energy harvesting of non-emissive triplet excitons in tetracene by emissive PbS nanocrystals. *Nat. Mater.* **13,** 1039–1043 (2014).

12. Okada, Y. *et al.* Intermediate band solar cells: Recent progress and future directions. *Appl. Phys. Rev.* **2,** 021302 (2015).

13. Luque, A. *et al.* General equivalent circuit for intermediate band devices: Potentials, currents and electroluminescence. *J. Appl. Phys.* **96,** 903–909 (2004).

14. Tanaka, T. *et al.* Photogenerated current by two-step photon excitation in ZnTeO intermediate band solar cells with *n*-ZnO window layer. *IEEE J. Photovoltaics* **4,** 196–201 (2014).

15. Tabbal, M. *et al.* Formation of single crystal sulfur supersaturated silicon based junctions by pulsed laser melting. *J. Vac. Sci. Technol. B Microelectron. Nanom. Struct.* **25,** 1847

(2007).

16. Simmons, C. B. *et al.* Enhancing the infrared photoresponse of silicon by controlling the fermi level location within an impurity band. *Adv. Funct. Mater.* **24,** 2852–2858 (2014).

17. Dimroth, F. *et al.* Four-junction wafer-bonded concentrator. *IEEE J. Photovoltaics* **6,** 343–349 (2016).

18. Mailoa, J. P. *et al.* Room-temperature sub-band gap optoelectronic response of hyperdoped silicon. *Nat. Commun.* **5,** 3011 (2014).

19. Bailie, C. D. *et al.* Semi-transparent perovskite solar cells for tandems with silicon and CIGS. *Energy Environ. Sci.* **8,** 956–963 (2015).

20. Mailoa, J. P. *et al.* A 2-terminal perovskite/silicon multijunction solar cell enabled by a silicon tunnel junction. *Appl. Phys. Lett.* **106,** 121105 (2015).

21. Mailoa, J. P. *et al.* Optical loss analysis of monolithic perovskite/Si tandem solar cell. in *Proc. 42nd IEEE PVSC* 1–3 (2015).

22. Nature Communications. Nature Communications Open Access Policy. (2016). at <http://www.nature.com/ncomms/open_access/index.html>

23. Creative Commons. Creative Commons Attribution 4.0 International (CC BY 4.0). (2016). at <http://creativecommons.org/licenses/by/4.0/>

24. Zhang, B. Y. *et al.* Broadband high photoresponse from pure monolayer graphene photodetector. *Nat. Commun.* **4,** 1811 (2013).

25. Lee, S. J. *et al.* A monolithically integrated plasmonic infrared quantum dot camera. *Nat. Commun.* **2,** 286 (2011).

26. Liu, X. *et al.* Bridging the mid-infrared-to-telecom gap with silicon nanophotonic spectral translation. *Nat. Photonics* **6,** 667–671 (2012).

27. Luque, A. & Martí, A. Photovoltaics: Towards the intermediate band. *Nat. Photonics* **5,** 137–138 (2011).

28. Kang, Y. *et al.* Monolithic germanium/silicon avalanche photodiodes with 340 GHz gain–bandwidth product. *Nat. Photonics* **3,** 59–63 (2009).

29. Michel, J., Liu, J. & Kimerling, L. C. High-performance Ge-on-Si photodetectors. *Nat. Photonics* **4,** 527–534 (2010).

30. Wang, G. *et al.* High quality Ge epitaxial layers in narrow channels on Si (001) substrates. *Appl. Phys. Lett.* **96,** 111903 (2010).

31. Yan, J. *et al.* Dual-gated bilayer graphene hot-electron bolometer. *Nat. Nanotechnol.* **7,** 472–478 (2012).

32. Tanaka, A. *et al.* Infrared focal plane array incorporating silicon IC process compatible bolometer. *IEEE Trans. Electron Devices* **43,** 1844–1850 (1996).

33. Casalino, M., Coppola, G., Iodice, M., Rendina, I. & Sirleto, L. Near-infrared sub-bandgap all-silicon photodetectors: State of the art and perspectives. *Sensors* **10,** 10571–10600 (2010).

34. Bradley, J. D. B., Jessop, P. E. & Knights, A. P. Silicon waveguide-integrated optical power monitor with enhanced sensitivity at 1550 nm. *Appl. Phys. Lett.* **86,** 1–3 (2005).

35. Doylend, J. K., Jessop, P. E. & Knights, a P. Silicon photonic resonator-enhanced defect-mediated photodiode for sub-bandgap detection. *Opt. Express* **18,** 14671–8 (2010).

36. Grote, R. R. *et al.* 10 Gb/s error-free operation of all-silicon ion-implanted-waveguide photodiodes at 1.55 µm. *IEEE Photonics Technol. Lett.* **25,** 67–70 (2013).

37. Geis, M. W. *et al.* CMOS-compatible all-Si high-speed waveguide photodiodes with high responsivity in near-infrared communication band. *IEEE Photonics Technol. Lett.* **19,** 152–154 (2007).

38. Geis, M. W. *et al.* All silicon infrared photodiodes : photo response and effects of processing temperature. *Opt. Express* **15,** 9–13 (2007).

39. Geis, M. W. *et al.* Silicon waveguide infrared photodiodes with >35 GHz bandwidth and phototransistors with 50 AW^{-1} response. *Opt. Express* **17,** 5193 (2009).

40. Park, D. S.-W., Kim, K., Pillans, B. & Lee, J.-B. Polydimethylsiloxane-based pattern transfer process for the post-IC integration of MEMS onto CMOS chips. *J. Micromechanics Microengineering* **14,** 335–340 (2003).

41. Lopez, J. L. *et al.* Integration of RF-MEMS resonators on submicrometric commercial CMOS technologies. *J. Micromechanics Microengineering* **19,** 015002 (2008).

42. Green, M. A. & Keevers, M. J. Optical properties of intrinsic silicon at 300 K. *Prog. Photovoltaics Res. Appl.* **3,** 189–192 (1995).

43. Carey, J. E., Crouch, C. H., Shen, M. & Mazur, E. Visible and near-infrared responsivity of femtosecond-laser microstructured silicon photodiodes. *Opt. Lett.* **30,** 1773–1775 (2005).

44. Hu, S. *et al.* Improved photoresponse characteristics in Se-doped Si photodiodes fabricated using picosecond pulsed laser mixing. *Semicond. Sci. Technol.* **27,** 102002 (2012).

45. Smith, M. J. *et al.* The origins of pressure-induced phase transformations during the surface texturing of silicon using femtosecond laser irradiation. *J. Appl. Phys.* **112,** 083518 (2012).

46. Winkler, M. *et al.* Insulator-to-metal transition in sulfur-doped silicon. *Phys. Rev. Lett.*

106, (2011).

47. Ertekin, E. *et al.* Insulator-to-metal transition in selenium-hyperdoped silicon: Observation and origin. *Phys. Rev. Lett.* **108,** 1–5 (2012).

48. Sullivan, J. T. *et al.* Methodology for vetting heavily doped semiconductors for intermediate band photovoltaics: A case study in sulfur-hyperdoped silicon. *J. Appl. Phys.* **114,** 103701 (2013).

49. Olea, J., Pastor, D., Prado, A., Garc, E. & Garc, R. Ruling out the impact of defects on the below band gap photoconductivity of Ti supersaturated Si. *J. Appl. Phys.* **114,** 053110 (2013).

50. Redington, R. W. & van Heerden, P. J. Doped silicon and germanium photoconductors as targets for infrared television camera tubes. *J. Opt. Soc. Am.* **49,** 997–1001 (1959).

51. Sclar, N. Survey of dopants in silicon for 2-2.7 and 3-5 μm infrared detector application. *Infrared Phys.* **17,** 71–82 (1977).

52. Recht, D. *et al.* Supersaturating silicon with transition metals by ion implantation and pulsed laser melting. *J. Appl. Phys.* **114,** 124903 (2013).

53. Priolo, F. *et al.* Trapping of Au in Si during pulsed laser irradiation: A comparison with ion beam induced segregation. *Appl. Phys. Lett.* **53,** 2486–2488 (1988).

54. Auston, D. H., Surko, C. M., Venkatesan, T. N. C., Slusher, R. E. & Golovchenko, J. A. Time-resolved reflectivity of ion-implanted silicon during laser annealing. *Appl. Phys. Lett.* **33,** 437–440 (1978).

55. Graff, K. *Metal impurities in silicon-device fabrication*. (Springer Publishing Company, 1999).

56. Trumbore, F. A. Solid solubilities of impurity elements in germanium and silicon. *Bell Syst. Tech. J.* **39,** 205–233 (1960).

57. Cagnina, S. F. Enhanced gold solubility effect in heavily *n*-type silicon. *J. Electrochem. Soc. Solid State Sci.* **116,** 498–502 (1969).

58. Brown, M., Jones, C. L. & Willoughby, A. F. W. Solubility of gold in *p*-type silicon. *Solid. State. Electron.* **18,** 763–770 (1975).

59. Cullis, A. G. *et al.* Growth interface breakdown during laser recrystallization from the melt. *Appl. Phys. Lett.* **38,** 642–644 (1981).

60. Sullivan, J. T. *et al.* Soft x-ray emission spectroscopy studies of the electronic structure of silicon supersaturated with sulfur. *Appl. Phys. Lett.* **99,** 142102 (2011).

61. Dash, W. C. & Newman, R. Intrinsic optical absorption in single-crystal germanium and

silicon at 77°K and 300°K. *Phys. Rev.* **99,** 1151–1155 (1955).

62. Valdinoci, M., Colalongo, L., Pellegrini, A., Rudan, M. & Member, S. Analysis of conductivity degradation in gold/platinum-doped silicon. *IEEE Trans. Electron Devices* **43,** 2269–2275 (1996).

63. Bristow, A. D., Rotenberg, N. & Van Driel, H. M. Two-photon absorption and Kerr coefficients of silicon for 850-2200 nm. *Appl. Phys. Lett.* **90,** 191104 (2007).

64. Perera, A. G. U., Yuan, H. X. & Francombe, M. H. Homojunction internal photoemission far-infrared detectors: Photoresponse performance analysis. *J. Appl. Phys.* **77,** 915–924 (1995).

65. García-Hemme, E. *et al.* Sub-bandgap spectral photo-response analysis of Ti supersaturated Si. *Appl. Phys. Lett.* **101,** 192101 (2012).

66. Dunn, M. H. & Ebrahimzadeh, M. Parametric generation of tunable light from continuous-wave to femtosecond pulses. *Science* **286,** 1513–1517 (1999).

67. Sah, C. T. & Tasch, A.F., J. Precise determination of the multiphonon and photon carrier generation. *Phys. Rev. Lett.* **19,** 69–71 (1967).

68. C.T. Sah, Tasch, A. F. J. & Schroder, D. K. Recombination properties of the gold acceptor level in silicon using the impurity photovoltaic effect. *Phys. Rev. Lett.* **19,** 71–72 (1967).

69. Okuyama, M., Matsunaga, N., Chen, J.-W. & Milnes, A. G. Photoionization cross-sections and energy levels of gold, iron, platinum, silver, and titanium in silicon. *J. Electron. Mater.* **8,** 501–515 (1979).

70. Shockley, W. & Read, W. T., J. Statistics of the recombination of holes and electrons. *Phys. Rev.* **87,** 835–842 (1952).

71. Canali, C., Majni, G., Minder, R. & Ottaviani, G. Electron and hole drift velocity measurements in silicon and their empirical relation to electric field and temperature. *IEEE Trans. Electron Devices* **22,** 1045–1047 (1975).

72. Sah, C. T., Forbes, L., Rosier, L. L. & Tasch, A.F., J. Thermal and optical emission and capture rates and cross sections of electrons and holes at imperfection centers in semiconductors from photo and dark junction current and capacitance measurements. *Solid. State. Electron.* **13,** 759–788 (1970).

73. Weman, H. *et al.* Electrical and optical properties of gold-doped *n*-type silicon. *J. Appl. Phys.* **65,** 137–145 (1989).

74. Bullis, W. M. Properties of gold in silicon. *Solid. State. Electron.* **9,** 143–168 (1966).

75. Braun, S. & Grimmeiss, H. G. Optical properties of gold acceptor and donor levels in silicon. *J. Appl. Phys.* **45,** 2658–2665 (1974).

76. Kurik, M. V. Urbach rule. *Phys. Status Solidi* **8,** 9–45 (1971).

77. Grimmeiss, H. G. & Ledebo, L.-A. Spectral distribution of photoionization cross sections by photoconductivity measurements. *J. Appl. Phys.* **46,** 2155–2162 (1975).

78. Grimmeiss, H. G. & Ledebo, L.-A. Photo-ionization of deep impurity levels in semiconductors with non-parabolic bands. *J. Phys. C Solid State Phys.* **8,** 2615–2626 (1975).

79. Lucovsky, G. On the photoionization of deep impurity centers in semiconductors. *Solid State Commun.* **3,** 299–302 (1965).

80. Yablonovitch, E. & Gmitter, T. Auger recombination in silicon at low carrier densities. *Appl. Phys. Lett.* **49,** 587–589 (1986).

81. RSC. RSC License, Copyright & Permissions. (2016). at <http://www.rsc.org/journals-books-databases/journal-authors-reviewers/licences-copyright-permissions/>

82. AIP. AIP Copyright & Permission to Reuse AIP Material FAQ. (2016). at <http://authortoolkit.aip.org/CopyrightPermissionsFAQ.pdf>

83. IEEE. IEEE Permissions FAQ. (2016). at <https://www.ieee.org/publications_standards/publications/rights/permissions_faq.pdf >

84. Basore, P. A. Understanding manufacturing cost influence on future trends in silicon photovoltaics. *IEEE J. Photovoltaics* **4,** 1477–1482 (2014).

85. Powell, D. M., Winkler, M. T., Goodrich, A. & Buonassisi, T. Modeling the cost and minimum sustainable price of crystalline silicon photovoltaic manufacturing in the United States. *IEEE J. Photovoltaics* **3,** 662–668 (2013).

86. Green, M. A., Emery, K., Hishikawa, Y., Warta, W. & Dunlop, E. D. Solar cell efficiency tables (version 45). *Prog. Photovoltaics Res. Appl.* **23,** 1–9 (2015).

87. Umeno, M., Soga, T., Baskar, K. & Jimbo, T. Heteroepitaxial technologies on Si for high-efficiency solar cells. *Sol. Energy Mater. Sol. Cells* **50,** 203–212 (1998).

88. Tanabe, K., Watanabe, K. & Arakawa, Y. III-V/Si hybrid photonic devices by direct fusion bonding. *Sci. Rep.* **2,** 349 (2012).

89. Beiley, Z. M. & McGehee, M. D. Modeling low cost hybrid tandem photovoltaics with the potential for efficiencies exceeding 20%. *Energy Environ. Sci.* **5,** 9173–9179 (2012).

90. Loper, P. *et al.* Organic–inorganic halide perovskites: Perspectives for silicon-based tandem solar cells. *IEEE J. Photovoltaics* **4,** 1545–1551 (2014).

91. Meillaud, F., Shah, a., Droz, C., Vallat-Sauvain, E. & Miazza, C. Efficiency limits for single-

junction and tandem solar cells. *Sol. Energy Mater. Sol. Cells* **90,** 2952–2959 (2006).

92. Carmody, M. *et al.* Single-crystal II-VI on Si single-junction and tandem solar cells. *Appl. Phys. Lett.* **96,** 28–30 (2010).

93. Umeno, M., Shimizu, H., Egawa, T., Soga, T. & Jimbo, T. First results of AlGaAs/Si monolithic 2-terminal tandem solar cell grown by MOCVD. *Proc. 22nd IEEE PVSC* 361–364 (1991).

94. O'Regan, B. & Grätzel, M. A low-cost, high-efficiency solar cell based on dye-sensitized colloidal TiO2 films. *Nature* **353,** 737–740 (1991).

95. Yu, G., Gao, J., Hummelen, J. C., Wudl, F. & Heeger, A. J. Polymer photovoltaic cells: Enhanced efficiencies via a network of internal donor-acceptor heterojunctions. *Science* **270,** 1789–1791 (1995).

96. Cusano, D. A. CdTe solar cells and photovoltaic heterojunctions in II–VI compounds. *Solid. State. Electron.* **6,** 217–218 (1963).

97. Buch, F., Fahrenbruch, A. L. & Bube, R. H. Photovoltaic properties of five II-VI heterojunctions. *J. Appl. Phys.* **48,** 1596–1602 (1977).

98. Tian, B. *et al.* Coaxial silicon nanowires as solar cells and nanoelectronic power sources. *Nature* **449,** 885–889 (2007).

99. You, J. *et al.* A polymer tandem solar cell with 10.6% power conversion efficiency. *Nat. Commun.* **4,** 1446 (2013).

100. Yang, J., Banerjee, A. & Guha, S. Triple-junction amorphous silicon alloy solar cell with 14.6% initial and 13.0% stable conversion efficiencies. *Appl. Phys. Lett.* **70,** 2975–2977 (1997).

101. Liu, M., Johnston, M. B. & Snaith, H. J. Efficient planar heterojunction perovskite solar cells by vapour deposition. *Nature* **501,** 395–398 (2013).

102. Lee, M. M., Teuscher, J., Miyasaka, T., Murakami, T. N. & Snaith, H. J. Efficient hybrid solar cells based on meso-superstructured organometal halide perovskites. *Science* **338,** 643–647 (2012).

103. Im, J.-H., Lee, C.-R., Lee, J.-W., Park, S.-W. & Park, N.-G. 6.5% efficient perovskite quantum-dot-sensitized solar cell. *Nanoscale* **3,** 4088–4093 (2011).

104. Burschka, J. *et al.* Sequential deposition as a route to high-performance perovskite-sensitized solar cells. *Nature* **499,** 316–9 (2013).

105. Jeon, N. J. *et al.* Compositional engineering of perovskite materials for high-performance solar cells. *Nature* **517,** 476–480 (2015).

106. Ishii, A., Jena, A. K. & Miyasaka, T. Fully crystalline perovskite-perylene hybrid photovoltaic cell capable of 1.2 V output with a minimized voltage loss. *APL Mater.* **2,** 091102 (2014).

107. McMeekin, D. P. *et al.* A mixed-cation lead mixed-halide perovskite: The ideal absorber for tandem solar cells. *Science* **351,** 151–155 (2016).

108. Noh, J. H., Im, S. H., Heo, J. H., Mandal, T. N. & Seok, S. Il. Chemical management for colorful, efficient, and stable inorganic − organic hybrid nanostructured solar cells. *Nano Lett.* **13,** 1764–1769 (2013).

109. Hoke, E. T. *et al.* Reversible photo-induced trap formation in mixed-halide hybrid perovskites for photovoltaics. *Chem. Sci.* **6,** 613–617 (2015).

110. Brandt, R. E., Stevanović, V., Ginley, D. S. & Buonassisi, T. Identifying defect-tolerant semiconductors with high minority carrier lifetimes: Beyond hybrid lead halide perovskites. *MRS Commun.* **5,** 265–275 (2015).

111. De Vos, A. Detailed balance limit of the efficiency of tandem solar cells. *J. Phys. D. Appl. Phys.* **13,** 839–846 (2000).

112. PVCDROM. Refining Silicon. (2016). at <http://www.pveducation.org/pvcdrom/manufacturing/refining-silicon>

113. Safarian, J., Tranell, G. & Tangstad, M. Processes for upgrading metallurgical grade silicon to solar grade silicon. *Energy Procedia* **20,** 88–97 (2012).

114. Wikipedia. Silicon. at <https://en.wikipedia.org/wiki/Silicon>

115. Li, J., Chen, G., Zhang, P., Wang, W. & Duan, J. Technical challenges and progress in fluidized bed chemical vapor deposition of polysilicon. *Chinese J. Chem. Eng.* **19,** 747–753 (2011).

116. Esaki, L. New phenomenon in narrow germanium p-n junctions. *Phys. Rev.* **109,** 603–604 (1958).

117. Todorov, T., Gershon, T., Gunawan, O., Sturdevant, C. & Guha, S. Perovskite-kesterite monolithic tandem solar cells with high open-circuit voltage. *Appl. Phys. Lett.* **105,** 173902 (2014).

118. Bauhuis, G. J., Mulder, P. & Schermer, J. J. Ultra-thin , high performance tunnel junctions for III–V multijunction cells. *Prog. Photovoltaics Res. Appl.* **22,** 656–660 (2014).

119. Rubinelli, F. A., Rath, J. K. & Schropp, R. E. I. Microcrystalline *n-i-p* tunnel junction in a-Si:H/a-Si:H tandem cells. *J. Appl. Phys.* **89,** 4010 (2001).

120. Tvingstedt, K. *et al.* Radiative efficiency of lead iodide based perovskite solar cells. *Sci. Rep.* **4,** 6071 (2014).

121. Etgar, L. *et al.* Mesoscopic $CH_3NH_3PbI_3/TiO_2$ heterojunction solar cells. *J. Am. Chem. Soc.* **134,** 17396–17399 (2012).

122. Albrecht, S. *et al.* Monolithic perovskite/silicon-heterojunction tandem solar cells processed at low temperature. *Energy Environ. Sci.* **9,** 81–88 (2015).

123. Todorov, T. *et al.* Monolithic perovskite-CIGS tandem solar cells via in situ band gap engineering. *Adv. Energy Mater.* **5,** 1500799 (2015).

124. You, J. *et al.* Improved air stability of perovskite solar cells via solution-processed metal oxide transport layers. *Nat. Nanotechnol.* **11,** 75–81 (2016).

125. Upadhyaya, A., Sheoran, M., Rohatgi, A. & Ieee. Study of direct PECVD SiN_x-induced surface emitter and bulk defect passivation in *p*-type silicon solar cells. *Proc. 31st IEEE PVSC* 1273–1276 (2005). doi:10.1109/pvsc.2005.1488372

126. Hoke, E. T. *et al.* Reversible photo-induced trap formation in mixed-halide hybrid perovskites for photovoltaics. *Chem. Sci.* **6,** 613–617 (2015).

127. Rowell, M. W. & McGehee, M. D. Transparent electrode requirements for thin film solar cell modules. *Energy Environ. Sci.* **4,** 131 (2011).

128. Beiley, Z. M. *et al.* Semi-transparent polymer solar cells with excellent sub-bandgap transmission for third generation photovoltaics. *Adv. Mater.* **25,** 7020–7026 (2013).

129. Margulis, G. Y. *et al.* Spray deposition of silver nanowire electrodes for semitransparent solid-state dye-sensitized solar cells. *Adv. Energy Mater.* **3,** 1657–1663 (2013).

130. Lee, J., Lee, I., Kim, T. S. & Lee, J. Y. Efficient welding of silver nanowire networks without post-processing. *Small* **9,** 2887–2894 (2013).

131. Nguyen, W. H., Bailie, C. D., Unger, E. L. & McGehee, M. D. Enhancing the hole-conductivity of spiro-OMeTAD without oxygen or lithium salts by using spiro$(TFSI)_2$ in perovskite and dye-sensitized solar cells. *J. Am. Chem. Soc.* **136,** 10996–11001 (2014).

132. Gaynor, W. *et al.* Color in the corners: ITO-free white OLEDs with angular color stability. *Adv. Mater.* **25,** 4006–4013 (2013).

133. Unger, E. L. *et al.* Hysteresis and transient behavior in current-voltage measurements of hybrid-perovskite absorber solar cells. *Energy Environ. Sci.* **7,** 3690–3698 (2014).

134. Wu, X. *et al.* 13.9%-efficient CdTe polycrystalline thin-film solar cells with an infrared transmission of ~50%. *Prog. Photovoltaics Res. Appl.* **14,** 471–483 (2006).

135. Coutts, T. J., Emery, K. A. & Ward, J. S. Modeled performance of polycrystalline thin-film tandem solar cells. *Prog. Photovoltaics Res. Appl.* **10,** 195–203 (2002).

136. International Technology Roadmap for Photovoltaic (ITRPV) 2013 Results. (2014).

137. Bryant, D. *et al.* A transparent conductive adhesive laminate electrode for high-efficiency organic-inorganic lead halide perovskite solar cells. *Adv. Mater.* **26,** 7499–7504 (2014).

138. Jin, N. *et al.* Diffusion barrier cladding in Si/SiGe resonant interband tunneling diodes and their patterned growth on PMOS source/drain regions. *IEEE Trans. Electron Devices* **50,** 1876–1884 (2003).

139. Wang, Y. *et al.* Solid-phase crystallization and dopant activation of amorphous silicon films by pulsed rapid thermal annealing. *Appl. Surf. Sci.* **135,** 205–208 (1998).

140. Bush, K. A. *et al.* Thermal and environmental stability of semi-transparent perovskite solar cells for tandems enabled by a sputtered ITO electrode. *Adv. Mater.* 1–7 (2016). doi:10.1002/adma.201505279

141. Werner, J. *et al.* Efficient monolithic perovskite/silicon tandem solar cell with cell area > 1 cm^2. *J. Phys. Chem. Lett.* **7,** 161–166 (2016).

142. Filipič, M. *et al.* $CH_3NH_3PbI_3$ perovskite / silicon tandem solar cells: characterization based optical simulations. *Opt. Express* **23,** A263–A278 (2015).

143. Coutts, T. J. *et al.* Critical issues in the design of polycrystalline, thin-film tandem solar cells. *Prog. Photovoltaics* **11,** 359–375 (2003).

144. Liu, H. *et al.* The realistic energy yield potential of GaAs-on-Si tandem solar cells: a theoretical case study. *Opt. Express* **23,** A382 (2015).

145. Haas, A. W., Wilcox, J. R., Gray, J. L. & Schwartz, R. J. Design of a GaInP/GaAs tandem solar cell for maximum daily, monthly, and yearly energy output. *J. Photonics Energy* **1,** 018001 (2011).

146. Chan, N. L. A. *et al.* Validation of energy prediction method for a concentrator photovoltaic module in Toyohashi Japan. *Prog. Photovoltaics Res. Appl.* **21,** 1598–1610 (2013).

147. Green, M. A., Emery, K., Hishikawa, Y., Warta, W. & Dunlop, E. D. Solar cell efficiency tables (version 47). *Prog. Photovolt Res. Appl.* **24,** 3–11 (2016).

148. Lazard Ltd. *Lazard's levelized cost of energy analysis - Version 9.0*. *Lazard* (2015). at <http://www.lazard.com/>

149. Nelson, L., Frichtl, M. & Panchula, A. Changes in cadmium telluride photovoltaic system performance due to spectrum. *IEEE J. Photovoltaics* **3,** 488–493 (2013).

150. Lee, M., Ngan, L., Hayes, W. & Panchula, A. F. Comparison of the effects of spectrum on cadmium telluride and monocrystalline silicon photovoltaic module performance. *Proc. 42nd IEEE PVSC* 1–4 (2015).

151. Lee, M. *et al.* Understanding next generation cadmium telluride photovoltaic

performance due to spectrum. *Proc. 42nd IEEE PVSC* 1–6 (2015).

152. Schweiger, M. & Herrmann, W. Comparison of energy yield data of fifteen PV module technologies operating in four different climates. *Proc. 42nd IEEE PVSC* 1–6 (2015).

153. Würfel, P. *Physics of Solar Cells : From Basic Principles to Advanced concepts*. *Wiley-VCH* (2009). doi:10

154. Brown, A. S. & Green, M. A. Detailed balance limit for the series constrained two terminal tandem solar cell. *Phys. E* **14,** 96–100 (2002).

155. Fraas, L. M. *et al.* Over 35% efficient GaAs/GaSb stacked concentrator cell assemblies for terrestrial applications. *Proc. 21st IEEE PVSC* **1,** 190–195 (1990).

156. Fraas, L. M. & Huang, H.-X. Coarse grain polycrystalline gallium antimonide thermophotovoltaic cell. 1–5 (2000).

157. Sulima, O. V. *et al.* GaSb-, InGaAsSb-, InGaSb-, InAsSbP- and Ge-TPV cells for low-temperature TPV applications. in *Proc. AIP Conf.* 435–441 (2003).

158. Fan, J. *et al.* Influence of temperature ramp on the materials properties of GaSb grown on ZnTe using molecular beam epitaxy. *J. Vac. Sci. Technol. B Microelectron. Nanom. Struct.* **30,** 02B122 (2012).

159. Dhere, R. *et al.* Fabrication and characterization of CdMgTe thin films and their application in solar cells. *MRS Proc.* **1012,** 37–42 (2007).

160. Dhere, R. *et al.* Investigation of CdZnTe for thin-film tandem solar cell applications. in *Proc. Mater. Res. Soc. Spring Meet.* **763,** 409–414 (2003).

161. Martinez, O. S. *et al.* Development of wide band gap $Cd_{1-x}Mg_xTe$/CdS top cells for tandem devices. *Proc. 33rd IEEE PVSC* 1–5 (2008).

162. Dhere, R. *et al.* Investigation of $Cd_{1-x}Mg_xTe$ alloys for tandem solar cell applications. in *Proc. 4th WCPEC* 546–549 (2006).

163. Carmody, M. & Gilmore, A. *High efficiency single crystal CdTe solar cells*. *NREL Subcontract Rep.* (2011).

164. Bonnet, D. & Rickus, E. The CdSe thin-film solar cell. *Proc. 14th IEEE PVSC* 629–632 (1980).

165. Wang, M. W. Novel CdSe-based PV structure for high efficiency CdSe/CIGS tandem solar cells. in *Proc. 34th IEEE PVSC* 489–493 (2009).

166. Meyers, P. V. *et al.* Polycrystalline CdTe on $CuInSe_2$ cascaded solar cells. in *Proc. 20th IEEE PVSC* 1448–1451 (1988).

167. Symko-Davies, M. Status of high performance PV: polycrystalline thin-film tandems. in

Proc. 31st IEEE PVSC 410–413 (2005). doi:10.1109/PVSC.2005.1488156

168. Fu, F. *et al.* Low-temperature-processed efficient semi-transparent planar perovskite solar cells for bifacial and tandem applications. *Nat. Commun.* **6,** 8932 (2015).

169. Cheek, G., Yang, F. & Lee, H. Thin film PV: Moving at the speed of solar. in *Proc. 39th IEEE PVSC* 3407–3410 (2013). doi:10.1109/PVSC.2013.6745180

170. Gale, R. P. *et al.* High-Efficiency GaAs/CuInSe2 and AlGaAs/CuInSe2 Thin-Film Tandem Solar Cells. in *Proc. 21st IEEE PVSC* 53–57 (1990).

171. Dimroth, F. *et al.* Comparison of direct growth and wafer bonding for the fabrication of GaInP/GaAs dual-junction solar cells on silicon. *IEEE J. Photovoltaics* **4,** 620–625 (2014).

172. Green, M. A. Radiative efficiency of state-of-the-art photovoltaic cells. *Prog. Photovoltaics Res. Appl.* **20,** 472–476 (2012).

173. Green, M. A., Emery, K., Hishikawa, Y., Warta, W. & Dunlop, E. D. Solar cell efficiency tables (version 43). *Prog. Photovoltaics Res. Appl.* **22,** 1–9 (2014).

174. Nakamura, M. *et al.* Recent R&D progress in Solar Frontier's small-sized $Cu(InGa)(SeS)_2$ solar cells. *Proc. 40th IEEE PVSC* 0107–0110 (2014). doi:10.1109/PVSC.2014.6925346

175. Burkhard, G. F., Hoke, E. T. & McGehee, M. D. Accounting for interference, scattering, and electrode absorption to make accurate internal quantum efficiency measurements in organic and other thin solar cells. *Adv. Mater.* **22,** 3293–3297 (2010).

176. Adachi, S. Optical dispersion relations for GaP, GaAs, GaSb, InP, InAs, InSb, $Al_xGa_{1-x}As$, and $In_{1-x}Ga_xAs_yP_{1-y}$. *J. Appl. Phys.* **66,** 6030–6040 (1989).

177. Paulson, P. D., Birkmire, R. W. & Shafarman, W. N. Optical characterization of $CuIn_{1-x}Ga_xSe_2$ alloy thin films by spectroscopic ellipsometry. *J. Appl. Phys.* **94,** 879–888 (2003).

178. Ninomiya, S. & Adachi, S. Optical properties of wurtzite CdS. *Electronics* **78,** 1183–1190 (1995).

179. Sopra. Sopra SA Database. (2016). at <http://www.sspectra.com/sopra.html>

180. Mclntosh, K. R. *et al.* An optical comparison of silicone and EVA encapsulants for conventional silicon PV modules: A ray-tracing study. *Proc. 34th IEEE PVSC* 544–549 (2009). doi:10.1109/PVSC.2010.5615830

181. Green, M. A., Emery, K., Hishikawa, Y., Warta, W. & Dunlop, E. D. Solar cell efficiency tables (version 40). *Prog. Photovolt Res. Appl.* **20,** 606–614 (2012).

182. NREL. NREL SMARTS Model. (2016). at <www.nrel.gov/rredc/smarts/>

183. NREL. NREL TMY3 Database. (2016). at <http://rredc.nrel.gov/solar/old_data/nsrdb/>

184. Hayes, W., Panchula, A., Nelson, L. & Francisco, S. Thermal modeling accuracy of hourly averaged data for large free field Cadmium Telluride PV arrays. *Proc. 38th IEEE PVSC* 1–4 (2012).

185. First Solar. First Solar Module FS-Series 3 Product Data Sheet. (2016). at <www.firstsolar.com/~/media/documents/data-sheets/products/module data sheet/pd-5-401-03_series3black-4.ashx>

186. Solar Frontier. Solar Frontier Module SF L-Series Product Data Sheet. (2016). at <www.nobility.cz/files/Solar_Frontier_En_Nobility_Solar_Projects.pdf>

187. Guzzi, R. & Spaziale, A. Water vapor absorption in the visible and near infrared : results of field measurements. *Appl. Opt.* **23,** 1853–1861 (1984).

188. Eldridge, R. G. Water vapor absorption of visible and near infrared radiation. *Appl. Opt.* **6,** 709–714 (1967).

Appendix

A.1. Validation of Semi-Empirical Tandem Energy Yield (Model 3)

In order to test the validity of the semi-empirical energy-yield model (Model 3), we compare the performance of the model to a previously published energy-yield model developed by Liu et.al.[144] The same optical stack (layer material (*n*,*k*) data & thicknesses) are used to calculate the optical absorption in both models. EQE(λ) calculation for Model 3 is only valid for thin-film devices, so the actual EQE(λ) for the bottom Si cell of Model 3 (FS) is taken from the PC1D device physics simulator model calculated by the MIT model.[144] Identical Singapore annual sunlight spectrum is used for the two models, but the energy-yield calculation for the semi-empirical FS model and MIT device physics model are performed independently.[144]

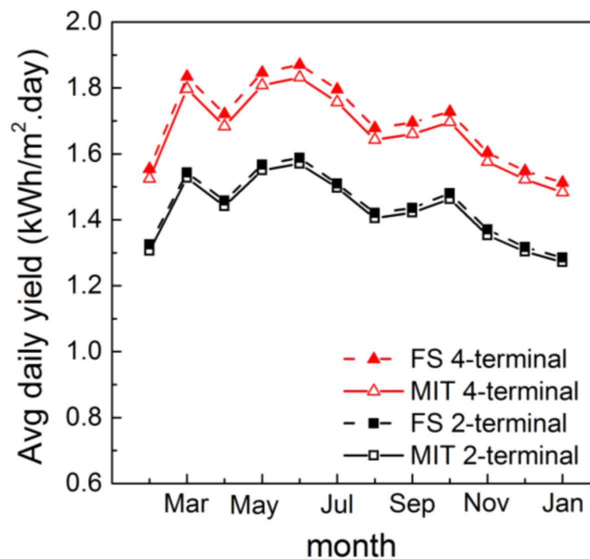

Figure A.1. Validation of Model 3 using device-physics-based baseline model

Comparison of average daily energy yield for 4T (red triangles) and 2T (black squares) GaAs/Si tandem[144] solar cells under annual Singapore spectrum, modeled using PC1D device physics simulator (MIT)[144] and semi-empirical Model 3 of this paper (FS). There is a negligible difference of energy-yield result between the two models, but the semi-empirical model is several orders of magnitudes faster than a full-fledged device physics simulator model.